

อิทธิพลของตัวรองรับและตัวเสริมการรีดักชันบนกัมมันตภาพของตัวเร่ง
ปฏิกิริยาโคบอลต์สำหรับการสังเคราะห์แบบฟิชเชอร์-โทรปซ์



วิทยานิพนธ์นี้เป็นส่วนหนึ่งของการศึกษาตามหลักสูตรปริญญาวิทยาศาสตรดุษฎีบัณฑิต
สาขาวิชาเคมี
มหาวิทยาลัยเทคโนโลยีสุรนารี
ปีการศึกษา 2557

**INFLUENCE OF SUPPORT AND REDUCTION
PROMOTER ON ACTIVITY OF COBALT CATALYSTS
FOR FISCHER-TROPSCH SYNTHESIS**



**A Thesis Submitted in Partial Fulfillment of the Requirements for the
Degree of Doctor of Philosophy in Chemistry
Suranaree University of Technology
Academic Year 2014**

ณัฐวุฒิ โอสระคุ : อิทธิพลของตัวรองรับและตัวเสริมการรีดักชันบนกัมมันตภาพของตัวเร่งปฏิกิริยาโคบอลต์สำหรับการสังเคราะห์แบบฟิชเชอร์-โทรปช์ (INFLUENCE OF SUPPORT AND REDUCTION PROMOTER ON ACTIVITY OF COBALT CATALYSTS FOR FISCHER-TROPSCH SYNTHESIS) อาจารย์ที่ปรึกษา : รองศาสตราจารย์ ดร.จตุพร วิทยาคูณ, 180 หน้า

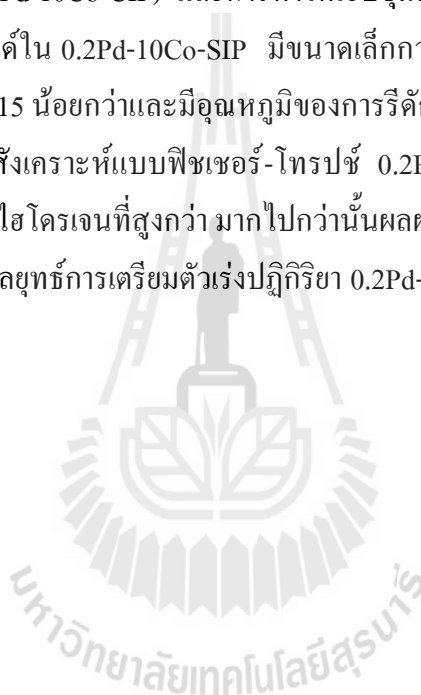
วิทยานิพนธ์นี้ศึกษาเกี่ยวกับการคัดแปรโลหะพาลเลเดียม-โคบอลต์รองรับบนซิลิกาและเฮสปีเอ-15 ใช้เป็นตัวเร่งปฏิกิริยาสำหรับการสังเคราะห์แบบฟิชเชอร์-โทรปช์เพื่อปรับปรุงความสามารถในการเร่งปฏิกิริยาและเพิ่มการเลือกเกิดสารผลิตภัณฑ์ที่อยู่ในช่วงแก๊สโซลีน (C_5-C_9) งานนี้เริ่มต้นด้วยการเปรียบเทียบสมบัติทางกายภาพและเคมีของตัวเร่งปฏิกิริยาโคบอลต์บนตัวรองรับบนซิลิกา (ด้วยปริมาณ 10% โดยน้ำหนัก) ซึ่งเตรียมโดยการทำให้เอิบซุ่ม (10Co-IP) และการตกตะกอนโดยการก่อไมเซลล์แบบผันกลับ (10Co-RM) หลังจากนั้นเติมพาลเลเดียมบนตัวเร่งปฏิกิริยาโคบอลต์ที่เตรียมไว้ทั้งสองแบบเพื่อเป็นตัวเสริม (ด้วยปริมาณพาลเลเดียม 0.2% และ 1% โดยน้ำหนัก) เพื่อที่จะศึกษาอิทธิพลที่เกิดขึ้นต่อตัวเร่งปฏิกิริยา 10Co-IP และ 10Co-RM จากนั้นนำไปทดสอบการเร่งปฏิกิริยาการสังเคราะห์แบบฟิชเชอร์-โทรปช์ที่อุณหภูมิ 230 องศาเซลเซียส และความดัน 5 บาร์ ด้วยอัตราส่วนของไฮโดรเจนต่อคาร์บอนมอนอกไซด์เป็นสองต่อหนึ่ง

ขนาดผลึกของโคบอลต์ออกไซด์ (Co_3O_4) ที่เตรียมจากการทำให้เอิบซุ่มมีขนาดใหญ่กว่าขนาดผลึกจากการเตรียมแบบการตกตะกอนแบบการก่อไมเซลล์แบบผันกลับ ซึ่งส่งผลให้การเลือกเกิดผลิตภัณฑ์ที่ต้องการที่สูงกว่าและเกิดมีเทนและพาราฟิน (C_2-C_4) ต่ำกว่า ยิ่งไปกว่านั้นการเติมพาลเลเดียมในปริมาณ 0.2% โดยน้ำหนักบน 10Co-IP และ 10Co-RM เสริมความสามารถในการเกิดรีดักชันของโคบอลต์ออกไซด์ และการเร่งปฏิกิริยาการสังเคราะห์แบบฟิชเชอร์-โทรปช์และเสริมการเลือกเกิดของพาราฟิน ในทางกลับกันการเติมพาลเลเดียมด้วยปริมาณ 1% โดยน้ำหนักส่งผลให้เพิ่มการเกิดมีเทนแต่ลดการแปลงผันของคาร์บอนมอนอกไซด์ ตัวเร่งปฏิกิริยาที่เหมาะสมคือ 0.2Pd-10Co-IP ซึ่งให้การแปลงผันของคาร์บอนมอนอกไซด์ที่สูงและให้เศษส่วนโมลของสารพาราฟินที่สูงในช่วงแก๊สโซลีน (C_5-C_9)

เพื่อที่จะปรับปรุงความสามารถในการเกิดปฏิกิริยาการสังเคราะห์แบบฟิชเชอร์-โทรปช์และการเลือกเกิดของผลิตภัณฑ์ในช่วงแก๊สโซลีน ส่วนต่อมาก็คือการศึกษาอิทธิพลของรูปร่างตัวรองรับและการเสริมด้วยพาลเลเดียม (ด้วยปริมาณ 0.2% โดยน้ำหนัก) ที่เตรียมด้วยการทำให้เอิบซุ่มร่วมต่อสมบัติทางกายภาพและเคมีของโคบอลต์รองรับบนเฮสปีเอ-15 และเฮสปีเอ-15 (M) โดยเฮสปีเอ-15 (M) ที่ได้จากการสังเคราะห์แบบไฮโดรเทอร์มัลที่มีการเติมเดคเคนมีขนาดอนุภาคที่เล็กกว่าเฮส

บีเอ-15 มีขนาดรูพรุนใหญ่กว่า และมีความยาวของท่อสั้นกว่า ทำให้เพิ่มการกระจายตัวของ โคนบอลต์ออกไซด์ สะดวกต่อการแพร่ของสารตั้งต้นและช่วยให้ปฏิกิริยาการสังเคราะห์แบบฟิชเชอร์-โทรปช์เกิดได้ดีขึ้นบน 10Co/SBA-15(M) ให้ค่าการแปลงผันของคาร์บอนมอนอกไซด์และไฮโดรเจนสูงสุด และให้ผลผลิตของแก๊สโซลีน (C_5-C_9) ที่สูงกว่า การเติมของพาลเลเดียมเพิ่มการรีดักชันของโคนบอลต์ออกไซด์แต่ทำให้เกิดการผลิตมีเทนและพาราฟิน (C_2-C_4) มากกว่า

เพื่อที่จะเพิ่มผลผลิตและการเลือกเกิดสารในช่วงแก๊สโซลีนให้มากขึ้นอีก ได้ศึกษาผลการของเร่งปฏิกิริยาร่วมของพาลเลเดียมและโคนบอลต์บนตัวรองรับบนเอสบีเอ-15 ซึ่งเตรียมโดยการทำให้เอ็บซุ่มร่วม (0.2Pd-10Co-CIP) และการทำให้เอ็บซุ่มตามลำดับ (0.2Pd-10Co-SIP) ขนาดผลึกของโคนบอลต์ออกไซด์ใน 0.2Pd-10Co-SIP มีขนาดเล็กกว่า ทำให้การลดลงของขนาดรูพรุนและพื้นที่ผิวของเอสบีเอ-15 น้อยกว่าและมีอุณหภูมิของการรีดักชันที่สูงกว่า 0.2Pd-10Co-CIP ในการทดสอบปฏิกิริยาการสังเคราะห์แบบฟิชเชอร์-โทรปช์ 0.2Pd-10Co-SIP มีค่าการแปลงผันของคาร์บอนมอนอกไซด์และไฮโดรเจนที่สูงกว่า มากไปกว่านั้นผลผลิตและการเลือกเกิดสารผลิตภัณฑ์ (C_5-C_9)มากที่สุด ได้จากกลุ่ตยู่การเตรียมตัวเร่งปฏิกิริยา 0.2Pd-10Co-SIP



NATTAWUT OSAKOO : INFLUENCE OF SUPPORT AND REDUCTION
PROMOTER ON ACTIVITY OF COBALT CATALYSTS FOR FISCHER-
TROPSCHE SYNTHESIS. THESIS ADVISOR : ASSOC. PROF. JATUPORN
WITTAYAKUN, Ph.D. 180 PP.

SUPPORT/PROMOTER/PALLADIUM/COBALT/FISCHER-TROPSCHE

This thesis involves modification of Pd-Co supported on silica and SBA-15 as catalysts for Fischer-Tropsch synthesis to improve catalytic activity and selectivity in the gasoline range (C_5 – C_9). This work began with a comparison of the physicochemical properties of silica-supported cobalt catalysts (with 10 wt% Co) prepared by impregnation (10Co-IP) and precipitation using a reverse micelle technique (10Co-RM). Then, Pd was added as a promoter (0.2 wt% and 1.0 wt%) to influence the properties of 10Co-IP and 10Co-RM. The reactivity during Fischer-Tropsch synthesis (FTS) was studied at 230 °C, 5 bar with $H_2/CO = 2$.

The crystal size of Co_3O_4 in 10Co-IP was larger than that in 10Co-RM. The 10Co-IP in Co metallic form was mainly hcp phase but the 10Co-RM was mixed hcp and fcc phase. The presence of mainly hcp phase in Co could contribute to lower selectivity to methane and C_2 – C_4 paraffin products and higher selectivity to C_5 – C_9 in 10Co-IP. The addition of 0.2 wt% Pd to 10Co-IP and 10Co-RM enhanced the cobalt reducibility, FTS activity and paraffin selectivity. On the other hand, the addition of 1.0 wt% Pd resulted in increased methane formation but lower CO conversion. The most suitable catalyst was 0.2Pd-10Co-IP, which gave high CO conversions and mole fraction of paraffins in the gasoline range (C_5 – C_9).

To further improve the FT activity and gasoline selectivity, the influence of support morphology and Pd promoter prepared by co-impregnation on the physicochemical properties and catalytic performance of Co/SBA-15 and SBA-15(M) were investigated. The SBA-15(M) from a hydrothermal synthesis with decane addition had smaller particle size, larger pore size and shorter cavity length, which enhanced the dispersion of cobalt oxides, eased diffusion of reactants and improved the FTS performance. 10Co/SBA-15(M) provided the highest and most steady conversions of CO and H₂ with the higher yield of C₅–C₉ products. The addition of Pd enhanced the reduction of cobalt oxides but produced more methane and light paraffins.

To enhance yield and selectivity in gasoline, catalytic performance of bimetallic Pd-Co/SBA-15 prepared by co-impregnation (0.2Pd-10Co-CIP) and sequential impregnation (0.2Pd-10Co-SIP) was studied. The cobalt oxides in 0.2Pd-10Co-SIP had smaller crystal size, leading to less decrease in pore size and surface area of SBA-15 as well as higher reduction temperature, than those in 0.2Pd-10Co-CIP. In FTS testing, 0.2Pd-10Co-SIP had higher CO and H₂ conversions. In addition, the highest yield and selectivity of C₅–C₉ products was obtained by the preparation strategy with 0.2Pd-10Co-SIP.

School of Chemistry

Academic Year 2014

Student's Signature _____

Advisor's Signature _____

ACKNOWLEDGEMENTS

I would like to thank several people who help me to complete my thesis. First of all, my thesis advisor, Assoc. Prof. Dr. Jatuporn Wittayakun, for giving me an interesting research topic and a chance to study at SUT, his kind support, suggestion, encouragement and discussion throughout my research, thesis and paper writing; my supervisor in Germany, Prof. Dr. Frank Roessner for accepting me to his research group at the Industrial Chemistry 2, Carl von Ossietzky Universität Oldenburg; Dr. Robert Henkel from Prof. Dr. Frank Roessner's group for teaching me several research procedures, including catalyst preparation, Fischer-Tropsch reaction testing and product analysis by gas chromatography.

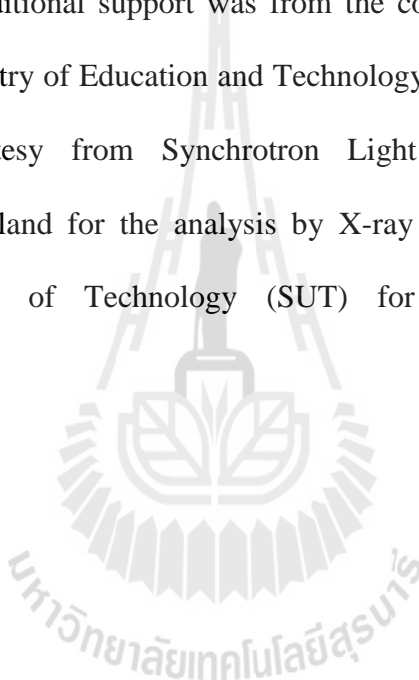
I also thank Dr. Sirinuch Loiha and Dr. Pongtanawat Khemthong for teaching me about synchrotron technique, interpretation and facilitating during TEM measurement at KKU; Asst. Prof. Dr. Sanchai Prayoonpokarach for correction and suggestion during my manuscript preparation. I am also very thankful to the thesis examining committee for their helpful suggestions.

Thanks to all members of catalysis group at SUT for the impressive atmosphere. Special thanks to Onsulang, Saowanee, Wina, Kotchakriangkrai, Saran, Yutadate, Kittinone, Narongrit, Dr. Anupong, Dr. Sittichai, Dr. Nuttinee, Dr. Kamolwan, Dr. Piaw, Dr. Supattra, Dr. Surachai and others for their help, nice conversations and discussion. Also thank to all members of the Industrial Chemistry 2 at the Carl von Ossietzky Universität Oldenburg for help, nice atmosphere, parties and beautiful time.

Particularly, I would like to give my special thanks to my parents, soulmate (Jutamas Osakoo), younger sister and younger brother-in-law for their helps, inspiration, encouragement, additional living allowance, patience and understanding during my education.

Last but not least, my Ph.D. study was supported by the Royal Golden Jubilee Ph.D. Program from Thailand Research Fund (TRF, contract number: PHD/0058/2551). Additional support was from the cooperation research fund from German Federal Ministry of Education and Technology (grant number: APR 09/014). Moreover, the courtesy from Synchrotron Light Research Institute (Public Organization) in Thailand for the analysis by X-ray Absorption spectroscopy and Suranaree University of Technology (SUT) for supporting characterization equipment.

Nattawut Osakoo



CONTENTS

	Page
ABSTRACT IN THAI.....	I
ABSTRACT IN ENGLISH	III
ACKNOWLEDGEMENTS.....	V
CONTENTS.....	VII
LIST OF FIGURES	XII
LIST OF TABLES.....	XV
 CHAPTER	
I INTRODUCTION.....	1
1.1 Aim of thesis	1
1.2 Background of Fischer-Tropsch reaction.....	2
1.3 Background of SBA-15.....	5
1.4 Scope and limitations of the study.....	7
1.5 References	8
II LITERATURE REVIEWS	11
2.1 Fischer-Tropsch synthesis.....	11
2.2 Chemistry of FTS process.....	12
2.3 Fischer-Tropsch product distribution.....	14
2.4 Fischer-Tropsch catalyst	16
2.4.1 Active metal and promoter.....	16

CONTENTS (Continued)

	Page	
2.4.2 Catalyst precursors	18	
2.4.3 The catalyst supports	20	
2.4.4 Synthesis of cobalt catalyst for FTS.....	26	
2.3 References	30	
III PALLADIUM-PROMOTED COBALT CATALYSTS SUPPORTED		
ON SILICA PREPARED BY IMPREGNATION AND		
REVERSE MICELLE FOR FISCHER-TROPSCH SYNTHESIS.....		34
3.1 Introduction	35	
3.2 Experimental	37	
3.2.1 Catalyst preparation	37	
3.2.2 Catalyst characterization	39	
3.2.2 Catalytic testing for FTS	41	
3.3 Results and discussion	43	
3.3.1 Catalyst characterization by XRD.....	43	
3.3.2 Catalyst characterization by TPR.....	45	
3.3.3 Characterization by DR-UV-vis.....	47	
3.3.4 Catalyst characterization by X-ray absorption.....	50	
3.3.4.1 Characterization of calcined 10Co-RM and 10Co-IP		
by XANES and EXAFS	50	
3.3.4.2 Characterization of reduced 10Co-RM and 10Co-IP		
by XANES and EXAFS	56	

CONTENTS (Continued)

	Page
3.3.4.3 Characterization of calcined xPd-10Co-IP and xPd-10Co-RM by XANES.....	58
3.3.4.4 Characterization of reduced xPd-10Co-IP and xPd-10Co-RM by XANES.....	59
3.3.5 FTS activity	63
3.3.5.1 Conversion of CO and H ₂ , selectivity to CH ₄ and chain growth probability	63
3.3.5.2 FTS selectivity	67
3.4 Conclusions.....	71
3.5 References.....	72
IV EFFECT OF SUPPORT MORPHOLOGY AND Pd PROMOTER ON Co/SBA-15 FOR FISCHER-TROPSCH SYNTHESIS.....	
4.1 Introduction.....	79
4.2 Experimental	81
4.2.1 Synthesis of SBA-15 mesoporous silica	81
4.2.1.1 Synthesis of modified SBA-15 (SBA-15(M))	81
4.2.1.2 Synthesis of SBA-15.....	81
4.2.2 Catalyst preparation	82
4.2.2.1 Preparation of mono-metallic catalyst (10Co/SBA-15(M) and 10Co/SBA-15) by incipient wetness impregnation.....	82

CONTENTS (Continued)

	Page
4.2.2.2 Preparation of bimetallic catalyst Pd-Co (0.2Pd-10Co/SBA-15(M) and 0.2Pd-10Co/SBA-15) by co-incipient wetness impregnation.....	82
4.2.3 Catalyst characterization	83
4.2.4 Catalytic testing for FTS	83
4.3 Results and discussion	85
4.3.1 Characterization by N ₂ adsorption-desorption	85
4.3.2 Support characterization by SEM and TEM	88
4.3.3 Catalyst characterizations by XRD and TEM.....	90
4.3.4 Characterization by XANES	92
4.3.5 Characterization by TPR	94
4.3.6 FTS activity.....	95
4.4 Conclusions.....	100
4.5 References.....	100
 V COMPARISON OF PdCo/SBA-15 PREPARED BY CO- IMPREGNATION AND SEQUENTIAL IMPREGNATION FOR FISCHER-TROPSCH SYNTHESIS	 104
5.1 Introduction.....	104
5.2 Experimental	106
5.2.1 Catalyst preparation	106
5.2.2 Catalyst characterization	107
5.2.3 Catalytic testing for FTS	108

CONTENTS (Continued)

	Page
5.3 Results and discussion	109
5.3.1 Catalyst Characterizations by XRD and TEM	109
5.3.2 Catalyst characterizations by DR-UV-vis	112
5.3.3 Catalyst characterizations by XANES and EXAFS	114
5.3.4 Characterization by N ₂ adsorption-desorption	118
5.3.5 Catalyst characterizations by TPR	120
5.3.6 Catalyst characterizations by FT-IR	122
5.3.7 Catalytic testing for FTS	123
5.4 Conclusions	127
5.5 References	127
VI CONCLUSIONS	132
APPENDICES	134
APPENDIX A FISCHER-TROPSCH EXPERIMENTS AND PRODUCT ANALYSIS	135
APPENDIX B CALIBRATION CURVE, SELECTED MOLAR FLOW RATE OF CATALYSTS AND ALPHA YIELD	155
APPENDIX C ADDITIONAL CHARACTERIZATION RESULTS	172
CURRICULUM VITAE	180

LIST OF FIGURES

Figure		Page
1.1	The representative image of the formation of ordered mesoporous silica (SBA-15)	6
1.2	Structures of P123 and TEOS	7
2.1	Detailed flow chart of the Fischer-Tropsch process	12
2.2	Carbon chain growth and termination sequences in FTS	14
2.3	Plots of various theoretical product distributions as a function of chain growth probability assuming ideal ASF kinetics	15
2.4	The experimental set up for incipient wetness impregnation	26
2.5	A schematic diagram of the proposed mechanism during precipitation using two microemulsion systems	29
3.1	The XRD peaks of calcined (A) and reduced (B) catalysts	44
3.2	TPR profiles of the catalysts in IP series (A) and RM series (B)	47
3.3	The DR-UV-vis spectra of all calcined catalysts	49
3.4	The DR-UV-vis spectra of all reduced catalysts.....	50
3.5	XANES spectra of reference material.....	52
3.6	The XANES spectrum of Co K-edge of calcined 10Co-IP and 10Co-RM (A) and reduced 10Co-IP and 10Co-RM (B).....	53
3.7	Details from the LCF fitting of calcined catalysts	57

LIST OF FIGURES (Continued)

Figure		Page
3.8	The k^3 -weighted magnitude of the Fourier Transform for calcined and reduced 10Co-IP (A), calcined and reduced 10Co-RM (B).....	58
3.9	Details from the LCF fitting of reduced catalysts.....	61
3.10	The XANES spectrum of catalysts (A and B), calcined IP and RM series; (C and D), reduced IP and RM series	62
3.11	CO conversion, H ₂ conversion and CH ₄ selectivity in IP (A) and RM series (B)	66
3.12	Mole fraction of olefins in linear hydrocarbon products from C ₂ –C ₉ (A), IP series; (B), RM series and (C), mole fraction of <i>n</i> -paraffins in the range of C ₂ –C ₄ and C ₅ –C ₉ of all catalysts.....	68
3.13	Mole fractions of alcohols in all linear hydrocarbons as a function of carbon number, (A), IP series, (B), RM series and (C), mole ratio of methyl branched hydrocarbons to linear C ₆ hydrocarbons product as a function of the catalysts	70
4.1	N ₂ adsorption–desorption isotherms of (A) SBA-15 and its supported catalysts and (B) SBA-15(M) and its supported catalysts.....	86
4.2	Pore size distribution; (A) SBA-15 and its supported catalysts and (B) (SBA-15(M) and its supported catalysts.....	87
4.3	(Top) SEM and (bottom) TEM micrographs of SBA-15 and SBA-15(M)	89

LIST OF FIGURES (Continued)

Figure		Page
4.4	XRD patterns of support and calcined catalysts: (A) and (B) low-angle range and (C) high-angle range	91
4.5	TEM images of calcined catalysts	92
4.6	XANES spectra of calcined catalysts.....	94
4.7	H_2 -TPR profiles of calcined catalysts	95
4.8	Conversions of CO and H_2 as a function of time on stream	97
4.9	Selectivity of 1-butene/2-butene (%C) as function of catalysts.....	99
5.1	XRD patterns: (A) low-angle, (B) high-angle of calcined catalysts and (C) high-angle of reduced catalysts.....	111
5.2	TEM images of calcined catalysts	112
5.3	DR-UV-Vis spectra of SBA-15 and catalysts.....	113
5.4	XANES spectrum of Co K-edge: (A) calcined catalysts, (B) reduced catalysts and EXAFS spectrum of Co K-edge, (C) calcined catalysts, (D) reduced catalysts	116
5.5	N_2 adsorption–desorption isotherms (A) and pore size distribution (B).....	119
5.6	H_2 -TPR profiles of 0.2Pd-10Co-CIP and 0.2Pd-10Co-SIP	121
5.7	FT-IR spectra of calcined catalysts.....	123
5.8	Catalytic performance on FTS: (A) CO conversions rate and (B) H_2 Conversions rate	125

LIST OF TABLES

Table		Page
2.1	Effect of catalyst precursor	19
2.2	Effect of support type to FTS activity.....	21
2.3	Effect of pore size support to FTS activity	25
3.1	The particle diameters and dispersions of different catalysts	45
3.2	Co K-edge energy position for calcined and reduced catalysts with respect to Co metal foil (7709 keV).....	54
3.3	Composition of calcined and reduced catalysts suggested by Linear Combination Fitting (LCF) of XANES spectra.....	55
4.1	Textural properties of SBA-15 and calcined catalysts determined by N ₂ adsorption–desorption and XRD.....	88
4.2	FTS activity, CO ₂ selectivity and hydrocarbon selectivities calculated at 8 h of time on stream	98
5.1	Co K-edge energy position for calcined and reduced catalysts with respect to Co metal foil (7709 keV).....	117
5.2	Composition of calcined and reduced catalysts suggested by Linear Combination Fitting (LCF) of XANES spectra.....	118
5.3	Textural properties of SBA-15 support and calcined catalysts as determined by N ₂ adsorption–desorption	119
5.4	FTS activity and hydrocarbon selectivity calculated at 8 h of time on stream.....	126

CHAPTER I

INTRODUCTION

1.1 Goals of thesis

The goals of thesis were to investigate the physicochemical properties and catalytic performance of supported cobalt (Co) catalysts containing 10 wt% of Co. The first part involved an investigation on the influence of preparation method of cobalt supported on silica, including incipient wetness impregnation and precipitation with reverse micelle technique (referred to as IP and RM) and palladium (Pd) as a promoter. The second part was a study to understand the effect of support morphology, including conventional SBA-15 and modified SBA-15 (referred to as SBA-15 (M)). The third part compared the effect of Pd addition methods, including co- and sequential impregnation methods on SBA-15 (referred to as CIP and SIP, respectively). The chemical and physical properties of all catalysts were investigated by X-ray diffraction (XRD), H₂-temperature programmed reduction (H₂-TPR), diffuse reflectance ultraviolet-visible spectroscopy (DR-UV-vis) and X-ray absorption spectroscopy (XAS, including X-ray absorption near edge structure (XANES) and extended X-ray absorption fine structure (EXAFS) spectroscopy), N₂ adsorption-desorption, scanning electron microscopy (SEM), transmission electron microscopy (TEM) and Fourier transform infrared spectroscopy (FT-IR). Finally, all catalysts were tested for Fischer-Tropsch synthesis (FTS) and the catalytic activity and product selectivity in C₅–C₉ range were determined.

1.2 Background of Fischer-Tropsch reaction

The FTS is a reaction between CO and H₂ (synthesis gas or syngas) in the presence of a heterogeneous catalyst to produce hydrocarbon compounds as a fuel. The FTS is interesting as an alternative method to produce fuel due to gradual decrease of natural oil resources (Diehl and Khodakov, 2009). The FT reaction can generate several types of hydrocarbon compounds that can be categorized based on the desired fuel ranges including lower olefins (C₂–C₄), gasoline (C₅–C₁₁), diesel fuel (C₁₂–C₂₀) and jet fuel (C₂₀₊) (Morales and Weckhuysen, 2006).

Among several catalysts for the FTS process, cobalt in metallic form (Co⁰) is widely used because it can be employed at low temperature and gives high selectivities for C₅₊ products. The catalytic activity and product selectivity are a function of reducibility of cobalt, which depends on the dispersion (González et al., 2009; Khodakov et al., 2003). In order to improve dispersion of metallic particles, cobalt precursors are dispersed on porous materials, such as SiO₂, Al₂O₃, and TiO₂. However, the reduction of Co species depends on the metal–support interactions which decrease in the order of Al₂O₃ > TiO₂ > SiO₂ (Jacobs et al., 2002). Although weak metal–support interactions between Co and SiO₂ support could attribute to a poor metal dispersion resulting in low CO conversion, the Co/SiO₂ gave the highest C₅₊ selectivity (Jacobs et al., 2002). Consequently, SiO₂ is still one of the most widely used catalyst supports for FTS reaction, because it can stabilize the active phase against loss of surface area during the reaction and facilitate the mass or heat transfer in the reactions (Khodakov, Chu, and Fongarl, 2007). The cobalt dispersion on SiO₂ depends on the preparation method (Khodakov, Chu, and Fongarl, 2007).

Zhang et al. (2007) studied silica-supported cobalt catalysts (Co/SiO_2) prepared by incipient wetness impregnation (IP) with cobalt nitrate in various solvents and found that the catalyst prepared from dehydrated ethanol had the highest dispersion and gave the best catalytic performance. Another method to produce cobalt catalyst with high dispersion is the precipitation using the reverse micelle method (RM). Fischer, Steen and Claeys (2011) used the RM method to synthesize Co_3O_4 crystallites in the nanometer size range (average sizes: 3–10 nm) supported on Al_2O_3 ($\text{Co}/\text{Al}_2\text{O}_3$). The cobalt in $\text{Co}/\text{Al}_2\text{O}_3$ from RM method contained metal with mainly a face-centered cubic (fcc) phase whereas that prepared by conventional method consisted of the mixed fcc and hexagonal close packed (hcp) (Bezemer et al., 2006; Enache et al., 2002). The catalytic activity of supported cobalt catalyst also depends on cobalt reducibility.

To enhance the reducibility of cobalt, which is well dispersed on a support, a small amount of noble metal such as Ru, Pt, Pd, Ir or Re can be added (Zhang et al., 2010; Khodakov, Chu, and Fongarl, 2007; Ma et al., 2012; Tsubaki, Sun, and Fujimoto, 2001; Xu et al., 2005; Lapidus et al., 2005). There are several reports about the use of Ru as a promoter for cobalt catalysts in the FTS process to enhance cobalt reducibility and CO conversion (Tsubaki, Sun, and Fujimoto, 2001; Xu et al., 2005). Other promoters including Pd are not extensively investigated for the FTS. Pd as a promoter on cobalt catalyst can act as adsorption sites for H_2 and increase hydrogenation rate in FTS (Ma et al., 2012; Xu et al., 2005). Such improvement could provide crucial paraffin products and prevent the formation of hard waxes, which are inactive carbons, a cause of catalyst deactivation (Morales and Weckhuysen, 2006; Guzzi et al., 2001). Guzzi et al. (2001) showed that an addition of Pd to Co/SiO_2

resulted in an increase in the relative fraction of alkanes during FTS. This effect was attributed to a higher concentration of surface hydrogen on the Pd promoter.

Another strategy to improve Co dispersion is changing the support with a high surface area. Mesoporous silica such as MCM-41, MCM-48 and SBA-15 has a large surface area, highly uniform mesopores and high thermal stability and has been used as a support for Co- and Fe-based FTS catalysts (Champson et al., 2010). In term of thermal stability, SBA-15 is superior to the others because it has a thick pore wall and large pore size (González et al., 2009). High dispersion of cobalt on SBA-15 (Co/SBA-15) enhanced reducibility of cobalt oxides and subsequently, the FTS activity (Champson et al., 2010). A further improvement in the conversions and selectivity of gasoline was made by changing the support to SBA-15 with different morphologies. Prieto et al. (2009) reported that a dispersion of bimetallic Ru-Co was influenced by the cavity length of SBA-15. Short cavity length eased a diffusion of CO to the catalyst active sites and gave a steady performance. Moreover, Pd is needed as a promoter to enhance the reducibility and act as H₂ activation site during FTS.

Recently, Satsuma et al. (2014) reported about effect of preparation method including co-impregnation and sequential impregnation of Pd-promoted Co/alumina for methane combustion. Bimetallic catalyst prepared from co-impregnation provided better mixing of Pd-Co and higher reactivity than that sequential impregnation. Thus, the effect of preparation method for Pd-promoted Co/SBA-15 by co- and sequential impregnation is interesting for the improvement of FTS.

1.3 Background of SBA-15

SBA-15 is a periodic mesoporous silicates, which has uniform channels with large pore size (2-40 nm), high surface area (up to 2000 m²/g), and high thermal stability (Zhao et al., 1998). The SBA-15 has been widely used as a support in various catalytic applications including acidic/basic catalysis, hydrogenation, desulfurization, oxidation, asymmetric synthesis, enzyme catalysis or Fischer-Tropsch synthesis. The main surface groups of dry SBA-15 are isolated silanols with some geminal and hydrogen-bonded silanols (Meer et al., 2010).

Among different mechanisms of the mesostructure formation, the most accepted one is self-assembled surfactants in an acidic solution between inorganic and organic periodic composite materials through hydrogen bonding ($S^0 H^+$)(XI^+) pathway where the S, I and X^- are surfactant, mineral species and halogen anions (Cl^- or Br^-), respectively (Zhao et al., 1998). In this mechanism the randomly ordered rod like micelles (formed from the self-organized surfactants) interact with the silica species to result tubular silica condensing around the external surface of the micelle rods and arrange to form hexagonal structure.

In general, there are four main steps in the SBA-15 preparation as shown in Figure 1.1. The first step is the formation of the mesoporous structure by mixing a surfactant which is a triblock copolymer (poly (ethylene glycol)-block-poly(propylene glycol)-block-poly(ethylene glycol), P123) and a silica precursor (tetraethyl orthosilicate, TEOS) in the presence of HCl solution. The second step is the hydrothermal treatment at a high temperature to generate tubular silica. The third step is filtrating and washing to remove residue Cl^- and the last step is calcination to remove the template.

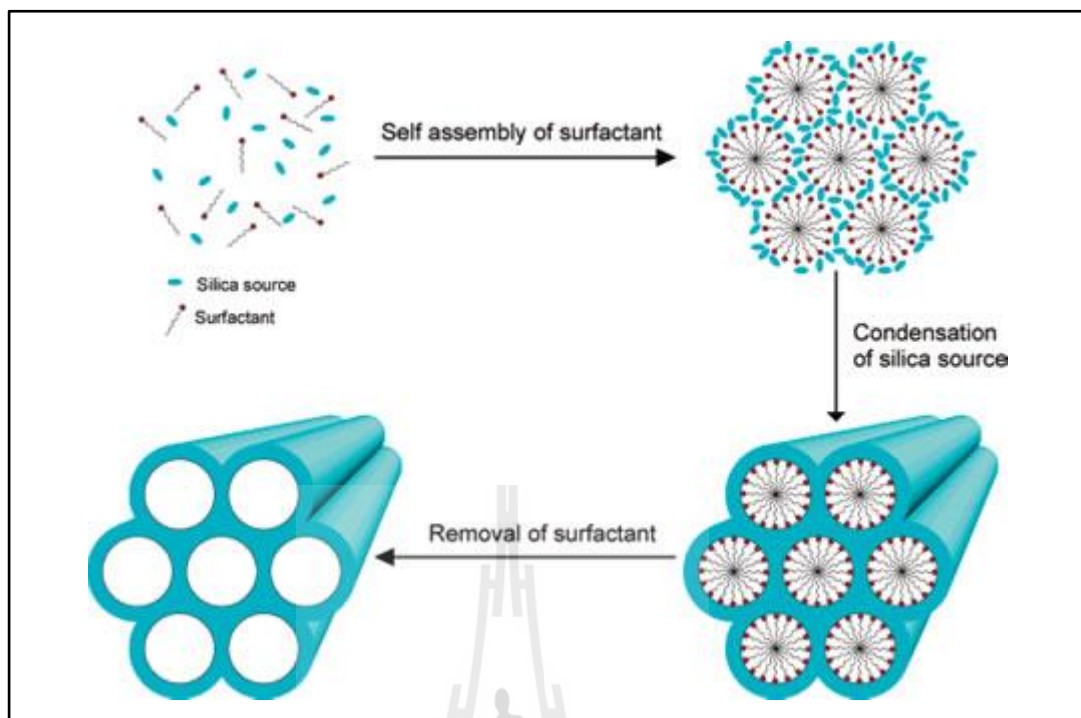


Figure 1.1 The representative image of the formation of ordered mesoporous silica (SBA-15) (Zhao et al., 1998).

The structure of TEOS and P123 can be seen in Figure 1.2. P123 is a triblock PEO-PPO-PEO copolymer which is an amphiphilic molecule where the PEO parts are hydrophilic and PPO part is hydrophobic. The amphiphilic behaviour of P123 makes it form spherical micelles in water with the PEO chains towards the water and the PPO chains in the core of the micelles (Zhao et al., 1998).

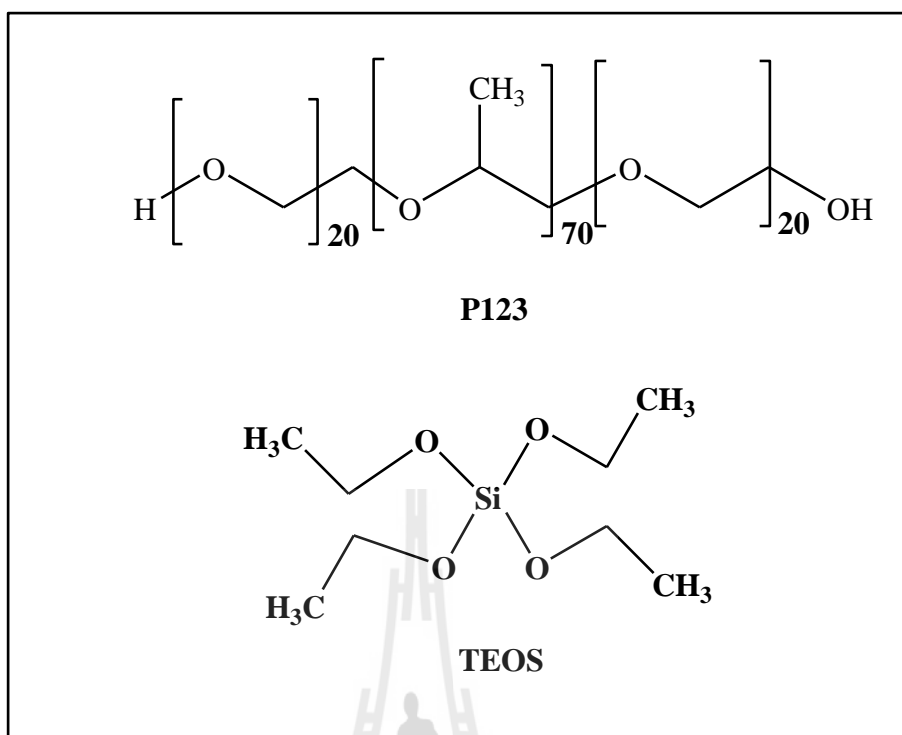


Figure 1.2 Structures of P123 and TEOS.

1.4 Scope and limitation of the study

SBA-15 and SBA-15(M) mesoporous silica were synthesized by procedures from literatures (Prieto et al., 2009; Zhang et al., 2006). All the Pd-Co catalysts contained 10 wt% Co and 0.2, 1 wt% Pd. All catalysts were activated in a reactor before FTS testing by using 60 mL/min of H₂ flow rate to 100 °C (heating rate 1 °C/min) and held at 100 °C for 1h then the temperature was increased to 350 °C (heating rate 1 °C/min) and the hold for 12 h. The FTS was tested at 230 °C under 5 bars of gas mixture for 480 min. The final gas mixture, N₂:H₂: CO was adjusted to volume ratio of 8:22:11 (total flow rate of 41 mL/min) corresponded to H₂: CO = 2.

1.5 References

- Bezemer, G. L., Bitter, J. H., Kuipers Herman, P. C. E., Oosterbeek, H., Holewijn, J. E., Xu, X., Kapteijn, F., van Dillen, A. J. and de Jong K. P. (2006). Cobalt particle size effects in the Fischer-Tropsch reaction studied with carbon nanofiber supported catalysts. **Journal of American Chemical Society**. 128: 39-56.
- Diehl, I. and Khodakov, Y. (2009). Promotion of cobalt Fischer-Tropsch catalysts with noble metals: A review. **Oil & Gas Science and Technology - Rev. IFP**. 64: 11-24.
- Enache, D. I., Rebours, B., Roy-Aubergier, M. and Revel, R. J. (2002). *In Situ* XRD study of the influence of thermal treatment on the characteristics and the catalytic properties of cobalt-based Fischer-Tropsch catalysts. **Journal of Catalysis**. 205: 346-353
- Fischer, N., Steen, V. and Claeys, M. (2011). Preparation of supported nano-sized cobalt oxide and fcc cobalt crystallites. **Catalysis Today**. 171: 174-179.
- Ghampson, I. T., Newman, C., Kong, L., Pier, E., Hurley, K. D., Pollock, R. A., Walsh, B. R., Goundie, B., Wright, J., Wheeler, M. C., Meulenberg, R. W., Desisto, W. J., Frederick, B. G. and Aulin, R. N. (2010). Effect of pore diameter on particle size, phase, and turnover frequency in mesoporous silica supported cobalt Fischer-Tropsch catalyst. **Applied Catalysis A: General**. 388: 57-67.
- González, O., Perez, H., Navarro, P., Almedia, L. C., Pacheco, J. G. and Montes, M. (2009). Use of different mesostructured materials based on silica as cobalt supports for the Fischer-Tropsch synthesis. **Catalysis Today**. 143: 140-147.

- Guczi, L., Borkó, L., Schay, Z., Bazin, D. and Mizukami, F. (2001). CO hydrogenation and methane activation over Pd-Co/SiO₂ catalysts prepared by sol/gel method. **Catalysis Today**. 65: 51-57.
- Jacobs, G., Patricia, P., Zhang, Y., Das, T., Li, J. and Davis, B. (2002). Fischer-Tropsch synthesis: deactivation of noble metal-promoted Co/Al₂O₃ catalysts. **Applied Catalysis A: General**. 233: 215-226.
- Khodakov, A., Bechara, R. and Griboval-Constant, A. (2003), Fischer-Tropsch synthesis over silica supported cobalt catalysts: mesoporous structure versus cobalt surface density. **Applied Catalysis A: General**. 254: 273-288.
- Lapidus, A. L., Tsapkina, M. V., Krylova, A. Y. and Tonkonogov, B. P. (2005). Bimetallic cobalt catalysts for the synthesis of hydrocarbons from CO and H₂. **Russian Chemical Reviews**. 74: 577-586.
- Ma, W., Jacobs, G., Keogh, R., Bukur, D. B. and Davis, B. H. (2012). Fischer-Tropsch synthesis: Effect of Pd, Pt, Re, and Ru noble metal promoters on the activity and selectivity of a 25%Co/Al₂O₃ catalyst. **Applied Catalysis A: General**. 437-438: 1-9.
- Meer, J., Bardez-Giboire, I., Mercier, C., Revel, B., Davidson, A. and Renaud, D. (2010). Mechanism of metal oxide nanoparticle loading in SBA-15 by the double solvent technique. **The Journal of Physical Chemistry C**. 114: 3507-3515.
- Morales, F. and Weckhuysen, B. (2006). Promotion effects in Co-based Fischer-Tropsch catalysis. **The Royal Society of Chemistry**. 19: 1-40.
- Prieto, G., Martínez, A., Murciano, R. and Arribas, M. A. (2009). Cobalt supported on morphologically tailored SBA-15 mesostructures: the impact of pore length

on metal dispersion and catalytic activity in the Fischer-Tropsch synthesis.

Applied Catalysis A: General. 367: 146-154.

Satsuma, A., Tojo, T., Okuda, K., Yamamoto, Y., Arai, S. and Oyama, J. (2014).

Effect of preparation method of Co-promoted Pd/alumina formethane combustion. **Catalysis Today.** 224: 308-314.

Tsubaki, N., Sun, S. and Fujimoto, K. (2001). Different functions of the noble metals

added to cobalt catalysts for Fischer-Tropsch synthesis. **Journal of Catalysis.** 199: 236-246.

Xu, D., Li, W., Duan, H., Ge, Q. and Xu, H. (2005). Reaction performance and

characterization of Co/Al₂O₃ Fischer-Tropsch catalysts promoted with Pt, Pd and Ru. **Catalysis Letters.** 102: 229-235

Zhang, Q., Kang, J. and Wang, Y. (2010). Development of novel catalysts for Fischer

-Tropsch synthesis: tuning the product selectivity. **ChemCatChem.** 2: 1030-1050.

Zhang, Y., Liu, Y., Yang, G., Sun, S. and Tsubaki, N. (2007). Effects of impregnation

solvent on Co/SiO₂ catalyst for Fischer-Tropsch synthesis: A highly active and stable catalyst with bimodalsized cobalt particles. **Applied Catalysis A:**

General. 321: 79-85.

CHAPTER II

LITERATURE REVIEWS

2.1 Fischer-Tropsch synthesis

Fischer-Tropsch synthesis (FTS) is a reaction between CO and H₂ (synthesis gas or syngas) in the presence of a heterogeneous catalyst to produce hydrocarbon compounds. This process was first reported in 1926 by two German chemists, Han Fischer and Franz Tropsch (Zhang et al., 2010). The FTS is interesting as an alternative method to produce fuels due to a gradual decrease of natural oil resources (Diehl and Khodakov, 2009).

The FTS technologies from different feedstocks for syngas, namely, coal, natural gas and biomass are referred to as coal-to-liquid (CTL), gas-to-liquid (GTL) and biomass-to-liquid (BTL), respectively. Type of feedstocks, fuels and corresponding applications are shown in Figure 1. Firstly, the feed stock is converted to syngas. Then, the reactions between CO and H₂ in FT-reactor produce several types of hydrocarbon compounds that can be categorized based on the desired fuel ranges including lower olefins (C₂–C₄), gasoline (C₅–C₁₁), diesel fuel (C₁₂–C₂₀) and jet fuel (C₂₀₊) (Morales and Weckhuysen, 2006).

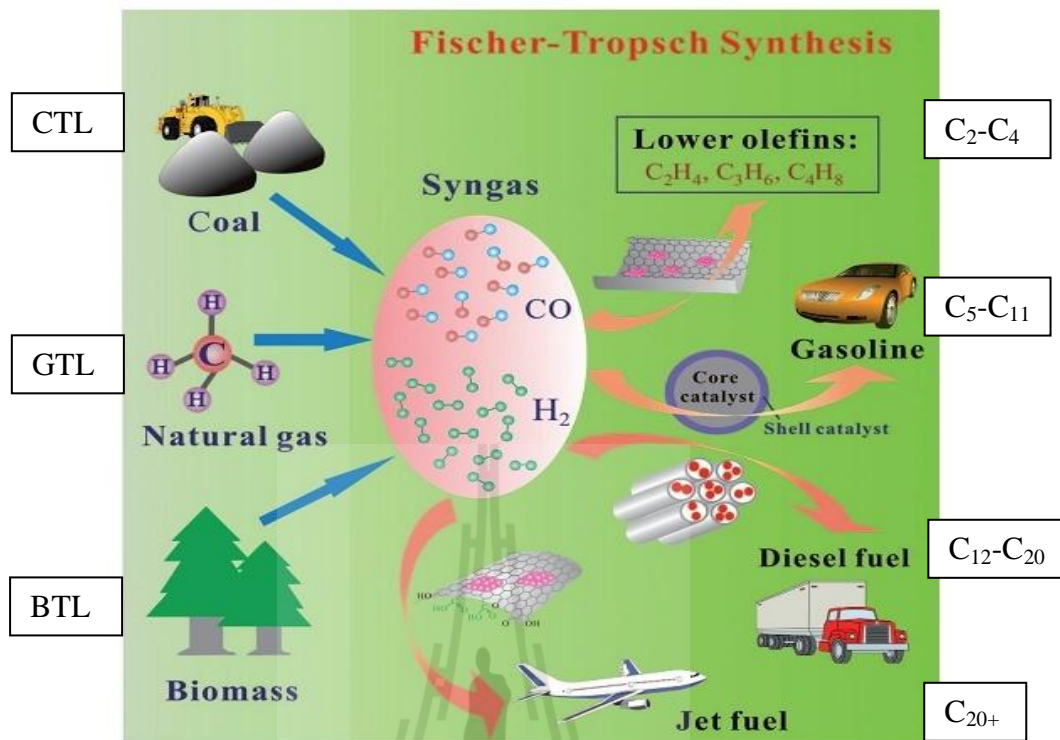


Figure 2.1 Detailed flow chart of the Fischer–Tropsch process (Zhang et al., 2010).

2.2 Chemistry of FTS process

There are two main reactions in FTS to generate alkane and alkene (equations 2.1 and 2.2). Both reactions are strongly exothermic ($\Delta H = -165$ to $-204 \text{ kJ}_{\text{CO}}^{-1}$). In general, the FTS reactions occur on a catalyst surface by adsorption of CO and H₂ followed by dissociation to various surface species. The reactions of the surface species produce alkyl chains which may be terminated by addition or elimination of hydrogen to produce paraffin (equation 2.1) or olefin (equation 2.2).



However, some oxygenate products (equation 2.3), water-gas-shift reaction (equation 2.4) and Boudouard reaction (equation 2.5) can occur in FTS process which give undesired hydrocarbon products (Diehl and Khodakov, 2009).



There are many questions about the mechanism of the FTS products. Various detailed mechanisms have been proposed while there are still controversial issues in the literatures. However, it is typically accepted that the FTS proceeds through a surface-catalyzed polymerization mechanism from dissociative adsorption of CO molecule to chemisorbed carbon and oxygen (C_s and O_s , respectively). The O_s can be efficiently removed by reactions with surface hydrogen, H_s to form water whereas the C_s reacts successively with H_s to yield various $(\text{CH})_x$ intermediates ($x = 0-3$). Then, the chain growth through C-C coupling starts, in competition with chain termination through hydrogenation, dehydrogenation, hydrogen abstraction, or insertion of nondissociatively adsorbed CO to produce alkanes, alkenes, or alcohols, respectively (Iglesia et al., 1997; Doss et al., 2012).

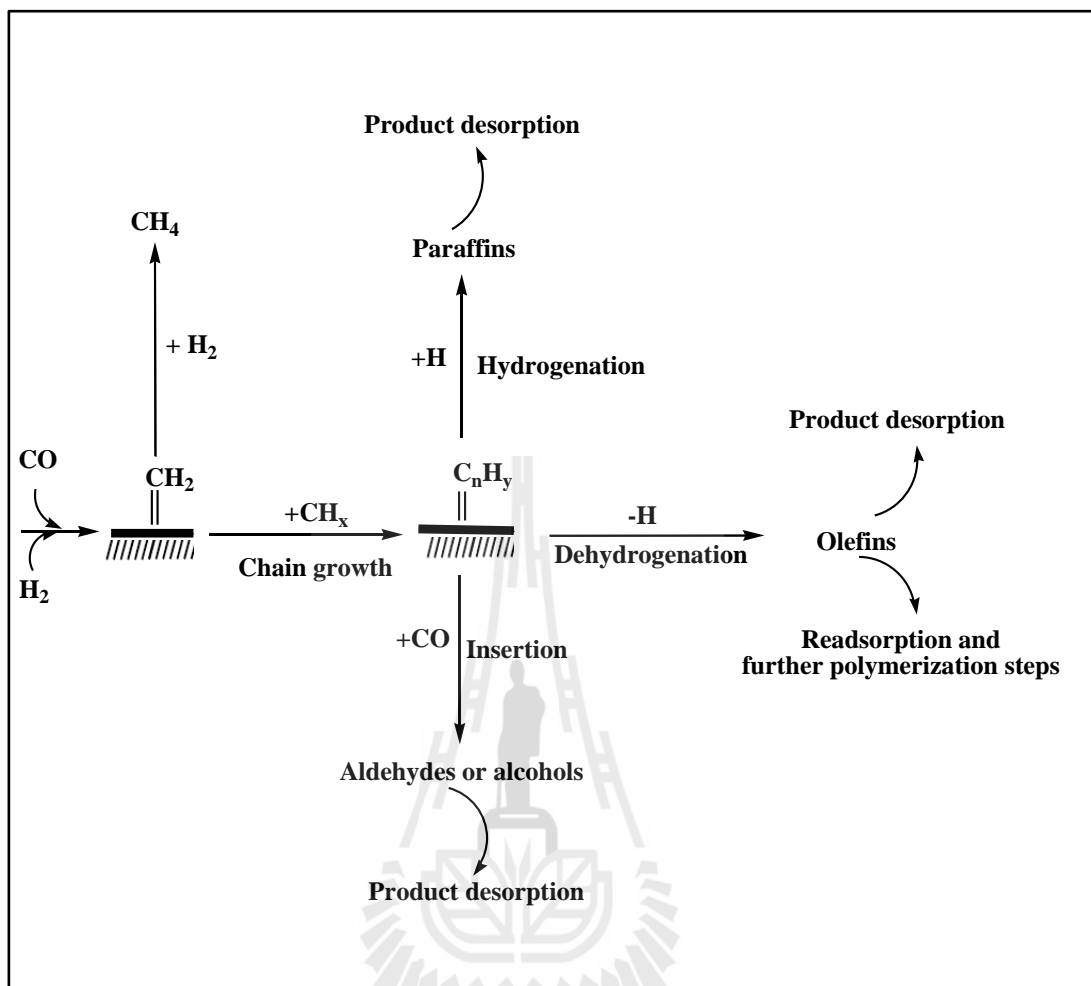


Figure 2.2 Carbon chain growth and termination sequences in FTS adapted from Doss et al., 2012.

2.3 Fischer-Tropsch product distribution

Although different mechanisms for the FTS have been proposed, all of them assume that the growth of the surface species has a stepwise mechanism sequence. This means there will be either chain growth of adsorbed species on the catalyst surface or desorption of the surface species from the catalyst surface as product (Cairns, 2008). Fraction of products with different chain length is related to chain growth probability as shown in Figure 2.2.

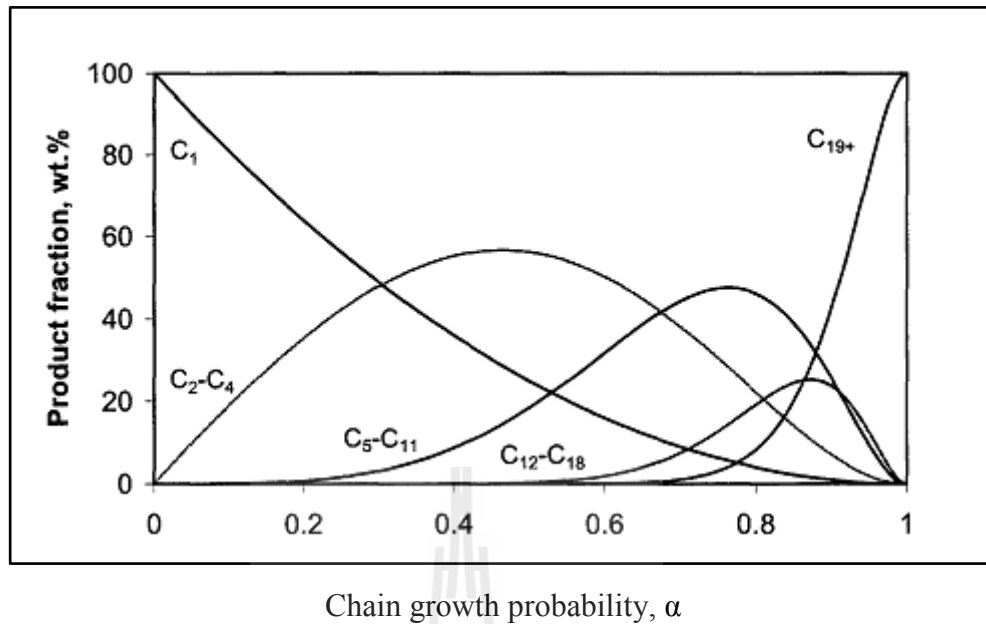


Figure 2.3 Plots of various theoretical product distributions as a function of chain growth probability assuming ideal ASF kinetics (Zhang et al., 2010).

The probability of the species on the surface growing by one carbon number (C_{n-1} to C_n) as opposed to desorbing is described as the chain growth probability (α_{n-1}). If α is independent of carbon number, it can be found from the Anderson-Schulz-Flory (ASF) plot:

$$\log\left(\frac{W_n}{n}\right) = n \log \alpha + \text{constant} \quad \dots\dots(2.6)$$

Where W_n is the mass fraction of the product species with carbon number n and α is the independent chain growth probability. This implies that the FTS is not selective towards any particular carbon number product range of product except methane where a 100 % selectivity would be true for a chain growth probability equal to zero. Figure 2.3 reveals the change in product weight fraction as the chain growth probability increases. It can be clearly seen that as the chain growth probability

increases, the molecular weight of the product increases. However, there are many factors that can affect FTS product selectivity including type of catalyst, promoter, catalyst support, temperature and pressure during reaction testing, flow rate of reactant and mole ratio of CO and H₂ (Khodakov et al., 2007).

2.4 Fischer-Tropsch catalysts

2.4.1 Active metal and promoter

Most of metals of the VIII group of the periodic table show noticeable activity in hydrocarbon synthesis from carbon monoxide and hydrogen (Diehl and Khodakov, 2009). Khodakov et al. (2007) mentioned that activities in the hydrogenation of CO to hydrocarbons in commercial production were high when Ru, Fe, Ni and Co were used. However, the Ni catalyst produced methane quantitatively under practical conditions; Ru is expensive and its worldwide reserves are insufficient for large-scale industry. Consequently, Co and Fe are preferred as catalysts in the industry for hydrocarbon synthesis because they are cheaper and provide higher efficiency in H₂ and CO uptake and lower methane product than Ni. Normally, Co and Fe give different product selectivity due to the different properties. Co catalyst gives a higher C₅₊ product selectivity while Fe produces higher water-gas-shift products and olefins. Moreover, Co is more resistant to deactivation than Fe. However, both Fe and Co catalysts are very sensitive to sulfur. In the part of Fe-based catalysts, the syngas should not contain more than 0.2 ppm of sulfur. Particularly for Co catalysts, the amount of sulfur in the feed should be much less than 0.1 ppm.

In this thesis, Co was used as the active metal for FTS because it was expected to provide higher selectivity for C₅₊ products. The Co catalyst could be

employed at lower temperature when compared with Fe (Diehl and Khodakov, 2009). Co catalyst can be operated at a lower temperature than Fe catalyst because of its higher reducibility, namely, oxides of cobalt can be reduced to active metallic form at a lower temperature than those of iron. To minimize the consumption quantity, Co is generally dispersed on a support which is a stable and porous material. However, highly dispersed cobalt may result in a strong metal-support interaction and the formation of cobalt silicate which leads to a lower reducibility (Kababji et al., 2009).

In order to enhance the reducibility of cobalt oxides, a small amount of noble metal such as Ru, Pt, Ir and Pd has been added as a promoter in FTS reaction. Ru is the most widely used one for many cobalt catalysts in FTS process because it gives a high CO conversion and high reducibility (Morales et al., 2006). Other promoters including Pd are scarcely investigated in FTS reaction. One should note that the presence of Pd promotion in cobalt catalyst enhances the hydrogenation reaction rate because Pd is a rich H₂ adsorption sites (Xu et al., 2005). The increase in hydrogenation rate of FTS could provide paraffin as a crucial hydrocarbon product as well as avoid formation of hard waxes as inactive carbons which cause catalyst poisoning. Moreover, Guzzi et al. (2001) showed that addition of Pd to Co silica-supported catalysts significant improved in the catalytic activity. Promotion with Pd resulted in an increase in the relative fraction of alkanes in the products of carbon monoxide hydrogenation. This effect was attributed to a higher concentration of hydrogen activation sites in the cobalt from the Pd promotor. With similar goal to increase the reducibility and hydrogenation rate, Pd was chosen as a promoter in this research.

2.4.2 Catalyst precursors

A type of catalyst precursor can affect the activity and selectivity of FTS. Panpranot et al. (2003) studied an effect of catalyst precursor of cobalt supported on MCM-41 in FTS. The catalyst prepared from $\text{Co}(\text{NO}_3)_2$ gave a higher FTS activity than those prepared from other catalyst precursors. Similar conclusion was reported by Martínez et al. (2003) who investigated an influence of catalyst precursor of cobalt supported on SBA-15. The catalyst prepared from $\text{Co}(\text{NO}_3)_2$ provided a higher FTS activity than those prepared from $\text{Co}(\text{OOCCH}_3)_2$ and $\text{Co}(\text{C}_5\text{H}_7\text{O}_2)_3$ (Table 2.1).

In addition, the effect of the type of Pd precursor was estimated. Xu et al. (2009) found that PdCl_2 gave the highest conversion in ethylene oxidation when compared with other Pd precursors including $(\text{NH}_4)_2\text{PdCl}_4$, $\text{Pd}(\text{NO}_3)_2$, $\text{Pd}(\text{NH}_3)_2\text{Cl}_2$ and $\text{Pd}(\text{C}_2\text{H}_3\text{O}_2)$ because it gave a better dispersion. Furthermore, Panpranot et al. (2005) disclosed a similar influence of different Pd precursors supported on SiO_2 and MCM-41 in 1-hexene hydrogenation (Table 2.1).

From literature review, the use of $\text{Co}(\text{NO}_3)_2$ and PdCl_2 as the precursors of the catalyst and promotor, respectively provided the highest activity for ethylene oxidation and 1-hexene hydrogenation. Both precursors were selected for this work.

Table 2.1 Effect of catalyst precursor.

Catalyst	Catalyst precursor	Reaction and condition	Activity	Reference
7Co/MCM-41	Co(NO ₃) ₂	Fischer-Tropsch synthesis; 0.1MPa, 220 °C. H ₂ /CO = 10	1.150 × 10 ⁴ (g _{CH₂} /g _{cat} ·h)	Panpranot., 2003.
	Co(OOCCH ₃) ₂		0.071 × 10 ⁴ (g _{CH₂} /g _{cat} ·h)	
	Co(C ₅ H ₇ O ₂) ₃		0.057 × 10 ⁴ (g _{CH₂} /g _{cat} ·h)	
	CoCl ₂		0.050 × 10 ⁴ (g _{CH₂} /g _{cat} ·h)	
20Co/SBA-15	Co(NO ₃) ₂	Fischer-Tropsch synthesis; 2MPa, 220 °C. H ₂ /CO = 2	23.1 (% Conversion)	Martínez., et al., 2003
	Co(OOCCH ₃) ₂		5.5 (% Conversion)	
	Co(C ₅ H ₇ O ₂) ₃		5.0 (% Conversion)	
1Pd-SiW ₁₂ /SiO ₂	PdCl ₂	Ethylene oxidation; 0.6MPa, 150 °C	5.4 (% Conversion)	Xu et al., 2009.
	(NH ₄) ₂ PdCl ₄		4.8 (% Conversion)	
	Pd(NO ₃) ₂		3.9 (% Conversion)	
	Pd(NH ₃) ₂ Cl ₂		2.2 (% Conversion)	
	Pd(C ₂ H ₃ O ₂)		3.0 (% Conversion)	
0.5Pd/SiO ₂	PdCl ₂	1-Hexene hydrogenation; 0.1MPa, 25 °C	8.5 × 10 ³ (mol/min/g _{cat})	Panpranot., 2005.
	Pd(NO ₃) ₂		4.0 × 10 ³ (mol/min/g _{cat})	
	Pd(C ₂ H ₃ O ₂)		5.0 × 10 ³ (mol/min/g _{cat})	
0.5Pd/MCM-41	PdCl ₂		8.3 × 10 ³ (mol/min/g _{cat})	
	Pd(NO ₃) ₂		4.0 × 10 ³ (mol/min/g _{cat})	
	Pd(C ₂ H ₃ O ₂)		4.1 × 10 ³ (mol/min/g _{cat})	

2.4.3 The catalyst supports

Both structure and catalytic performance of Co catalysts depended on type of supports which are stable materials with high surface area. The main role of supports is to disperse active phase on their high surface area, stabilize the active phase against a loss of surface area during the reaction, maintain the catalyst mechanical strength and facilitate a mass or heat transfer in a diffusion-limited or an exothermic reaction (Diehl and Khodakov, 2009). In this work, the support materials were used to disperse Co and produce stable Co metal particles after reduction. The structure of the porous support could control the sizes of the Co particles. Among several metal oxides, SiO₂, Al₂O₃ and TiO₂ are probably the most extensively investigated supports for Co catalysts. As known that the FTS is an exothermic reaction, catalytic supports also dissipate the heat released by the FT reaction and thus reduce a temperature gradient in fixed bed reactors.

In addition, the support can affect the structure and electronic properties of small cobalt metal particles. Electron-donor support can enrich in electron density of the cobalt active phase and facilitate cleavage of the C-O bond in adsorbed carbon monoxide. The support may react with cobalt species forming cobalt-support mixed compounds (Khodakov et al., 2007). There are many papers which reported the effect of the supports. Jacobs et al. (2002) studied catalytic performance of Co catalysts supported on SiO₂, Al₂O₃, and TiO₂. They found that the metal-support interactions affected the reduction of Co species and the strength of such interactions decreased in the order Al₂O₃ > TiO₂ > SiO₂. Moreover, a noble metal promoter, such as Ru or Pt,

significantly enhanced the reduction of Co species and thus increased the initial activity of Al₂O₃- and TiO₂-supported Co catalysts.

Additionally, Ma et al. (2006) were among authors who investigated bimetallic Fe-Co catalysts on SiO₂, Al₂O₃, AC₁, and AC₂ (AC₁= coconut shell activated carbon, AC₂ = coal activated carbon) prepared with the same technique. The FT activity decrease in order of Fe-Co/SiO₂ > Fe-Co/AC₁ > Fe-Co/Al₂O₃ > Fe-Co/AC₂ because the oxide-support interaction of Fe-Co/SiO₂ catalyst was weaker than that of the other catalysts and metal oxide dispersion and the size of the particles are more effective for Fischer-Tropsch synthesis.

Table 2.2 Effect of support type to FTS activity.

Catalyst	% CO Conversion	Reaction condition	Reference
Fe-Co/SiO ₂	50.3	1.5 MPa, 220 °C. H ₂ /CO	Ma et al., 2006
Fe-Co/AC ₁	38.8	= 1.6	
Fe-Co/Al ₂ O ₃	28.7		
Fe-Co/AC ₂	28.6		
Co/SiO ₂	64.7	3.5 MPa, 230 °C. H ₂ /CO	Jacobs et al., 2002
Co/Al ₂ O ₃	22.7	=2	
Co/TiO ₂	58.4		
Co/SiO ₂	42.5	1MPa, 250 °C. H ₂ /CO =2	González et al., 2009
Co/SBA-15	63.2		
Co/Al-MCM-41	38.5		
Co/MM1	40.3		

Saib et al. (2002) investigated the effect of pore diameter of silica-supported cobalt catalyst on FTS. The catalysts were prepared by impregnation using silica-support with various pore diameters (2, 4, 6, 10 and 15 nm). When the diameter of the support was 2 nm, cobalt resided outside the pores and was reduced easily. For the other diameters, cobalt species was inside the pores; the particle size and degree of reduction increased with increasing pore diameter. The larger particle size or poorer dispersion was obtained from the supports with an average pore diameter from 4 nm. Results from temperature programmed reduction (TPR) showed that amount of hydrogen consumed for the reduction of cobalt species inside the pores increased as the pore diameter of support increased because of a decrease in surface area of support. Silica gel has approximately a constant number of silanol groups per unit surface area. Therefore, it might be assumed that the increase in silanol groups might cause an increase in the formation of cobalt silicate species which can be reduced only at high temperatures.

The above results by Saib et al. (2002) were consistent with a report by Song and Li (2006) who also studied the effect of pore size of silica support on the catalytic performance of cobalt for FTS. The catalysts were prepared by incipient wetness impregnation on silica with average pore diameter of 2.4, 6.8, 10.4 and 15.8 nm. The influence of pore size on the reduction behavior was studied by TPR. The trend of interaction between cobalt oxide and support seemed to be similar to that reported by Saib et al. (2002). The interaction of cobalt oxide species with support became weaker as the support pore size increased. For the support with pore size smaller than 6.8 nm,

strong interaction with cobalt was formed and it was difficult to decompose the catalyst precursor during calcination. As mentioned about properties of heterogeneous catalyst, not only high reducibility of catalysts but also good dispersion on the support is needed. Nevertheless, the catalyst that is easy to reduce usually has poor dispersion. Thus, optimization is necessary. Design of catalysts with high reducibility and dispersion is a challenge for many researchers.

Besides the ordinary silica, highly ordered mesoporous silica including MCM-41, MCM-48, SBA-15 have been employed as supports for Co and Fe based Fischer-Tropsch catalysts (Champion et al., 2010) because of high surface area, thermal stability and large pore size. The structure of ordered mesoporous silica and formation mechanism is shown in Figure 1.1. SBA-15 has properties superior to other mesoporous silica because it has higher thermal stability due to larger pore size and thicker pore wall. Khodakov et al. (2002) were among the pioneers to use MCM-41 and SBA-15 as the supports for FTS reaction. The effect of pore size (namely 2, 2.5, 4.2, 9.1, 28 and 33 nm) were studied in FTS over cobalt catalysts prepared by incipient wetness impregnation. They revealed that FTS reaction rates were much higher on cobalt catalysts on the support with the pore diameter of 3 nm or larger. The larger diameter of support pores also led to significantly higher C_{5+} selectivity. Similar to the ordinary silica, the catalytic effects depended on cobalt particle size and reducibility which depended on pore size of mesoporous materials.

Moreover, there was an interesting report by González and co-workers in 2009 about the effect of various mesostructured materials based on silica as cobalt support for FTS. When different materials, SiO_2 , SBA-15, Al-MCM-41 and INT-MM1 with pore diameter of 8.4, 4.9, 3.2 and 2.6 nm, respectively were used as the

supports for cobalt with 20wt%, the percent reduction of cobalt were 94, 81, 44 and 36%. When tested for FTS, the Co/SBA-15 catalyst revealed the highest conversion and C₅₊ selectivity because the Co on SBA-15 with pore diameter about 5 nm was more reducible than that on Al-MCM-41 and INT-MM1. Even though Co supported SiO₂ could be reduced more easily than that on SBA-15, the latter showed better FTS performance because of better Co dispersion. According to high reducibility of cobalt on SiO₂ and SBA-15, these materials were used as Co supports in this work.

Mu et al. (2010) studied influence of zirconia (ZrO₂) addition on SBA-15 to supported cobalt catalysts for FTS. The Co dispersion was improved because zirconia prevented sintering of Co. Prieto et al. (2009) disclosed the interesting result on the impact of pore length on metal dispersion of Co supported on morphologically tailored SBA-15. The pore size of SBA-15 was fixed in a range of 8-10 nm while the pore length was varied as 5.7, 1.15 and 0.33 μm . After loading 1wt% Ru-20wt% Co, the catalyst supported on short pore length SBA-15 (0.33 μm) provided the highest CO conversion because of good Co dispersion and the facilitated pore diffusional access of CO even when the pores were wax-filled. In contrast, the catalyst supported on long pore length SBA-15 gave low CO conversion because of poor Co dispersion owing to the effect of catalyst sintering from the longer pore-residence time during calcination.

Table 2.3 Effect of pore size support of FTS activity.

Support	Pore size (nm) (support)	% Co Reduction	% CO conversion	Reaction condition	Reference
Co/SiO ₂ -1	2.4	17.2	19.3	1MPa, 230	Song and Li
Co/SiO ₂ -2	6.8	51.6	65.7	°C,	et al., 2006
Co/SiO ₂ -3	10.4	47.6	56.5	H ₂ /CO =2	
Co/SiO ₂ -4	15.7	13.2	8.7		
Co/MCM-41	3.2	16.3	27.6=TOF (10 ⁻⁴ s ⁻¹)	1MPa, 240	Ghampson et
Co/MCM-48	3.3	28.4	27.7=TOF (10 ⁻⁴ s ⁻¹)	°C,	al., 2010
Co/SBA-15	10	83.4	99.1=TOF (10 ⁻⁴ s ⁻¹)	H ₂ /CO =1	
Co/SiO ₂	22.3	96.6	95.2=TOF (10 ⁻⁴ s ⁻¹)		
Co/SBA-15-1	10	-	2.45=TOF (10 ⁻⁴ s ⁻¹)	0.1MPa, 190 °C,	Khodakov et al. 2003
Co/SBA-15-2	33	-	1.60=TOF (10 ⁻⁴ s ⁻¹)	H ₂ /CO =2	

2.4.4 Synthesis of cobalt catalyst for FTS

The performance of FTS catalysts also depends on the preparation methods. Several methods have been used to prepare cobalt catalyst including impregnation, co-precipitation, deposition-precipitation, sol-gel, colloidal, micro-emulsion, and solvated metal atom dispersion. One of the most common methods is incipient wetness impregnation. This method is simple and metal loading can be easily varied.

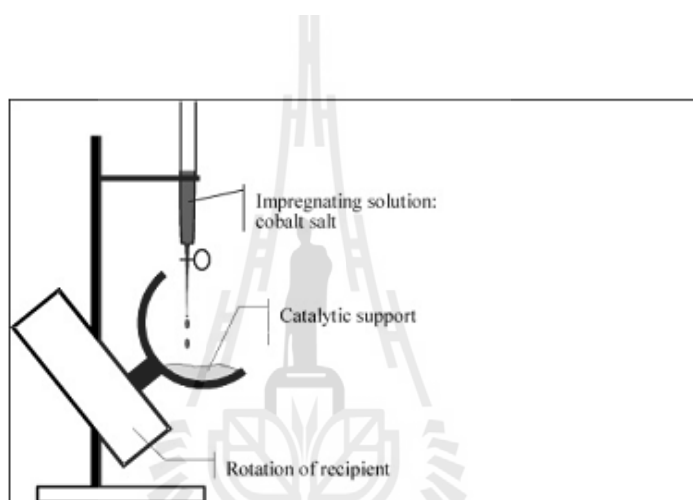


Figure 2.4 The experimental set up for incipient wetness impregnation (Khodakov et al., 2007).

In the incipient wetness impregnation, a solution of cobalt salt, typically cobalt nitrate, is brought to contact with a dry porous support. The solution then diffuses to fill the support pores. The incipient wetness occurs when the solution volume is just enough to completely fill all pores of the support. Although the incipient wetness impregnation is simple, the fundamentals during the process including drying are extremely complex. By using experimental setup as shown in Figure 2.4, reproducible preparation requires careful control of all impregnation parameters: temperature and time to dry the support before and after impregnation and

rate of addition of impregnating solution (Khodakov et al., 2007). Steen et al. (1996) proposed a method to prepare cobalt on SiO₂ to avoid formation of cobalt silicate and catalyst sintering by using solvents with high polarity (water, acetone or ethanol) since low polarity favor interaction with silanol groups. They also dried the samples at moderately high temperature (120 °C – 150 °C) over 10-24 hours and calcined at low temperature (200 °C – 300 °C) with slow heating rate (0.5-1 °C/min) from ambient temperature to desired temperature.

As mentioned that the dispersion of catalyst has direct influence to FTS-activity owing to number of active sites. In order to improve the catalyst dispersion, Zhang et al. (2007) prepared silica-supported cobalt catalysts by incipient-wetness impregnation with cobalt nitrate in different solvents including water, methanol, ethanol, acetone, n-propanol, DMF, THF and cyclohexane. They disclosed that the Co/SiO₂ catalyst prepared from absolute ethanol had the highest Co dispersion and gave the highest CO conversion with high α yield.

Traditionally, supported catalysts can be produced by wet impregnation using aqueous solution to give well-dispersed catalysts with high activity and good thermal stability. The average crystallite size of the active phase is usually in the nanometer range but with a broad size distribution. Therefore, the wet impregnation technique does't has a good control over the crystallite size.

According to the popularity of nanocatalyst, precipitation by water-in-oil microemulsion (reverse micelle) is one of several techniques with favorable reaction conditions producing the nanocatalyst with narrow size distribution without aggregation of crystallites (Mabaso, 2005). The water-in-oil microemulsion system is an isotropic dispersion of the aqueous phase in the continuous oil phase. In this

technique, synthesis of nanosized crystallites is based on the principle of confining the precipitation or reduction of precursors in the tiny aqueous droplets (see Figure 2.5). When a soluble metal salt is incorporated in the aqueous phase of the microemulsion, it will reside in the aqueous microdroplets surrounded by oil. Precipitation can be carried out when droplets containing the metal solution and the precipitating or reducing agent solution collide with each other. Each of these droplets will thus become a nanosized reactor for forming nanosized solid crystallites and the size of the "reactors" will ultimately determine the resulting crystallite size. A decrease in the water to surfactant ratio is expected to yield smaller droplets and thus the resulting metal crystallites after precipitation is expected to become smaller. The reverse micelle structure provides appropriate range of metal particle size by regulating the nucleation and growth process. In fact, it is the dynamics of micellar dispersions that make microemulsions so appropriate for this application. The droplets are subject to brownian motion and collide continuously, leading to the formation of short-lived dimers and to the exchange of the aqueous contents of the micelles. This dynamic process ensures a homogeneous repartition of the reactants among the aqueous droplets and thus the formation of very mono-dispersed crystallites.

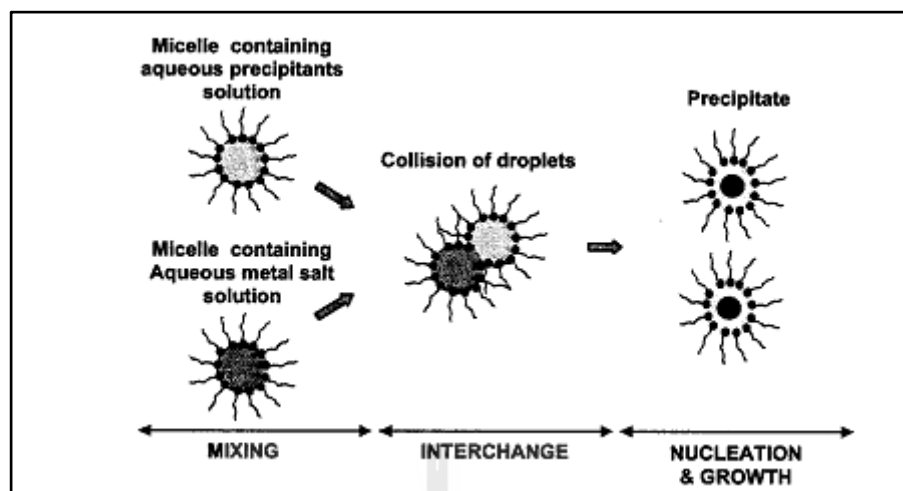


Figure 2.5 A schematic diagram of the proposed mechanism during precipitation using two microemulsion systems (Mabaso, 2005).

Fischer et al. (2011) displayed a new method to produce Co_3O_4 crystallites supported on Al_2O_3 in the nanometer size range (average sizes: 3–10 nm) utilizing reverse micelles and found that metal crystalline the prepared catalyst only showed the diffraction pattern of a face-centred cubic (fcc) phase. In contrast, a mixture of fcc and hcp cobalt were obtained in other methods. Furthermore, almost complete reduction of the Co catalyst could be obtained for all crystallite sizes from reverse micelle method.

From the information above, impregnation and reverse micelle methods were used in this study to prepare cobalt catalysts supported on SiO_2 . The better method was selected for further preparation of cobalt catalysts supported on SBA-15 and SBA-15(M)

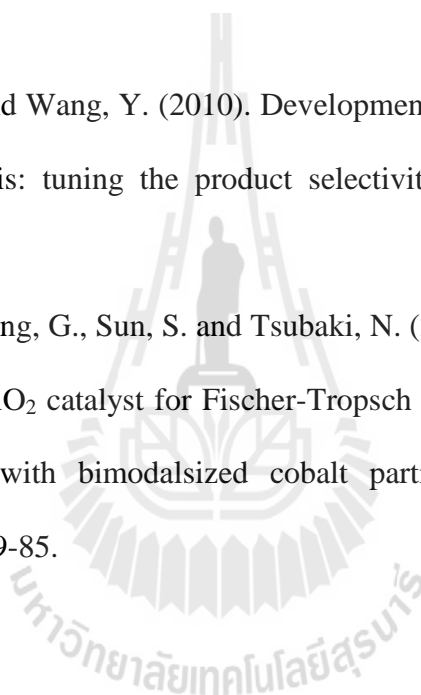
2.5 References

- Cairns, P. (2008). **Oxygenates in Iron Fischer-Tropsch Synthesis: Is copper a selectivity promoter?**. Ph.D. Thesis, University of Cape Town, South Africa.
- Diehl, I. and Khodakov, Y. (2009). Promotion of cobalt Fischer-Tropsch catalysts with noble metals: a review. **Oil & Gas Science and Technology - Rev. IFP**. 64: 11-24.
- Doss, T. P. (2012). **Low Severity Fischer-Tropsch synthesis for the production of synthetic hydrocarbon fuels**. Ph.D. Thesis, Aston University, United State of America.
- Fische, N., Steen, V. and Claeys, M. (2011). Preparation of supported nano-sized cobalt oxide and fcc cobalt crystallites. **Catalysis Today**. 171: 174-179.
- González, O., Perez, H., Navarro, P., Almedia, L.C., Pacheco, J. G. and Montes, M. (2009). Use of different mesostructured materials based on silica as cobalt supports for the Fischer-Tropsch synthesis. **Catalysis Today**. 143: 140-147
- Guczi, L., Borkó, L., Schay, Z., Bazin, D. and Mizukami, F. (2001). CO hydrogenation and methane activation over Pd-Co/SiO₂ catalysts prepared by sol/gel method. **Catalysis Today**. 65: 51-57.
- Iglesia, E. (1997). Design, synthesis, and use of cobalt-based Fischer-Tropsch synthesis catalysts. **Applied Catalysis A: General**. 161: 59-78.
- Jacobs, G., Das, P. K., Zhang, Y., Li, J., Racoillet, G. and Davis, B. H. (2002). Fischer - Tropsch synthesis: support, loading, and promoter effects on the reducibility of cobalt catalysts. **Applied Catalysis A: General**. 233: 263-281.

- Kababji, A. H., Joseph, B. and Woln, J. T. (2009). Silica-supported cobalt catalyst for Fischer-Tropsch synthesis: effect of calcination temperature and support surface area on cobalt silicate formation. **Catalysis Letters**. 130: 72-78.
- Khemthong, P., Klysubun, W., Prayoonpokarach, S. and Wittayakun, J. (2010). Reducibility of cobalt species impregnated on NaY and HY zeolites. **Materials Chemistry and Physics**. 121: 131-137.
- Khodakov, Y., Chu, W. and Fongarland, P. (2007). Advances in the development of novel cobalt Fischer-Tropsch catalysts for synthesis of long-chain hydrocarbons and clean fuels. **Chemical Reviews**. 107: 1692-1744.
- Khodakov, Y., Constant, A. G., Bechara, R. and Zholobenko, V. L. (2002). Size effects in Fischer Tropsch synthesis over cobalt-supported mesoporous silicas. **Journal of Catalysis**. 206: 230-241.
- Klysubun, W., Thanawan, S., Thamasirianunt, P., Radabutra, S. and Sombunchoo, P. (2007) Determination of chlorine content in chlorinated, vulcanized natural rubber by XANES. **Nuclear Instruments and Methods in Physics Research A**. 582: 242-244.
- Kukovecz, Á., Kánya, Z., Mőnter, D., Reschetilowski, W. and Kiricsi, I. (2001). UV-VIS investigation on Co, Fe and Ni incorporated into sol-gel SiO₂-TiO₂ matrices. **Journal of Molecular Structure**. 563: 403-407.
- Ma, X., Sun, Q., Cao, F., Ying W. and Fang, D. (2006). Effects of the different supports on the activity and selectivity of iron-cobalt bimetallic catalyst for Fischer-Tropsch Synthesis. **Journal of Natural Gas Chemistry**. 15: 335-339.
- Mabaso, E. H. (2005). **Nanosized iron crystallites for Fischer-Tropsch Synthesis**. Ph.D. Thesis, University of Cape Town, South Africa.

- Martínez, A., López, C., Márquez, F. and Díaz, I. (2003). Fischer-Tropsch synthesis of hydrocarbons over mesoporous Co/SBA-15 catalysts: the influence of metal loading, cobalt precursor, and promoters. **Journal of Catalysis**. 220: 486-499.
- Morales, F. and Weckhuysen, B. (2006). Promotion effects in Co-based Fischer-Tropsch catalysis. **Catalysis**. 19: 1-40.
- Mu, S., Li, D., Hou, B., Jia, L., Chen, J. and Sun, Y. (2010). Influence of ZrO₂ loading on SBA-15-supported cobalt catalysts for Fischer-Tropsch synthesis. **Energy Fuels**. 24: 3715-3718.
- Panpranot, J., Kaewkun, S., Praserttham, P. and Goodwin Jr., J. G. (2003). Effect of cobalt precursors on the dispersion of cobalt on MCM-41. **Catalysis Letters**. 19: 1-2.
- Panpranot, J., Tangjitwattakorn, O., Praserttham, P. and Goodwin Jr, J. G. (2005). Effects of Pd precursors on the catalytic activity and deactivation of silica-supported Pd catalysts in liquid phase hydrogenation. **Applied Catalysis A: General**. 292: 322-327.
- Prieto, G., Martínez, A., Murciano, R. and Arribas, M. A. (2009). Cobalt supported on morphologically tailored SBA-15 mesostructures: the impact of pore length on metal dispersion and catalytic activity in the Fischer-Tropsch synthesis. **Applied Catalysis A: General**. 367: 146-15.
- Saib, A. M., Claeys, M. and Steen, E. (2002). Silica supported cobalt Fischer-Tropsch catalysts: effect of pore diameter of support. **Catalysis Today**. 71: 395-402.
- Song, D. and Li, J. (2006). Effect of catalyst pore size on the catalytic performance of silica supported cobalt Fischer-Tropsch catalysts. **Journal of Molecular Catalysis A: Chemical**. 247: 206-212.

- Xu, D., Li, W., Duan, H., Ge, Q. and Xu, H. (2005). Reaction performance and characterization of Co/Al₂O₃ Fischer-Tropsch catalysts promoted with Pt, Pd and Ru. **Catalysis Letters**. 102: 229-235.
- Xu, S., Wang, L., Chua, W. and Yang, W. (2009). Influence of Pd precursors on the catalytic performance of Pd-H₄SiW₁₂O₄₀/SiO₂ in the direct oxidation of ethylene to acetic acid. **Journal of Molecular Catalysis A: Chemical**. 310: 138-143.
- Zhang, Q., Kang, J. and Wang, Y. (2010). Development of novel catalysts for Fischer-Tropsch synthesis: tuning the product selectivity. **ChemCatChem**. 2: 1030-1050.
- Zhang, Y., Liu, Y., Yang, G., Sun, S. and Tsubaki, N. (2007). Effects of impregnation solvent on Co/SiO₂ catalyst for Fischer-Tropsch synthesis: A highly active and stable catalyst with bimodally sized cobalt particles. **Applied Catalysis A: General**. 321: 79-85.



CHAPTER III

PALLADIUM-PROMOTED COBALT CATALYSTS

SUPPORTED ON SILICA PREPARED BY

IMPREGNATION AND REVERSE MICELLE FOR

FISCHER-TROPSCH SYNTHESIS

Abstract

The objectives of this work were to compare physicochemical properties of silica-supported cobalt catalysts (with 10 wt% Co) prepared by impregnation (10Co-IP) and precipitation using a reverse micelle technique (10Co-RM) and to investigate influence of palladium as a promoter (0.2 wt% and 1.0 wt%) on properties of 10Co-IP and 10Co-RM. The catalysts were characterized by XRD, H₂-TPR, DR-UV-vis, XANES and EXAFS. The reactivity during Fischer-Tropsch synthesis (FTS) was tested at 230 °C, 5 bar with H₂/CO = 2. The particle size of Co₃O₄ in 10Co-IP was larger than that of 10Co-RM which could contribute to lower selectivity to methane and C₂–C₄ paraffin products. The addition of 0.2 wt% Pd to 10Co-IP and 10Co-RM enhanced the cobalt reducibility, FTS activity and paraffin selectivity. On the other hand, the addition of 1.0 wt% Pd resulted in increased methane formation and lower CO conversion. The most suitable catalyst from this work was 0.2Pd-10Co-IP that gave high CO conversion (34.8%) and high mole fraction of paraffins (0.38) in the gasoline range (C₅–C₉).

3.1 Introduction

The Fischer-Tropsch synthesis (FTS) is a reaction of syngas, which is a mixture of carbon monoxide (CO) and hydrogen (H₂) to produce hydrocarbon and oxygenated compounds (Zhang et al., 2010). The FTS process is interesting in both industrial and academic fields due to the limited petroleum resources and increasing oil price (Diehl and Khodakov, 2009; Morales and Weckhuysen, 2006). Among several catalysts for the FTS process, cobalt in metallic form (Co⁰) is widely used because it can be employed at low temperature and gives high selectivities for C₅₊ products. The catalytic activity and product selectivity are a function of reducibility of cobalt, which depends on the dispersion (González et al., 2009; Khodakov et al., 2003).

In order to improve dispersion of metallic particles, cobalt precursors are dispersed on porous materials such as SiO₂, Al₂O₃ and TiO₂. However, the reduction of Co species depended on the metal–support interactions which decreased in the order Al₂O₃ > TiO₂ > SiO₂ (Jacobs et al., 2002). Although weak metal–support interactions between Co and SiO₂ support could attribute to a poor metal dispersion resulting in low CO conversion, the Co/SiO₂ gave the highest C₅₊ selectivity (Jacobs et al., 2002). Consequently, SiO₂ is still one of the most widely used catalyst supports for FTS reaction because it can stabilize the active phase against loss of surface area during the reaction and to facilitate the mass or heat transfer in the reactions (Khodakov, Chu, and Fongarl, 2007). The cobalt dispersion on SiO₂ depends on the preparation method (Khodakov, Chu, and Fongarl, 2007). Zhang et al. (2007) studied silica-supported cobalt catalysts (Co/SiO₂) prepared by incipient wetness impregnation (IP) with cobalt nitrate in various solvents and found that the catalyst

prepared from dehydrated ethanol had the highest dispersion and gave the best catalytic performance. Another method to produce cobalt catalyst with high dispersion is the precipitation using the reverse micelle method (RM). Fischer, Steen and Claeys (2011) used the RM method to synthesize Co_3O_4 crystallites in the nanometer size range (average sizes: 3–10 nm) supported on Al_2O_3 ($\text{Co}/\text{Al}_2\text{O}_3$). The cobalt in $\text{Co}/\text{Al}_2\text{O}_3$ from RM method contained metal with mainly a face-centered cubic (fcc) phase whereas that prepared by conventional method consisted of the mixed fcc and hexagonal close packed (hcp) (Bezemer et al., 2006; Enache et al., 2002).

The catalytic activity of supported cobalt catalyst also depends on cobalt reducibility. To enhance the reducibility of cobalt, which is well dispersed on a support, a small amount of noble metal such as Ru, Pt, Pd, Ir or Re can be added (Zhang et al., 2010; Khodakov, Chu, and Fongarl, 2007; Ma et al., 2012; Tsubaki, Sun, and Fujimoto., 2001; Xu et al., 2005; Lapidus., 2005). There are several reports about the use of Ru as a promoter for cobalt catalysts in the FTS process to enhance cobalt reducibility and CO conversion (Tsubaki, Sun, and Fujimoto, 2001; Xu et al., 2005). Other promoters including Pd are not extensively investigated for the FTS. Pd as a promoter on cobalt catalyst can act as adsorption sites for H_2 and increase hydrogenation rate in FTS (Ma et al., 2012; Xu et al., 2005). Such improvement could provide crucial paraffin products and prevent the formation of hard waxes, which are inactive carbons, a cause of catalyst deactivation (Morales and Weckhuysen, 2006; Guzzi et al., 2001). Guzzi et al. (2001) showed that an addition of Pd to Co/SiO_2 resulted in an increase in the relative fraction of alkanes during FTS. This effect was attributed to a higher concentration of surface hydrogen on the Pd promoter. The aim

of this work was to compare physicochemical properties of Co/SiO₂ prepared by incipient wetness impregnation (IP) with absolute ethanol and precipitation with reverse micelle technique (RM) and their changes after the addition of Pd. The catalyst properties were investigated by various characterization techniques including X-ray diffraction (XRD), H₂-temperature programmed reduction (H₂-TPR), diffuse reflectance ultraviolet-visible spectroscopy (DR-UV-vis) and X-ray absorption spectroscopy (XAS, including X-ray absorption near edge structure (XANES) and extended X-ray absorption fine structure (EXAFS) spectroscopy). Finally, the influence of catalyst preparation method and Pd promoter on FTS was investigated.

3.2 Experimental

3.2.1 Catalyst preparation

Silica (SiO₂) with 0.5 g/cm³ of pore volume and 2-4 μm of pore diameter (K253, Chemiewerk Bad Köstritz GmbH) was used as a support for all catalysts. The catalysts were prepared by IP and precipitation with RM technique by procedures from the literatures (Zhang et al., 2007; Mabaso, 2005).

In the IP method (Zhang et al., 2007), cobalt nitrate hexahydrate (Co(NO₃)₂•6H₂O, 99%, Riedel-de Häen) was dissolved ethanol and dropped on the support. The wetness solution volume of the SiO₂ was 2.1 cm³/g; the concentration of cobalt precursor was for the 10 wt% cobalt loading. The mixture was dried at room temperature overnight, at 100 °C for 16 h and calcined at 300 °C for 3 h. The obtained catalyst was named 10Co-IP.

In precipitation with RM technique (Mabaso, 2005), 40 g of Berol 050 (pentaethylene glycol dodecylether, AkzoNobel) as a surfactant was mixed with 250 g

of *n*-hexane (AR grade, Fischer-Scientific UK Limited) in each of two 1-L beaker, equilibrated for 24 h at room temperature and filtered. An aqueous solution containing 1.756 g of cobalt nitrate in 10.910 g of water was added to the first beaker and 1.632 g of ammonium hydroxide (NH₄OH, 25% NH₃, BI-Laboredarfslager) as a precipitating agent in 10.368 g of water was added to the second beaker; microemulsion was formed in both beakers. The total amount of oil phase and the salt concentration were kept constant throughout all conducted experiments. A 4:1 molar ratio of [NH₄OH]:[Co²⁺] was used to ensure that the precipitation of the 0.5 M cobalt nitrate solution was achieved. The two microemulsions were then mixed in a 2-L glass beaker using an overhead stirrer with a constant speed of 350 rpm for 3 h to facilitate collision between droplets of cobalt nitrate and precipitating agent to produce precipitates. The precipitates remained confined inside the microemulsion droplets until they were separated from the liquid phase by flocculating with acetone. Then, SiO₂ was added into the beaker and stirred for 10 min. Then, the mixture was washed with acetone several times to remove the surfactant, dried at room temperature overnight and at 100 °C for 24 h, and finally calcined at 300 °C for 3 h. The obtained catalyst was named 10Co-RM.

To prepare bimetallic Pd-Co catalysts, 10Co-IP and 10Co-RM were impregnated with a solution of PdCl₂ to provide 0.2 and 1.0 wt% Pd, dried at room temperature overnight, at 100 °C for 16 h and calcined at 300 °C for 3 h. The Pd-Co/SiO₂ catalysts with 0.2 and 1.0 wt% Pd were named 0.2Pd-10Co-IP, 1Pd-10Co-IP, 0.2Pd-10Co-RM and 1Pd-10Co-RM, respectively.

3.2.2 Catalyst characterization

Phases of metal in the catalysts were studied by powder X-ray diffraction (XRD, Bruker AXS D5005) with nickel filtered Cu K_{α} radiation at room temperature in the 2θ range from 25° to 80° with 1 s/step. The phases of cobalt and palladium compounds were assigned according to the database compiled by the Joint Committee on Powder Diffraction Standards (JCPDS). Co_3O_4 crystallite diameters were calculated by Scherrer equation (equation 3.1) using the most intense Co_3O_4 peak at $2\theta = 36.9^{\circ}$:

$$d = \left(\frac{0.89\lambda}{B\cos\theta} \right) \quad \dots(3.1)$$

Where d is the mean crystallite diameter, λ is the X-ray wavelength (1.54056 \AA), and B is the full width at half maximum (FWHM) of the Co_3O_4 diffraction peak (Xu et al., 2005). The relative molar volumes of metallic cobalt were obtained according to the size of Co_3O_4 using equation 3.2 (Xu et al., 2005):

$$d(\text{Co}^0) = 0.75 \cdot d(\text{Co}_3\text{O}_4) \quad \dots(3.2)$$

Then, the cobalt metal dispersion (D) was calculated from equation 3.3 where d is the average cobalt metal particle size in nm, assuming uniform spherical metal particles with site density of 14.6 atom/nm^2 (Xu et al., 2005):

$$D = 96/d \quad \dots(3.3)$$

H_2 -TPR was used to investigate the reduction behavior of the catalysts. A 0.3 g of calcined catalyst was packed in a quartz U-tube reactor, heated to $150 \text{ }^{\circ}\text{C}$ for 1 h under a flow of Ar ($50 \text{ cm}^3/\text{min}$) and cooled to $50 \text{ }^{\circ}\text{C}$ under Ar flow. Then H_2 was introduced to the flow to give 5 vol% H_2 with the total flow rate maintained at $50 \text{ cm}^3/\text{min}$. Then the temperature was raised to $900 \text{ }^{\circ}\text{C}$ with a heating rate of $10 \text{ }^{\circ}\text{C}/\text{min}$.

Amount of H₂ (before and after passing through the catalyst) was detected on-line by a TCD detector. The TPR profile was plotted between TCD signals versus temperature. After reduction, the catalysts were cooled to 50 °C in Ar flow and immediately passivated in molten wax under Ar atmosphere for further characterization (Jacobs et al., 2007).

Forms and local environment of cobalt and palladium after calcination and reduction were studied by DR-UV-Vis technique on a UV-Vis spectrophotometer (Shimadzu UV-2456) at room temperature against BaSO₄ reference in reflectance mode with measuring range of 190 - 800 nm. The spectra were plotted according to the Kubelka-Munk equation (Kukovecz et al., 2001; Morales, Mora and Pal, 2007).

Additional information of the forms and local environment of cobalt after calcination and reduction were studied by XAS at Beamline 8 of the Synchrotron Light Research Institute, Thailand with measurement procedure described in the literature (Klysubun et al., 2007). The XANES and EXAFS spectra of Co K-edge were recorded at room temperature in transmission mode. Either calcined or passivated sample powder was pressed in a frame covered by polyimide tape and mounted onto a sample holder. The photon energy was calibrated by a Co foil at 7709 ± 0.3 eV. Composition of each cobalt form was estimated by Linear Combination Fit (LCF) of XANES spectra in Athena program as described in the literature (Khemthong et al., 2010). The LCF was performed on normalized spectra with energy ranging from -20.00 to 30.00 eV from the edge energy.

EXAFS analysis was performed on calcined and reduced 10Co-IP and 10Co-RM as well as on cobalt standards for comparison. Data processing was done in

Athena program with a standard procedure to convert the absorption coefficient (μ) to EXAFS equation as a function of distance (R) space, ($\chi(R)$).

3.2.3 Catalytic testing for FTS

The catalytic testing for FTS was carried out in a U-tube fixed-bed reactor made from stainless steel (O.D., 0.635 mm and I.D., 0.5 mm). A 1 g of the calcined catalyst, sieved to the range of 0.2-0.35 mm size was packed between quartz wool in the tube center, activated by H₂ (99.998%, Air Liquide, Germany) at a flow rate of 60 cm³/min from room temperature to 100 °C (with a heating rate of 1 °C/min) and held for 1 h. Then the temperature was raised to 350 °C (heating rate 1 °C/min), held for 12 h, cooled down to the reaction temperature (230 °C) under H₂ (flow rate, 32 cm³/min) and held for 30 min. After that, a flow of N₂ (99.998%, Air Liquide, Germany) was slowly introduced and the pressure was adjusted to 5 bar by a needle valve. Then, the flow of H₂ was decreased and a flow of CO (99.95%, Messer Griesheim, Germany) was added. The final gas mixture had N₂/H₂/CO volume ratio of 8/22/11 in which the H₂/CO ratio was 2/1. The first injection to a gas chromatograph (GC) was made when the flow rate became constant (about 1 h after the pressure adjustment). The FTS was tested at 230 °C and 5 bar for 480 min. During the reaction, H₂, Ar (from a reference gas), CO, CH₄ and CO₂ were analyzed by using a GC (Hewlett Packard 5890) equipped with a TCD and C₂–C₄ gaseous products were analyzed by another GC (Agilent Technologies 6890N) equipped with a flame ionization detector (FID). Cyclohexane (0.13 mol% in Ar) as a reference gas was mixed with the product stream just before the GC analysis. In addition, the liquid products (C₅–C₉) were measured by using another GC (Agilent Technologies 6890N) equipped with a mass selective detector (MSD, Hewlett Packard 5973).

The following equations (Ma et al., 2012) were used to obtain some information resulting from catalytic studies:

$$\% \text{ CO conversion} = \left(\frac{\dot{n}_{\text{CO}_{\text{in}}} - \dot{n}_{\text{CO}_{\text{out}}}}{\dot{n}_{\text{CO}_{\text{in}}}} \right) \times 100 \quad \text{.....(3.4)}$$

$$\% \text{ H}_2 \text{ conversion} = \left(\frac{\dot{n}_{\text{H}_2 \text{ in}} - \dot{n}_{\text{H}_2 \text{ out}}}{\dot{n}_{\text{H}_2 \text{ in}}} \right) \times 100 \quad \text{.....(3.5)}$$

$$\% \text{ CH}_4 \text{ selectivity} = \left(\frac{\dot{n}_{\text{CH}_4 \text{ in}}}{\dot{n}_{\text{CO}_{\text{in}}} - \dot{n}_{\text{CO}_{\text{out}}}} \right) \times 100 \quad \text{.....(3.6)}$$

Mole fraction of olefin content

$$= \left(\frac{\dot{n} \text{ of olefin for carbon number } i}{\dot{n} \text{ of total olefin and paraffin for } C_i} \right) \quad \text{.....(3.7)}$$

Mole fraction of *n*-paraffin in range of C₂-C₄

$$= \left(\frac{\dot{n} \text{ of total paraffin from } C_2-C_4}{\dot{n} \text{ of total of paraffin and olefin from } C_2-C_9} \right) \quad \text{.....(3.8)}$$

Mole fraction of *n*-paraffin in range of C₅-C₉

$$= \left(\frac{\dot{n} \text{ of total paraffin from } C_5-C_9}{\dot{n} \text{ of total of paraffin and olefin from } C_2-C_9} \right) \quad \text{.....(3.9)}$$

Mole ratio of methyl branched paraffin

$$= \left(\frac{\dot{n} \text{ of total methyl branched paraffin for } C_i}{\dot{n} \text{ of } n\text{-paraffin for } C_i} \right) \quad \text{.....(3.10)}$$

Mole fraction of alcohol content

$$= \left(\frac{\dot{n} \text{ of alcohol for } C_i}{\dot{n} \text{ of alcohol for } C_i + \dot{n} \text{ of linear hydrocarbon for } C_i} \right) \quad \text{.....(3.11)}$$

where \dot{n} = molar flow rate (mole/min), C_{*i*} = hydrocarbon with *i* carbon atoms

Chain growth probability (α) obtained from ASF plot in the C₃-C₉ hydrocarbon range;

$$\log (W_n/n) = (n) \log \alpha + c \quad \text{.....(3.12)}$$

3.3 Results and discussion

3.3.1 Catalyst characterization by XRD

Figure 3.1A shows XRD patterns of calcined catalysts including monometallic (10Co-IP and 10Co-RM) and bimetallic (0.2Pd-10Co-IP, 1Pd-10Co-IP, 0.2Pd-10Co-RM, and 1Pd-10Co-RM). The XRD patterns of calcined 10Co-IP and 10Co-RM catalysts were similar to that of Co_3O_4 with peaks at $2\theta = 31.3, 36.9, 45.1, 59.4$ and 65.4° which are characteristic of Co_3O_4 spinel (Panpranot et al., 2003). The peaks from 10Co-IP had higher intensity and were sharper than those from 10Co-RM suggesting the higher crystallinity and larger size of Co_3O_4 crystals. After addition of 0.2 and 1 wt% Pd, XRD patterns of bimetallic catalysts were essentially similar to those of the monometallic ones indicating similar nature of Co_3O_4 particle in the IP and RM series. Re-distribution of Co_3O_4 did not take place after the Pd addition. In the bimetallic catalysts, a small peak of PdO was observed at $2\theta = 33.8^\circ$ (Panpranot et al., 2004; Wattoo et al., 2008; Zhang et al., 2005) and a peak of PdCoO_2 was observed at 38.1° [JCPDS] in the pattern of 1Pd-10Co-IP.

Figure 3.1 B shows XRD pattern of mono- and bimetallic cobalt catalysts after reduction. Both series illustrated peak of metallic cobalt with hexagonal close packed (hcp) at 41.4° and 42.7° , face centered cubic (fcc) structure at 44.8° and 51.5° (Ducreux et al., 2009). The dominant metallic cobalt in the reduced 10Co-IP was hcp but less extent was observed in the reduced 10Co-RM. This result was consistent with the report of Fischer, Steen and Claeys (2011) that fcc metallic crystal phase was mainly observed after reduction when the particle of Co_3O_4 supported on Al_2O_3 with 10 wt% Co loading was less than 4 nm in size. In the bimetallic catalysts, the

characteristic diffraction peak of metallic palladium (Pd^0) was not observed in all catalysts due to low Pd loading (Wang et al., 2008). In addition, low-intensity peaks corresponding to oxides of cobalt were observed in some catalysts. Part of the passivated catalyst could expose to air and got re-oxidized during the sample preparation for XRD analysis.

Particle sizes of Co_3O_4 , Co^0 and % dispersion of the catalysts calculated from equation 3.1-3.3 are shown in Table 3.1. The particle size of Co_3O_4 and corresponding Co^0 of the catalysts in RM series were smaller than those from IP. The results confirmed the control of particle size by the preparation method. Addition of 0.2 and 1.0 wt% of Pd did not change the particle sizes of Co_3O_4 in calcined catalysts and the corresponding Co^0 . In the other words, re-distribution of cobalt species did not occur.

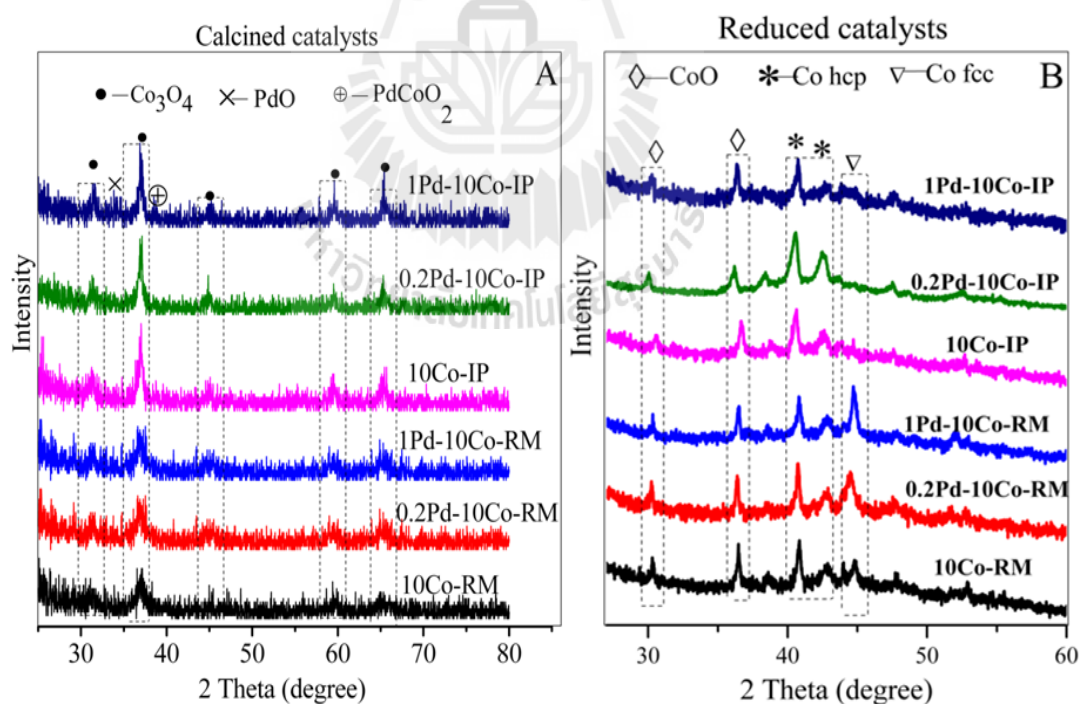


Figure 3.1 The XRD peaks of calcined (A) and reduced (B) catalysts.

Table 3.1 The particle diameters and dispersions of different catalysts.

Catalysts	$d(\text{Co}_3\text{O}_4)$ nm		Dispersion (%)
	Calcined catalysts	Reduced catalysts	
10Co-IP	15.2	11.4	8.4
0.2Pd-10Co-IP	13.6	10.2	9.4
1Pd-10Co-IP	15.5	11.6	8.2
10Co-RM	7.1	5.4	17.8
0.2Pd-10Co-RM	6.8	5.1	18.8
1Pd-10Co-RM	7.3	5.5	17.5

3.3.2 Catalyst characterization by TPR

Figure 3.2 shows TPR profiles of mono- and bimetallic Co catalysts from the IP and RM series. In figure 3.2A, the reduction profiles of the 10Co-IP consist of four peaks at 330, 381, 440 and 676 °C corresponding to the reduction of Co_3O_4 to CoO, smaller particle size of Co_3O_4 to CoO, CoO to Co^0 and cobalt hydrosilicate to Co^0 , respectively (Tsubaki, Sun and Fujimoto, 2001; Haddad and Goodwin, 1995; Steen et al., 1996). The last peak indicated a strong interaction between cobalt and the silica support (Xiong et al., 2009; Stonkus et al., 2009; Lin et al., 2003). The peaks from the TPR profile of 10Co-RM can be observed at 280, 476 and 847 °C corresponding to the reduction of Co_3O_4 to CoO, at CoO to Co^0 (Tsubaki, Sun and Fujimoto, 2001; Okamoto et al., 1990) and cobalt silicate to Co^0 (Stonkus et al., 2009; Lin et al., 2003). In 10Co-RM, Co_3O_4 showed an improved dispersion which could lead to an enhanced exposure to hydrogen and a faster reduction to CoO. However, smaller particles have

stronger interaction with the support which made the reduction of CoO to metallic Co more difficult. Furthermore, the strong metal-support interaction in 10Co-RM resulted in the formation of cobalt silicate which could be reduced at higher temperature than in the case of 10Co-IP (i.e., 847 vs. 676 °C). After the addition of Pd to both 10Co-IP and 10Co-RM, the peaks for the reduction of Co_3O_4 to CoO and CoO to Co^0 occurred at lower temperatures and a larger shift was observed with higher Pd loading. It has been known that the palladium cation can be reduced readily at room temperature (Stonkus et al., 2009). The resulting metallic Pd then became adsorption sites for hydrogen which could spill over to reduce the adjacent Co oxides (Jacobs et al., 2007; Xiong et al., 2009). Part of Pd^{2+} ions could interact with Co_3O_4 to form Pd–O–Co (Xiong et al., 2009). When compared the influence of Pd between the bimetallic IP and RM catalysts, the first reduction peak in RM series can be observed at temperatures lower than that of the IP series. This might be due to a close proximity of Pd particle to the well-dispersed Co_3O_4 . The peak at 350 and 295 °C in 0.2Pd-10Co-RM and 1Pd-10Co-RM, respectively, belong to cobalt species strongly bound to the support which was difficult to reduce.

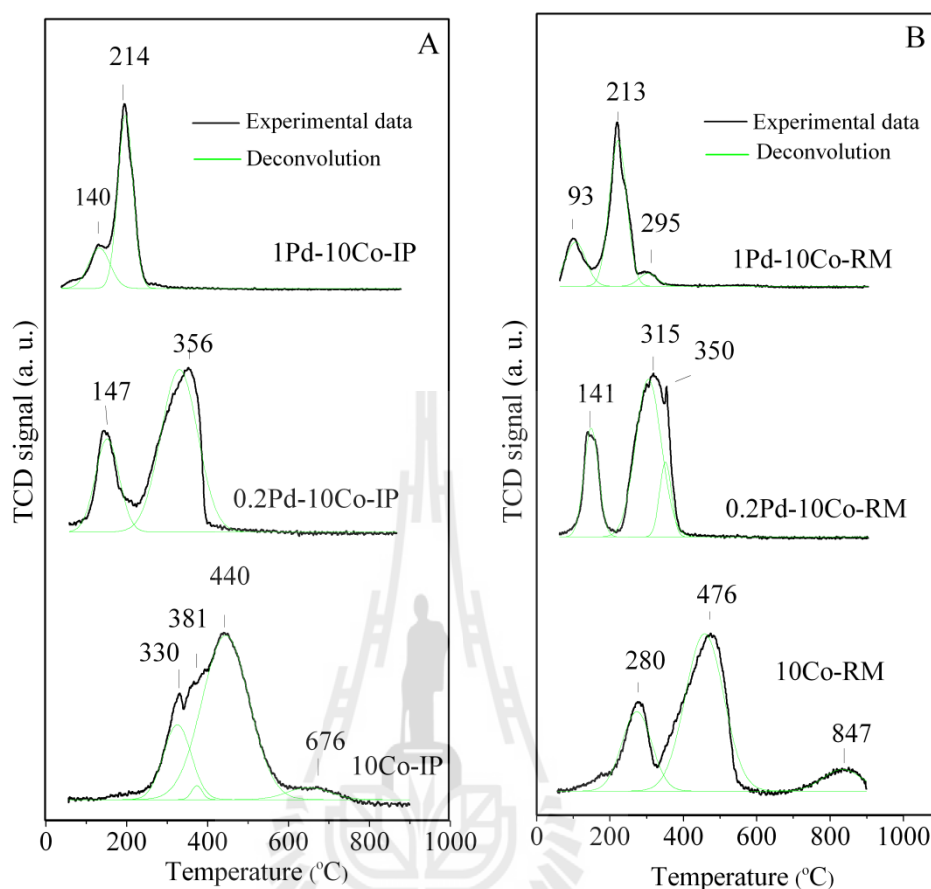


Figure 3.2 TPR profiles of the catalysts in IP series (A) and RM series (B).

3.3.3 Characterization by DR-UV-vis

DR-UV-vis spectra of calcined 10Co-IP and 10Co-RM are shown in Figure 3.3A. Both catalysts showed four bands with different amplitudes. The bands from the spectra of 10Co-IP at 240, 351, 425 and 708 nm are characteristic of Co_3O_4 and are related to ligand-to-metal charge transfer (LMCT, where oxygen atoms were the ligands) and d-d electronic transition associated with Co ions (Prieto et al., 2009). The bands between 200 and 250 nm are attributed to the oxygen to metal charge transfer (Boix, Aspromonte and Miró et al., 2008; Solsona et al., 2008) and the band at

approximately 350 nm of cobalt oxide thin film was attributed to LMCT process of $O^{2-} \rightarrow Co^{2+}$ (Barreca and Massignan, 2001). The absorption band at 415 nm is known from octahedral coordinated Co^{3+} in well-ordered spinel Co_3O_4 species and the band at 715 nm was ascribed to the electronic ligand-field ${}^4A_2(F) \rightarrow {}^4T_1(P)$ transition of Co^{2+} in tetrahedral coordination (Taghavimoghaddam et al., 2012). The Co_3O_4 spinel contained one-third of the Co^{2+} tetrahedral (T_d) site which has d^7 configuration with high-spin state and two-third of the Co^{3+} octahedral (O_h) site which has d^6 configuration with low-spin state (Kim and Park, 2003). The DR-UV-vis spectra of 10Co-RM consist of bands at 225, 350, 401 and 690 nm corresponding to similar transitions in the spinel Co_3O_4 . The shift of bands to lower wavelengths (blue shift) was due to the quantum size effect, namely, smaller crystal size of Co_3O_4 in 10Co-RM (Khodakov, Chu and Fongerl et al., 2007). The existence of spinel Co_3O_4 and smaller crystal size in 10Co-RM suggested by DR-UV-vis was consistent with the XRD result.

Comparison of DR-UV-vis spectra of mono- and bimetallic catalysts in IP and RM series are shown in Figure 3.3B and C, respectively. The four bands observed in the monometallic catalysts were still observed in the bimetallic ones. The band intensities in the bimetallic samples were higher than those in the corresponding monometallic catalyst. This probably related to the overlap with the peaks of transition in PdO or the formation of $CoCl_2$ species formed after impregnation with $PdCl_2$. The existence of $CoCl_2$ species could be further proved by XAS (see Section 3.3.4). An additional peak at 275 nm observed in both series after Pd addition could be assigned to a charge transfer in PdO (Verduraz et al., 2008).

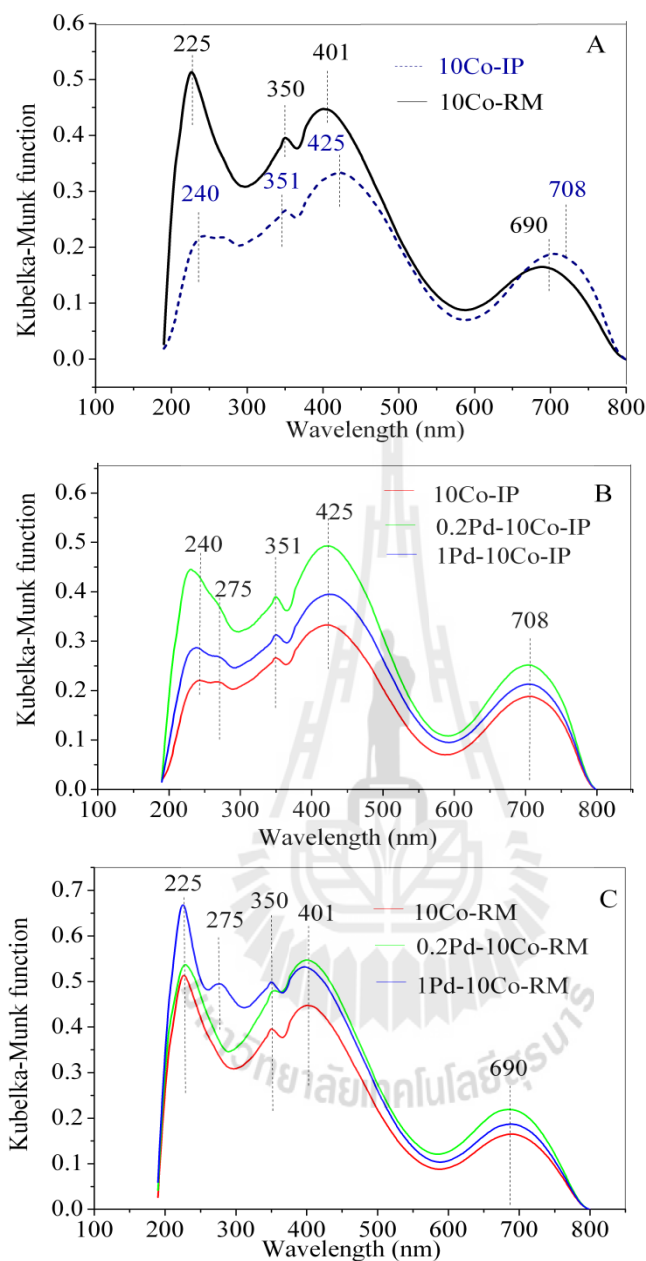


Figure 3.3 The DR-UV-vis spectra of all calcined catalysts.

The spectra from all reduced catalysts in IP and RM series are shown in the Figure 3.4A and B, respectively. The spectra consisted of a broad flat band which covered the range of CoO (400-700 nm) (Janas et al., 2009; Martens et al., 1986).

Thus, it was possible that metallic Co was re-oxidized to CoO during passivation or sample preparation for the UV analysis (Martens et al., 1986). The presence of CoO in the reduced catalysts was also suggested by XANES (see section 3.3.4).

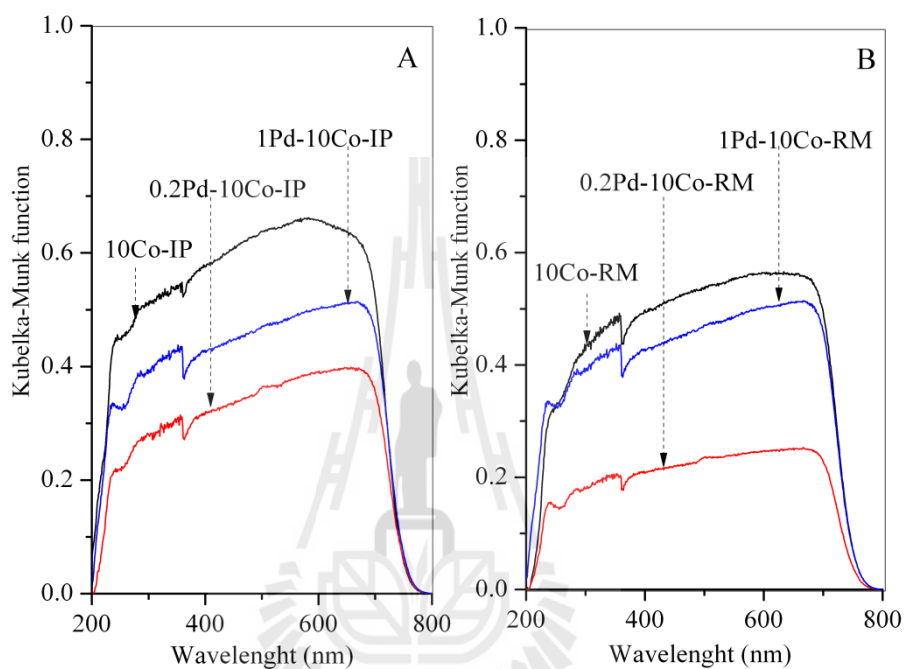


Figure 3.4 The DR-UV-vis spectra of all reduced catalysts.

3.3.4 Catalyst characterization by X-ray absorption

3.3.4.1 Characterization of calcined 10Co-RM and 10Co-IP by XANES and EXAFS

XANES spectra of reference materials including Co foil, CoO, Co₃O₄, Co(NO₃)₂, Co₂SiO₄ and CoCl₂ were acquired for comparison (see Figure 3.5). The XANES spectra of the calcined catalysts compared with Co₃O₄ are shown Figure 3.6A and the spectra of reduced catalysts compared with CoO are shown in Figure 3.6B. Values of pre-edge, K-edge and shift of K-edge from that of the Co foil are

listed in Table 3.2. In general, a shift of the peak position and a change of intensity in XANES spectra of a metal could indicate the change in oxidation state and local environment. The XANES spectra of the calcined 10Co-IP and 10Co-RM (Fig. 3.6A) were similar to that of Co_3O_4 and the edge shifts are nearly the same (Table 3.2). These results indicate that Co_3O_4 was generated in both samples after calcination. Beside the edge position, pre-edge which is a small peak before the rise of the edge (Koningsberger and Prins, 1988) gives information on the structure. The pre-edge is assigned to an electron transition from 1s to 3d orbital which is usually dipole-forbidden but becomes allowed when the metal has tetrahedral coordination (Khemthong et al., 2010). The pre-edge of both samples are similar to that of Co_3O_4 suggesting that Co_3O_4 was the major cobalt form. Another feature to consider is the white line which is the strongest peak from a transition of core electron to continuum. The white line intensity of 10Co-IP was higher than that of 10Co-RM suggesting a larger cluster size of Co_3O_4 . The information from XANES could confirm the existence of Co_3O_4 which contained mixed forms of cobalt, Co^{2+} in tetrahedral and Co^{3+} in octahedral structure, consistent with the results from DR-UV-vis and XRD. Result from LCF of calcined 10Co-IP and 10Co-RM show that the Co_3O_4 is the major component (Table 3.3). Details from the LCF fitting can be found in Figure 3.7. The amount of Co_3O_4 in 10Co-IP was higher than that of 10Co-RM catalyst as the latter had more amount of Co_2SiO_4 , an indication of strong metal-support interaction. These results were in a good agreement with the TPR results.

Figure 3.8A shows Fourier-transformed data of the XAS spectrum in the EXAFS region of the calcined 10Co-IP and 10Co-RM compared to that of the Co_3O_4 . Similarity between the spectra of both calcined samples and that of Co_3O_4 confirms

that Co_3O_4 was the major component. The backscattering amplitudes from higher shells (high R values) of 10Co-IP are stronger than those of 10Co-RM. This result suggests a larger particle size of Co_3O_4 in 10Co-IP, consistent with the other characterization results.

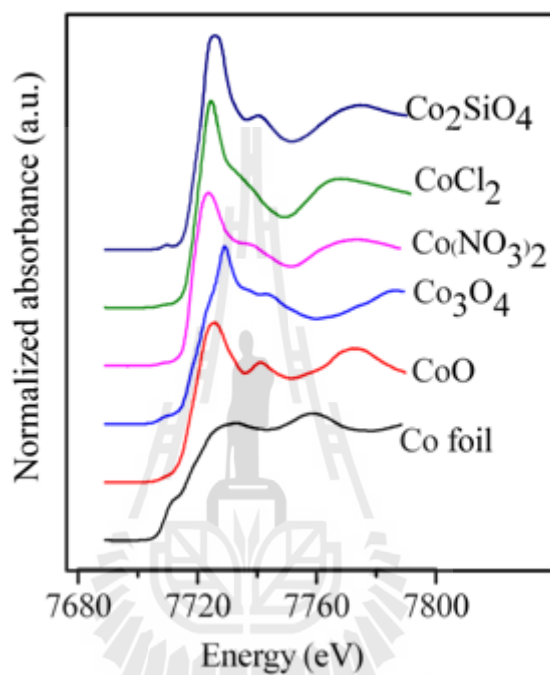


Figure 3.5 XANES spectra of reference material.

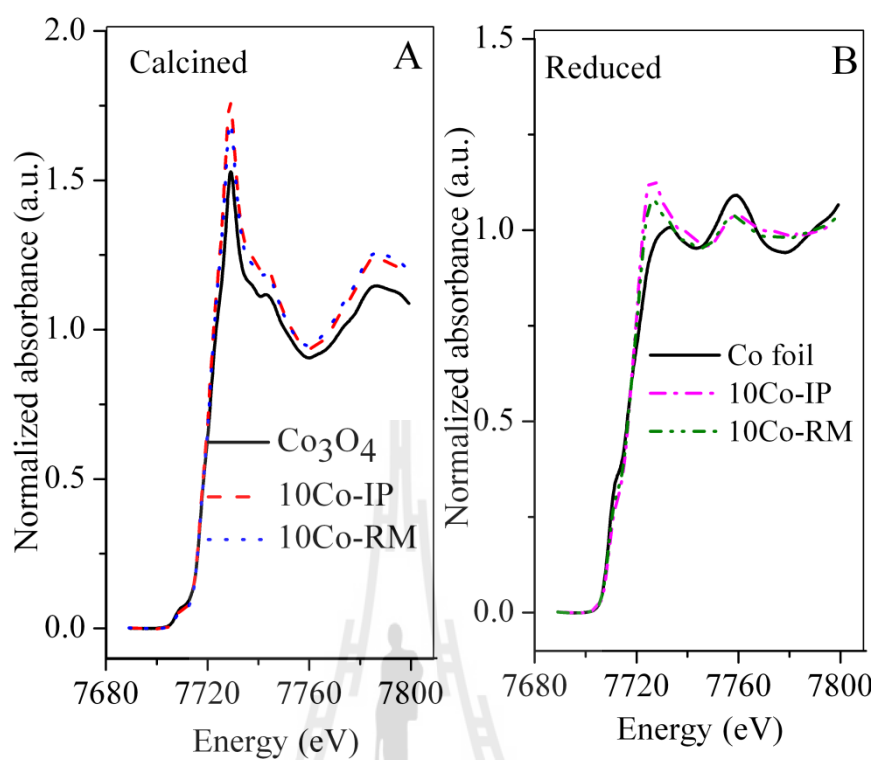


Figure 3.6 The XANES spectrum of Co K-edge of calcined 10Co-IP and 10Co-RM (A) and reduced 10Co-IP and 10Co-RM (B).

Table 3.2 Co K-edge energy position for calcined and reduced catalysts with respect to Co metal foil (7709 keV)^a.

Standards	Pre-edge position	K-edge position	ΔE (eV)
Co foil	-	7709.00	0
CoO	7709.4	7716.2	8.2
Co ₃ O ₄	7709.8	7720.9	11.9
Co ₂ SiO ₄	7710.3	7718.1	9.1
Co(NO ₃) ₂	7710.0	7717.3	8.3
CoCl ₂	7709.5	7717.9	8.9
Calcined catalysts			
10Co-IP	7709.8	7720.5	11.5
0.2Pd-10Co-IP	7709.7	7720.5	11.5
1Pd-10Co-IP	7709.3	7720.3	11.3
10Co-RM	7709.7	7720.5	11.5
0.2Pd-10Co-RM	7709.7	7720.4	11.4
1Pd-10Co-RM	7709.3	7720.2	11.2
Reduced catalysts			
10Co-IP	-	7710.6	1.6
0.2Pd-10Co-IP	-	7709.8	0.8
1Pd-10Co-IP	-	7710.6	1.6
10Co-RM	-	7710.3	1.3
0.2Pd-10Co-RM	-	7709.7	0.7
1Pd-10Co-RM	-	7710.5	1.5

^aThe edge position was obtained by the first derivative process.

Table 3.3 Composition of calcined and reduced catalysts suggested by Linear Combination Fitting (LCF) of XANES spectra.

Catalysts	Components						R-factor $\times 10^{-4}$
	Co ⁰	CoO	Co ₃ O ₄	Co(NO ₃) ₂	CoCl ₂	Co ₂ SiO ₄	
Calcined catalysts							
10Co-IP	0.0	0.0	90.6	0.0	0.0	9.4	9.51
0.2Pd-10Co-IP	0.0	0.0	99.3	0.0	0.7	0.0	9.64
1Pd-10Co-IP	0.0	0.0	90.5	0.0	9.5	0.0	8.5
10Co-RM	0.0	0.0	81.3	0.0	0	18.7	8.43
0.2Pd-10Co-RM	0.0	0.0	89.5	0.0	0.8	9.7	5.71
1Pd-10Co-RM	0.0	0.0	86.7	0.0	8.9	4.4	6.43
Reduced catalysts							
10Co-IP	70.5	22.9	2.1	0.0	0.0	4.5	3.52
0.2Pd-10Co-IP	78.2	17.6	3.6	0.0	0.6	0.0	6.04
1Pd-10Co-IP	69.9	19	3.9	0.0	7.2	0.0	2.42
10Co-RM	75.8	16	1.2	0.0	0.0	7	1.92
0.2Pd-10Co-RM	82.3	10.4	3.4	0.0	0.7	3.2	2.43
1Pd-10Co-RM	72.1	15.1	2.3	0.0	8.2	2.3	3.01

3.3.4.2 Characterization of reduced 10Co-RM and 10Co-IP by XANES and EXAFS

XANES spectra of reduced catalysts are shown in Figure 5B. The K-edge of cobalt in 10Co-RM and 10Co-IP shifted closer to that of the Co foil (Table 3.2). The result suggests that metallic cobalt was generated in both reduced samples. The compositions in reduced 10Co-RM and 10Co-IP from LCF are shown in Table 3.3. Details from the LCF fitting can be found in Figure 3.9. Metallic Co was suggested to be a major species followed by CoO. However, their reducibility should not be compared because the passivated samples might have been partially exposed to air during the sample preparation and some metallic cobalt could be converted back to CoO and Co₃O₄. A small amount of Co₂SiO₄ in both samples could still indicate the strong metal-support interaction.

Figure 3.8B shows EXAFS data of the reduced 10Co-IP and 10Co-RM compared with that of cobalt foil. The Co-Co contribution could be observed in both samples confirming that cobalt oxides were transformed to the metallic form. The magnitude of the Co-Co bond for both catalysts is much smaller than that of Co foil. This could be related to the disorder in the crystal structure of Co induced by the presence of CoO and the decrease the size of Co metallic (Ishida et al., 2013). A higher magnitude of Co-Co bond in 10Co-RM could be associated with a larger amount of reducible fraction suggesting by LCF (Jacobs et al., 2002). Because the LCF results suggested a mixture of cobalt phases, analysis of the EXAFS data was not

further discussed because the result would be the average information of those species.

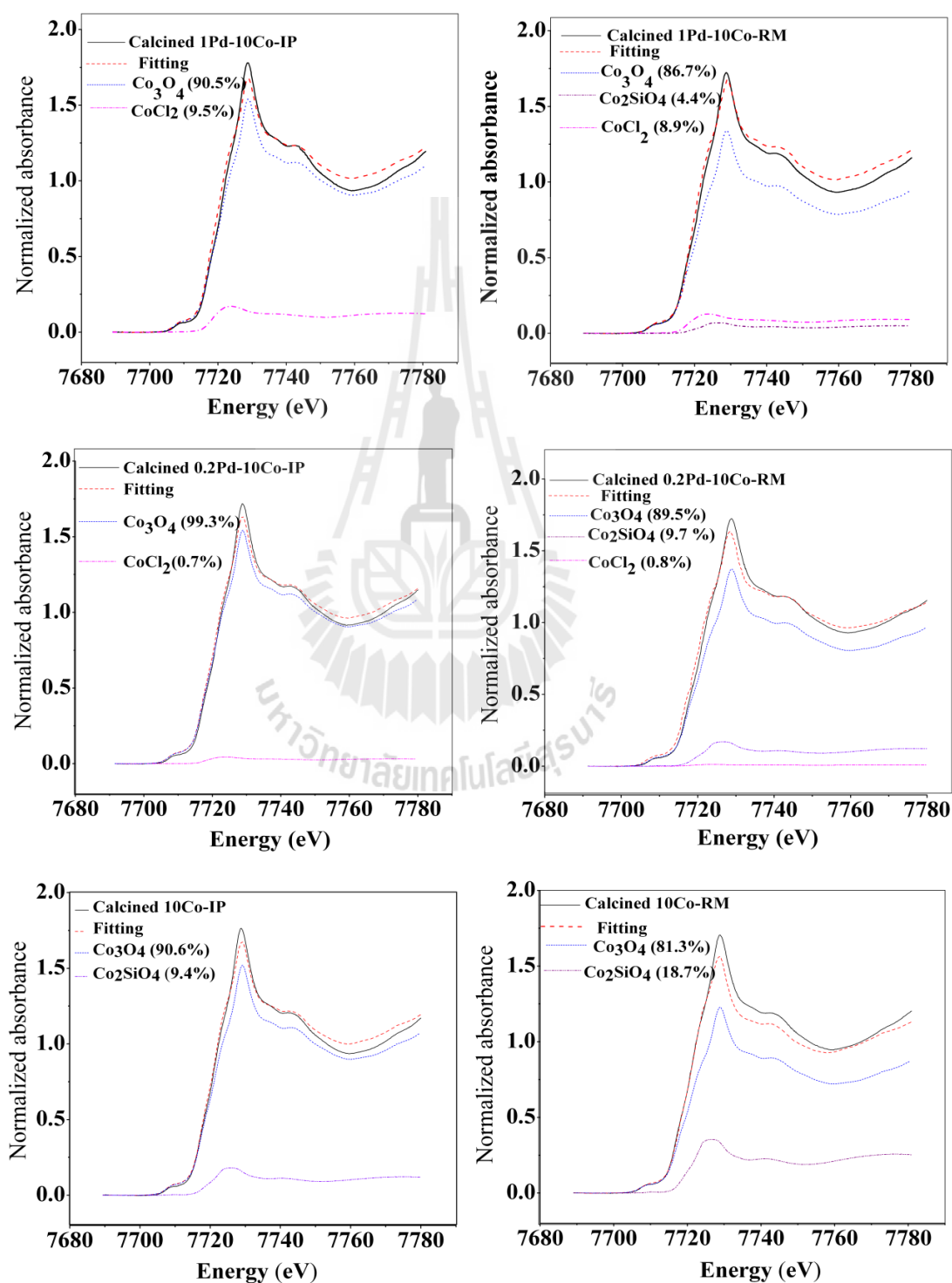


Figure 3.7 Details from the LCF fitting of calcined catalysts.

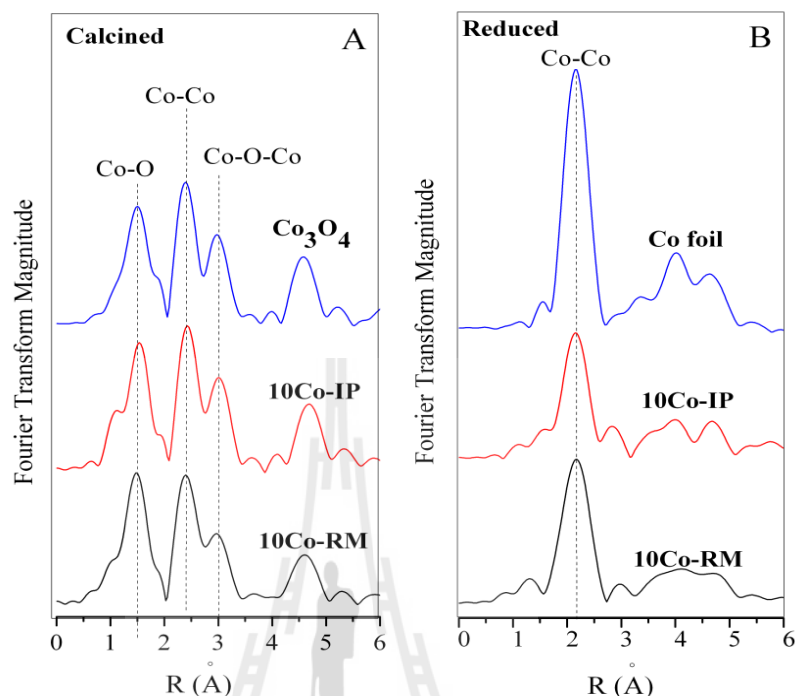


Figure 3.8 The k^3 -weighted magnitude of the Fourier Transform for calcined and reduced 10Co-IP (A), calcined and reduced 10Co-RM (B).

3.3.4.3 Characterization of calcined xPd-10Co-IP and xPd-10Co-RM by XANES

Figure 3.10A and B show the XANES spectra of calcined catalyst including 0.2Pd-10Co-IP, 1Pd-10Co-IP, 0.2Pd-10Co-RM and 1Pd-10Co-RM together with their monometallic counterpart. After the addition of 0.2 or 1.0 wt% Pd, the XANES spectra of both series are still similar to that of Co_3O_4 suggesting that Co_3O_4 was the major component. In addition, a small pre-edge of cobalt in bimetallic catalysts was similar to that of Co_3O_4 standard attributing a similar structure to that of the monometallic catalysts. The result indicates that the addition of Pd by sequential

impregnation did not cause significant change in geometry of Co_3O_4 in both RM and IP series.

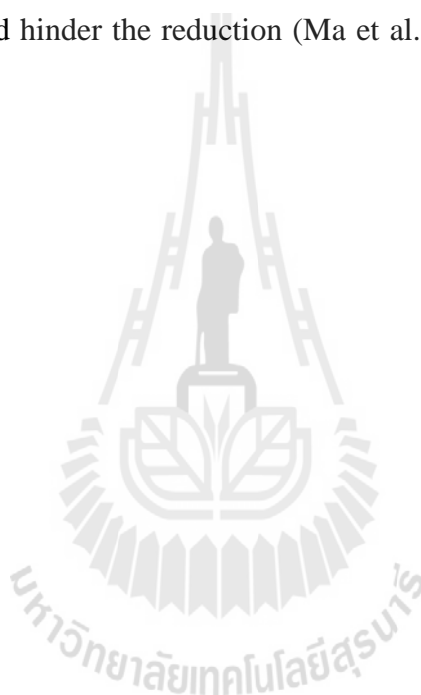
Compositions of cobalt in all catalysts suggested by LCF are summarized in Table 3.3. Details from the LCF fitting can be found in Figure 3.7. Co_3O_4 was still the main component in both series of the calcined bimetallic catalysts. The existence of Co_2SiO_4 in bimetallic catalysts was not suggested in the IP series but still remained in the RM series and decreased with the Pd loading. The decrease of Co_2SiO_4 after the addition of Pd suggests that the interaction between cobalt and support decreased (Xiong et al., 2009). The increase of Co_3O_4 in 0.2Pd-10Co-RM and 0.2Pd-10Co-IP could result from the decrease of Co_2SiO_4 . Moreover, a small amount of CoCl_2 species was observed in both catalysts after calcination. This species could be from the reaction between PdCl_2 and either Co_3O_4 or Co_2SiO_4 as the amount of CoCl_2 increased with the amount of PdCl_2 . The products could be PdCoO_2 , CoCl_2 and CoO as proposed by Hasegawa et al. (2003). The presence of the PdCoO_2 was also confirmed by XRD.

3.3.4.4 Characterization of reduced xPd-10Co-IP and xPd-10Co-RM by

XANES

XANES spectra of reduced bimetallic catalysts in RM and IP series are shown in Figure 10C and D. The Co K-edge positions and shifts from the edge of the Co foil are listed in Table 3.2. The Co K-edge of the reduced bimetallic catalysts is still near to that of metallic cobalt confirming that cobalt species, mainly Co_3O_4 were transformed to metallic form after reduction. The K-edge position of all catalysts are higher than that of the Co foil suggesting that a small amount of oxides were still present. This could be from re-oxidation during the transfer of the passivated sample

to the XANES sample holder. However, the pre-edge was no longer observed in the reduced catalysts. The addition of 0.2 wt% Pd enhanced the reducibility of cobalt in both IP and RM series but less improvement was observed from the addition of 1.0 wt% Pd. The enhancement of reducibility in 0.2Pd-10Co-IP and 0.2Pd-10Co-RM could be a result of H₂ spillover to reduce cobalt oxide (Lapidus, Tsapkina and Krylovo, 2005). However, when the catalyst is loaded with 1.0 wt% Pd, some Pd could cover Co₃O₄ and hinder the reduction (Ma et al., 2012; Lapidus, Tsapkina and Krylovo, 2005).



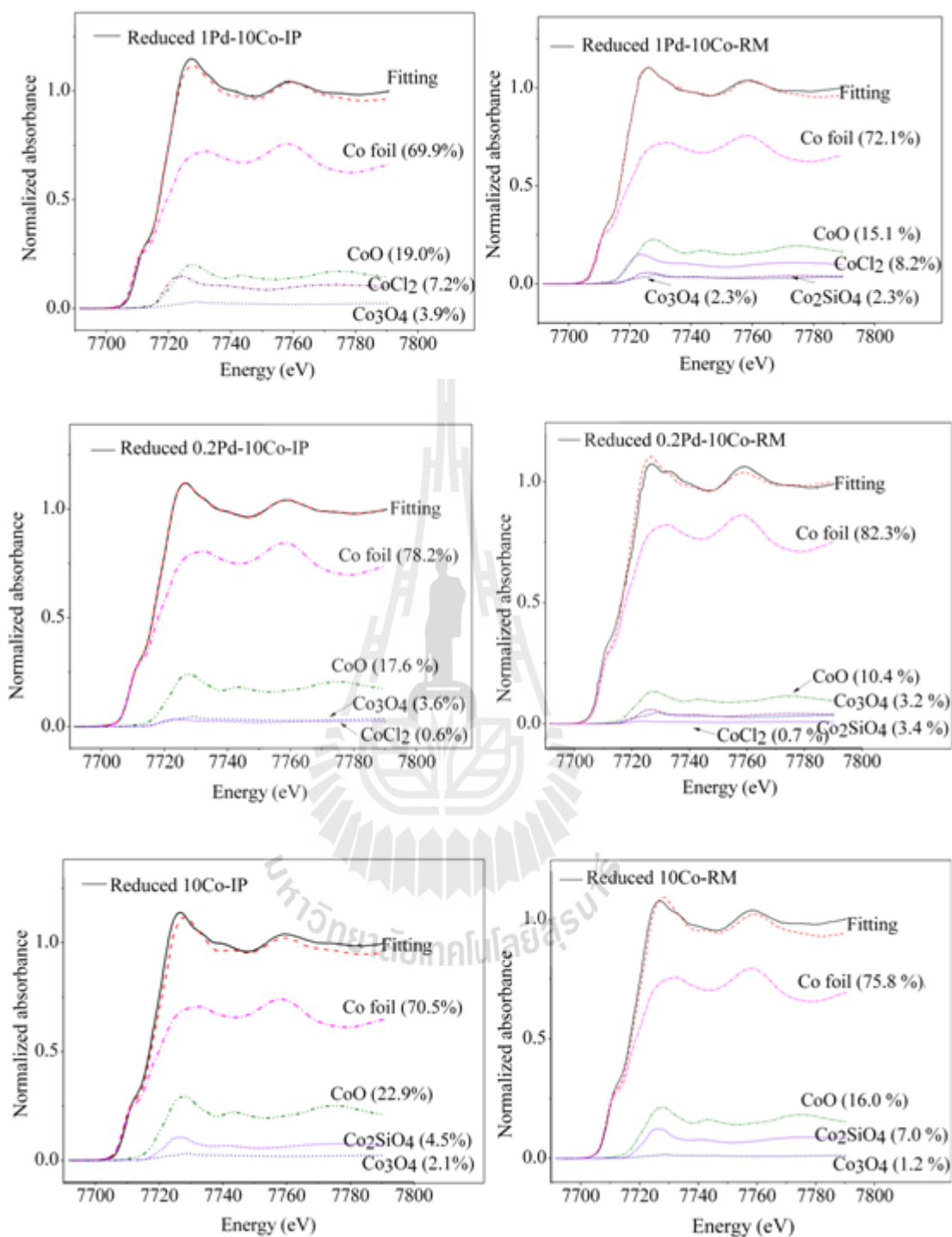


Figure 3.9 Details from the LCF fitting of reduced catalysts.

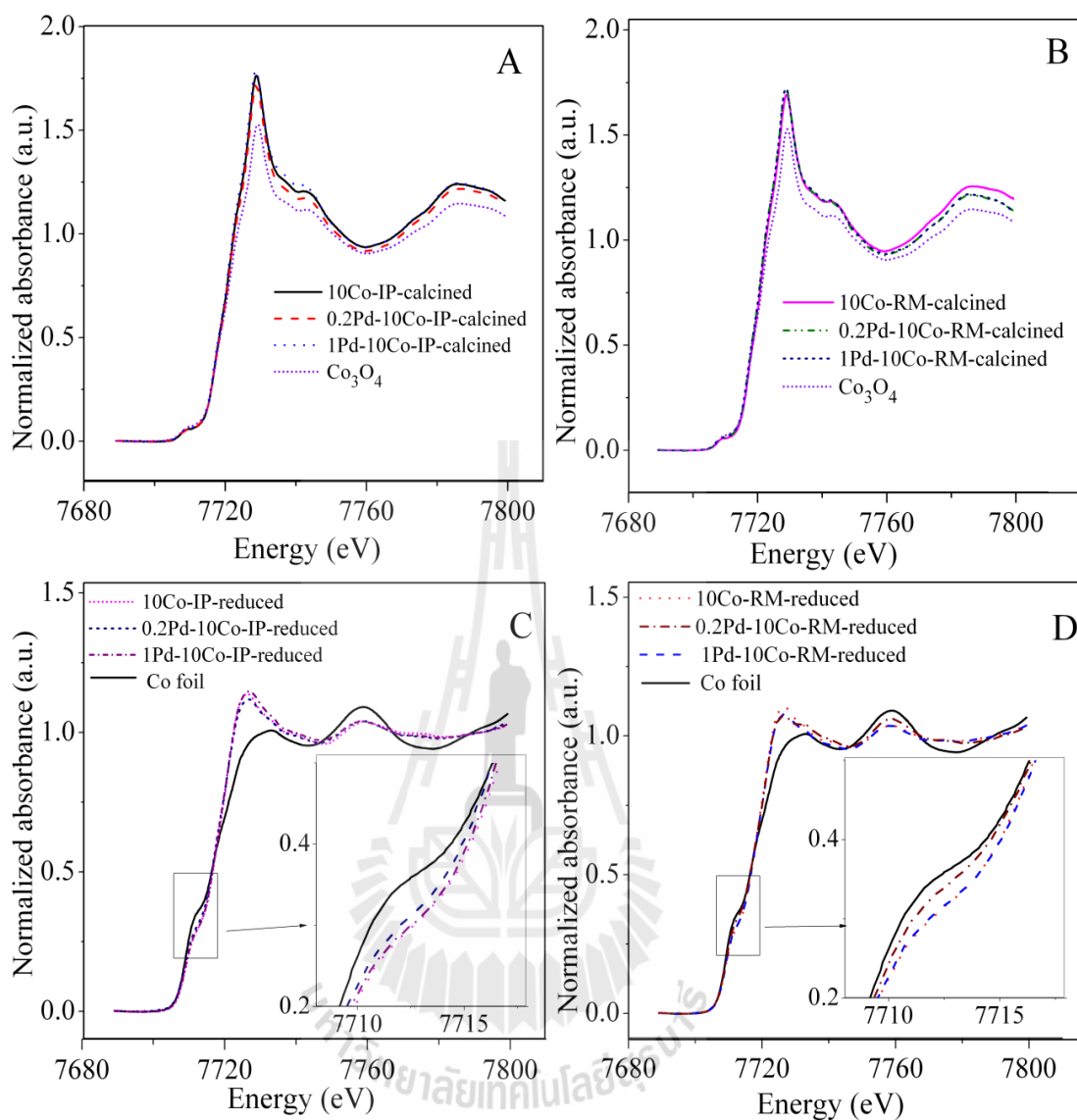


Figure 3.10 The XANES spectrum of catalysts (A and B), calcined IP and RM series; (C and D), reduced IP and RM series.

The results from LCF (Table 3.3 and Figure 3.9) show that the trend of reducibility was similar to that of the edge shift. The addition of 0.2 wt% Pd to 10Co-IP and 10Co-RM resulted in a higher Co^0 content, but not in the same manner as for the addition of 1.0 wt% Pd. As mentioned above, Pd from high PdCl_2 loading could segregate on cobalt oxides and generate CoCl_2 species. The chloride could block the

H₂ adsorption sites on the Co₃O₄ external surface (Panpranot et al., 2003). Khemthong et al. (2009) found that a small amount of CoCl₂ was not reduced at 400 °C after 5 h.

3.3.5 FTS activity

3.3.5.1 Conversion of CO and H₂, selectivity to CH₄ and chain growth probability

The plots for conversions of CO and H₂, selectivity to CH₄ versus time from the IP and RM catalyst series are shown in Figure 3.11. The conversions decrease at the beginning and steady state behavior was nearly reached throughout the experiments. In the IP series, the CO conversions are in the order: 0.2Pd-10Co-IP > 10Co-IP > 1Pd-10Co-IP and the highest H₂ conversion is from 0.2Pd-10Co-IP. In the RM series, CO conversions behave in the order: 10Co-RM ~ 0.2Pd-10Co-RM > 1Pd-10Co-RM and the highest H₂ conversion is from 10Co-RM. In terms of conversions, 0.2Pd-10Co-IP was the best catalyst because it gives the highest conversion of CO and H₂. Moreover, the IP catalysts have lower methane selectivities than the RM catalysts with similar metal content.

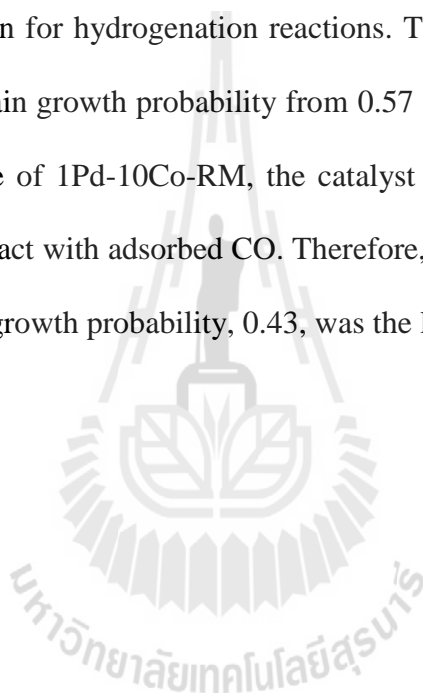
On monometallic catalyst, the 10Co-IP shows a higher CO conversion but lower H₂ conversions than the 10Co-RM. These results could be due to a different particle size, reducibility and the form of metallic phase. Results from XRD and DR-UV-vis indicated that the particle size of cobalt oxide and the corresponding reduced form in 10Co-IP was larger than that in 10Co-RM. From this, the larger particle size is favorable for CO adsorption and leads to the higher CO conversion. The results was in a good agreement with Park et al. (2012) who reported an increase of CO conversion with particle size of cobalt nanoparticles supported on alumina. From this

work, the high CO conversion and low H₂ conversion was consistent with low selectivity to CH₄ and high probability for chain growth. The α value of 10Co-IP was 0.83 implied that the catalyst is suitable for diesel production (Morales and weckhuysen, 2006) and in good agreement with selectivities discussed in section 3.3.5.2. However, such high α value also implies a high tendency to form carbonaceous deposition. Furthermore, the main Co phase in 10Co-IP was hcp which favored adsorption of CO and subsequent dissociation to cobalt carbide (Co₂C) leading to products with long hydrocarbon chain (Ducieux et al., 2009; Van Der Laan et al., 1999).

In 0.2Pd-10Co-IP, the addition of 0.2 wt% Pd enhances the reducibility of cobalt oxides, leading to an increase in adsorption sites and consequently the CO conversion. Pd also serves as adsorption sites for H₂ and resulted in an increase in H₂ conversion. In comparison with 10Co-IP, the enhanced adsorption of hydrogen on Pd sites seemed to be responsible for the increase of the selectivity to CH₄ and the slight decrease of chain growth probability to 0.71. These results also imply a lower probability of carbonaceous deposition.

Excess amount of Pd in 1Pd-10Co-IP results in decreased conversions of both CO and H₂. As mentioned earlier, this amount of Pd did not increase the reducibility of cobalt oxides but it could cover cobalt particles and decrease CO adsorption sites. Although the higher Pd loading increased the adsorption of H₂, the selectivity to CH₄ is increased and the chain growth probability is suppressed ($\alpha = 0.47$). Similar observations were reported by Ma et al. (2012) on Pd-Co/Al₂O₃. In addition, the presence of CoCl₂ or chloride residues could strongly affect the FTS activity because the remaining chloride could block the Co active sites for CO

adsorption (Panpranot et al., 2003). The catalytic performance of 10Co-RM and 0.2Pd-10Co-RM are not much different. They had similar CO conversions but different H₂ conversions and selectivity to CH₄ during the test period. The higher reducibility of cobalt oxides in the bimetallic catalysts could attribute to a decrease in the ratio of conversion of H₂ and CO (X_{H_2}/X_{CO}) (Xiong et al., 2009). The selectivity to CH₄ from 0.2Pd-10Co-RM is higher than that from 10Co-RM because Pd sites provide more hydrogen for hydrogenation reactions. That increase is consistent with the decrease in the chain growth probability from 0.57 of 10Co-RM to 0.53 of 0.2Pd-10Co-RM. In the case of 1Pd-10Co-RM, the catalyst was rich of surface hydrogen which could readily react with adsorbed CO. Therefore, the selectivity to CH₄ was the highest and the chain growth probability, 0.43, was the lowest.



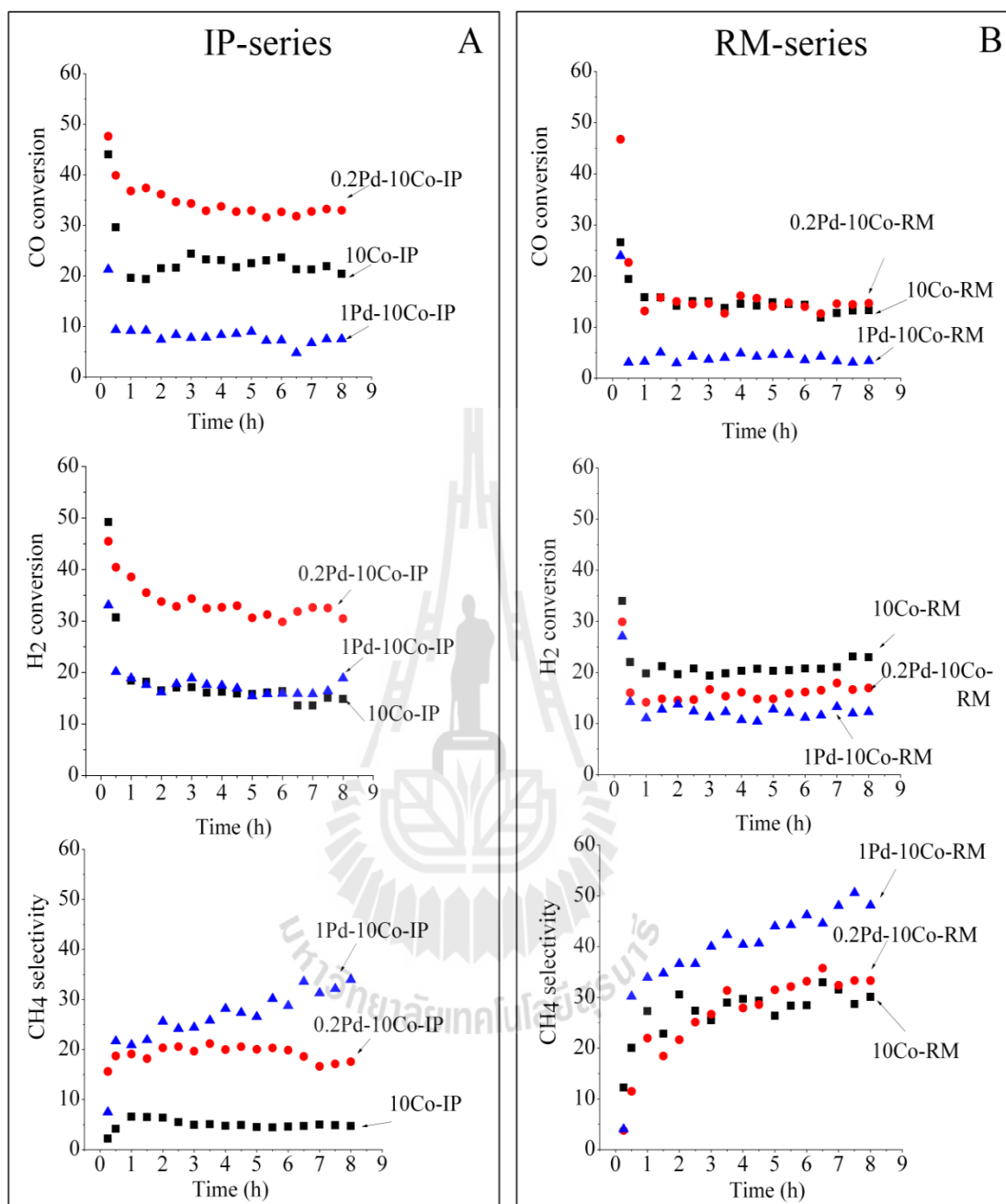


Figure 3.11 CO conversion, H₂ conversion and CH₄ selectivity in IP (A) and RM series (B).

3.3.5.2 FTS selectivity

Figure 3.12 shows selectivity to olefins and *n*-paraffins from FTS by the catalysts prepared with the IP and RM technique. Moreover Figure 3.12A and B show mole fraction of olefins in linear hydrocarbon products from C₂–C₉. The olefin fractions from IP series were much higher than those from RM series and lower tendency of hydrogenation. In this context, the monometallic catalysts had lower ratio of X_{H₂}/X_{CO} and thus higher olefin fractions than those from bimetallic catalysts. In addition, the olefin fraction decreased with higher amounts of Pd due to the increase of available surface hydrogen, consistent with an increase in methane selectivity. A similar observation was reported by Guzzi et al. (2001) using silica supported Pd-Co catalysts prepared by sol/gel method which contained 5 wt% of Pd-Co loading.

Figure 3.12C shows mole fraction of *n*-paraffins in two ranges: C₂–C₄ and C₅–C₉. The first range was greater from all catalysts. However, the fraction of both ranges depended directly on the ratio of X_{H₂}/X_{CO}, namely, the greater fraction of C₂–C₄ were produced on the catalysts with the higher ratio of X_{H₂}/X_{CO}. The high conversion of H₂ indicated high availability of surface hydrogen for hydrogenation to light paraffins (C₂–C₄) (Xu et al., 2005; Park et al., 2012). This explanation is similar to that of the conversions, namely, the adsorption of hydrogen is increasing with the decrease of cobalt particle size and with the increase of Pd loading (Park et al., 2012). The highest fraction of C₅–C₉ was obtained from 0.2Pd-10Co-IP.

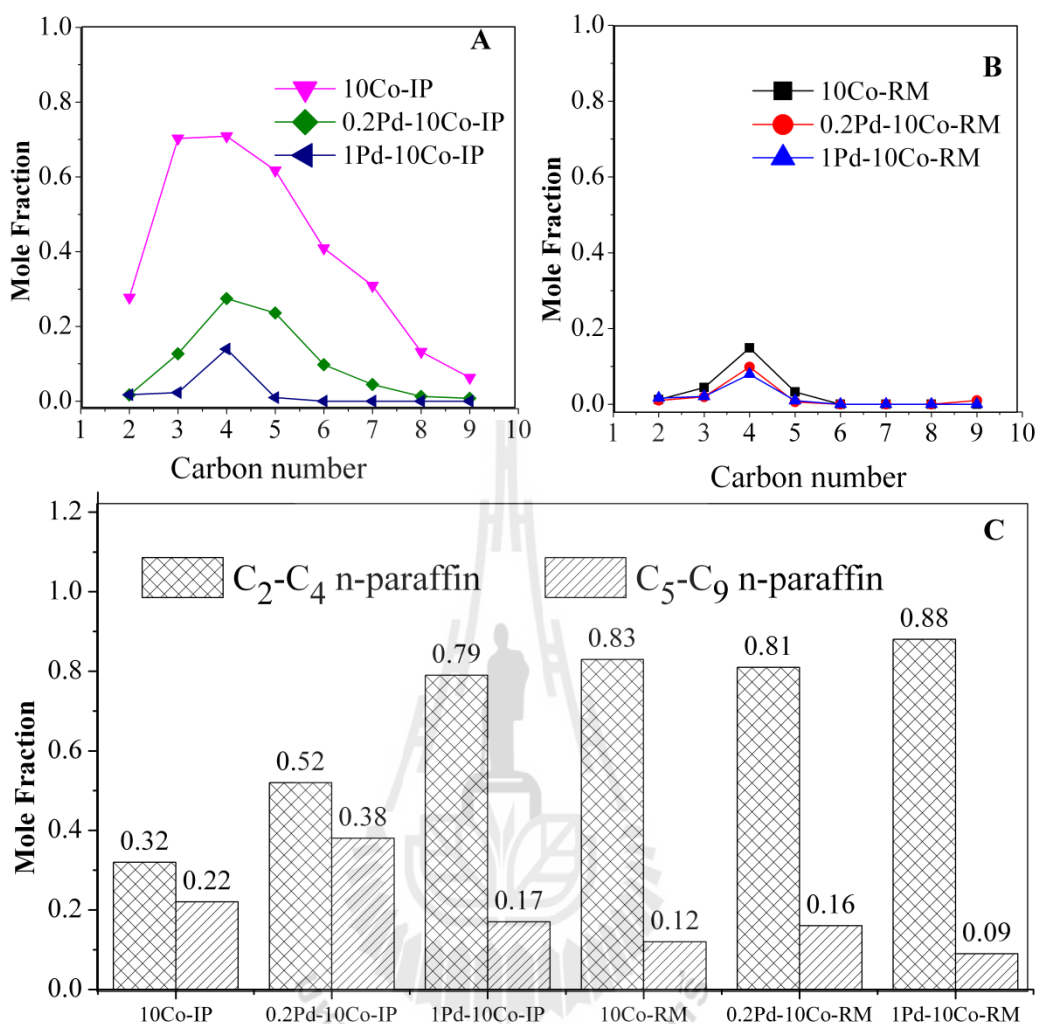


Figure 3.12 Mole fraction of olefins in linear hydrocarbon products from C₂–C₉. (A), IP series; (B), RM series and (C), mole fraction of *n*-paraffins in the range of C₂–C₄ and C₅–C₉ of all catalysts.

Figure 3.13A and B show the mole fraction of alcohols with various carbon numbers. In both series the alcohol content increases with the amount of Pd. Besides serving as adsorption sites for hydrogen for hydrogenation reactions, palladium is known as a catalyst for methanol synthesis (Lebarbier et al., 2012). The results from this work are in good agreement with Ma et al., 2012 who reported that

addition of 0.26 wt% Pd on Co/Al₂O₃ generated more oxygenated products (methanol and ethanol) than that of other promoters (0.5 wt% Pt, 0.48 wt% Re and 0.27 wt% Ru). Berlowitz et al. (1987) also showed that the selectivity of methanol increased with the amount of Pd on SiO₂.

Figure 3.13C shows mole ratio of methyl branched to linear C₆ hydrocarbon products from the studied catalysts. In both series the amount of branched hydrocarbon also increased with the palladium content. With a similar amount of Co and Pd, the RM series show a higher content of methyl branched paraffins than the IP series. This result could be attributed to the addition of Pd and the small particle size of cobalt, which enhance the hydrogenation and isomerization activities (Park et al., 2012). The explanation was consistent with a report by Guzzi et al. (2002) on the increase in hydrogenation and isomerization rates of butadiene with Pd-Co/Al₂O₃. Moreover, additional Pd in the Co catalysts was active for the isomerization of hydrocarbon compounds during the FTS (Ma et al., 2012).

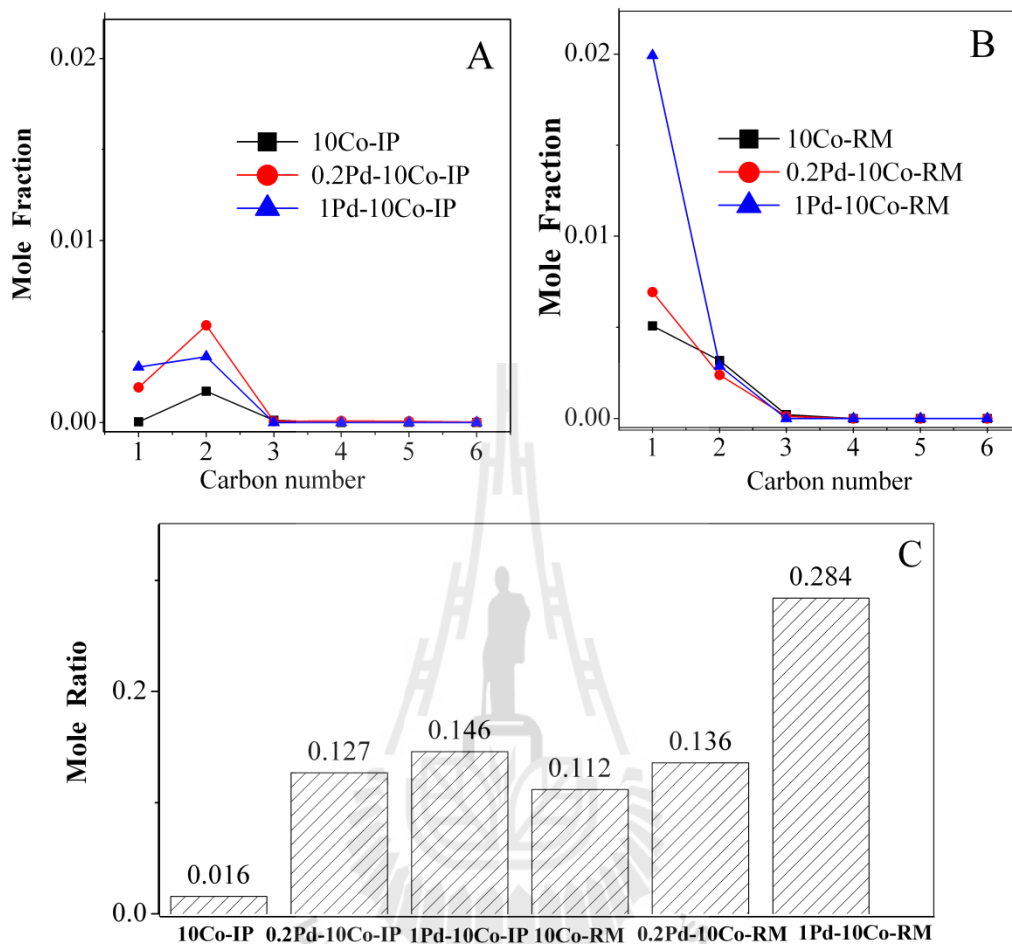


Figure 3.13 Mole fractions of alcohols in all linear hydrocarbons as a function of carbon number, (A), IP series, (B), RM series and (C), mole ratio of methyl branched hydrocarbons to linear C₆ hydrocarbons product as a function of the catalysts.

3.4 Conclusions

SiO₂-support cobalt catalysts (10 wt% Co) were prepared by impregnation (IP) and precipitation using the reverse micelle (RM) method. Co₃O₄ generated after calcination of 10Co-IP have larger particle sizes than that of 10Co-RM. The existence of Co₂SiO₄ species was suggested in both catalysts. After Pd was added to both Co containing catalysts, the structure and particle size of Co₃O₄ did not change; a small amount of CoCl₂ was suggested; and the reducibility of cobalt was improved. The structure of metallic cobalt of catalysts prepared by IP was mainly hcp instead of RM series where a mixed phase of hcp and fcc was found. The FTS activity of the SiO₂-support cobalt catalysts depended on particle size, reducibility, phase structure and Pd addition. With a similar amount of Co and Pd, the IP series show a higher CO conversion than that of catalysts of the RM series and the CO conversion was improved by the addition of 0.2 wt% Pd in both series. The highest CO conversion was obtained from 0.2Pd-10Co-IP. In terms of product selectivity, the IP series produced more olefins than RM series. The addition of Pd enhanced the formation of alkanes including methane, heavy paraffins, methyl-branched paraffin and alcohols. The improvement of Co supported on SiO₂ for FTS accomplished a strategy to produce desired paraffin products in two ranges: the formation of C₂–C₄ paraffins is enhanced in RM series while the C₅–C₉ paraffins (gasoline) are selective using 0.2Pd-10Co-IP.

3.5 References

- Barreca, D. and Massignan, C. (2001). Composition and microstructure of cobalt oxide thin films obtained from a novel cobalt (II) precursor by chemical vapor deposition. **Chemistry of Materials**. 13: 588-593.
- Berlowitz, P. J. and Goodman, D. W. (1987). The activity of Pd (110) for methanol synthesis. **Journal of Catalysis**. 108: 364-368.
- Bezemer, G. L., Bitter, J. H., Kuipers Herman, P. C. E., Oosterbeek, H., Holewijn, J. E., Xu, X., Kapteijn, F., van Dillen, A. J. and de Jong K. P. (2006). Cobalt particle size effects in the Fischer-Tropsch reaction studied with carbon nanofiber supported catalysts. **Journal of American Chemical Society**. 128: 39-56.
- Boix, A. V., Aspromonte, S. G. and Miró, E. E. (2008). Deactivation studies of the NO_x with hydrocarbons on Co-mordenite monolithic catalysts. **Applied Catalysis A: General**. 341: 26-34.
- Diehl, I. and Khodakov, Y. (2009). Promotion of cobalt Fischer-Tropsch catalysts with noble metals: A review. **Oil & Gas Science and Technology - Rev. IFP**. 64: 11-24.
- Ducreux, O., Rebours, B., Lynch, J., Roy-Auberger, M. and Bazin, D. (2009). Microstructure of supported cobalt Fischer-Tropsch catalysts. **Oil & Gas Science and Technology – Rev. IFP**. 64: 49-62.
- Enache, D. I., Rebours, B., Roy-Auberger, M. and Revel, R. J. (2002). *In Situ* XRD study of the influence of thermal treatment on the characteristics and the catalytic properties of cobalt-based Fischer-Tropsch catalysts. **Journal of Catalysis**. 205: 346-353.

- Fische, N., Steen, V. and Claeys, M. (2011). Preparation of supported nano-sized cobalt oxide and fcc cobalt crystallites. **Catalysis Today**. 171: 174-179.
- González, O., Perez, H., Navarro, P., Almedia, L. C., Pacheo, J. G. and Montes, M. (2009). Use of different mesostructured materials based on silica as cobalt supports for the Fischer-Tropsch synthesis. **Catalysis Today**. 143: 140-147
- Guczi, L., Borkó, L., Schay, Z., Bazin, D. and Mizukami, F. (2001). CO hydrogenation and methane activation over Pd-Co/SiO₂ catalysts prepared by sol/gel method. **Catalysis Today**. 65: 51-57.
- Guczi, L., Bazin, D., Kovacs, I., Borko, L., Schay, Z., Lynch, J., Parent, P., Lafon, C., Stefler, G., Koppany, Z. and Sajo, I. (2002). Structure of Pt-Co/Al₂O₃ and Pt-Co/NaY bimetallic catalysts: Characterization by *in situ* EXAFS, TPR, XPS and by activity in Co (carbon monoxide) hydrogenation, **Topics in Catalysis**. 20: 129-139.
- Haddad, G. J. and Goodwin, J. G. (1995). The impact of aqueous impregnation on the properties of prerduced vs precalcined Co/SiO₂. **Journal of Catalysis**. 157: 25-34.
- Hasegawa, M., Tanaka, M., Yagi, T., Takei, H. and Inoue, A. (2003). Compression behavior of the delafossite-type metallic oxide PdCoO₂ below 10 GPa. **Solid State Communications**. 128: 303-307.
- Ishida, T., Yanagihara, T., Liu, X., Ohashi, H., Hamasaki, A., Honma, T., Oji, H., Yokoyama, T. and Tokunaga, M. (2013). Synthesis of higher alcohols by Fischer-Tropsch synthesis over alkali metal-modified cobalt catalysts. **Applied Catalysis A: General**. 458: 145-154.

- Jacobs, G., Patricia, P., Zhang, Y., Das, T., Li, J. and Davis, B. (2002). Fischer-Tropsch synthesis: deactivation of noble metal-promoted Co/Al₂O₃ catalysts. **Applied Catalysis A: General**. 233: 215-226.
- Jacobs, G., Ji, Y., Davis, B. H., Cronauer, D., Kropf, A. J. and Marshall, C. L. (2007). Fischer-Tropsch synthesis: Temperature programmed EXAFS/XANES investigation of the influence of support type, cobalt loading, and noble metal promoter addition to the reduction behavior of cobalt oxide particles. **Applied Catalysis A: General**. 333: 177-191.
- Janas, J., Shishido, T., Che, M. and Dzwigaj, S. (2009). Role of tetrahedral Co(II) sites of CoSiBEA zeolite in the selective catalytic reduction of NO: XRD, UV-vis, XAS and catalysis study. **Applied Catalysis: B-Environmental**. 89: 196-203.
- Kim, K. J. and Park, Y. K. (2003). Optical investigation of charge-transfer transitions in spinel Co₃O₄. **Solid State Communications**. 127: 25-28.
- Klysubun, W., Thanawan, S., Thamasirianunt, P., Radabuttra, S. and Sombunchoo, P. (2007). Determination of chlorine content in chlorinated, vulcanized natural rubber by XANES. **Nuclear Instruments and Methods in Physics Research A**. 582: 242-244.
- Khemthong, P., Klysubun, W., Prayoonpokarach, S. and Wittayakun, J. (2010). Reducibility of cobalt species impregnated on NaY and HY zeolites. **Materials Chemistry and Physics**. 121: 131-137.
- Khodakov, A., Bechara, R. and Griboval-Constant, A. (2003), Fischer-Tropsch synthesis over silica supported cobalt catalysts: mesoporous structure versus cobalt surface density. **Applied Catalysis A: General**. 254: 273-288.

- Koningsberger, D. C. and Prins, R. (1988). **X-ray Absorption Principle, Applications, Techniques of EXAFS, SEXAFS and XANES**, New York.
- Kukovecz, Á., Kónya, Z., MÖnter, D., Reschetilowski, W. and Kiricsi, I. (2001). UV-VIS investigation on Co, Fe and Ni incorporated into sol-gel SiO₂-TiO₂ matrices. **Journal of Molecular Structure**. 563: 403-407.
- Lapidus, A. L., Tsapkina, M. V., Krylova, A. Y. and Tonkonogov, B. P. (2005). Bimetallic cobalt catalysts for the synthesis of hydrocarbons from CO and H₂. **Russian Chemical Reviews**. 74: 577-586.
- Lebarbier, V. M., Dagle, R. A. L., Kovarik, A., Jair, L., Adarme, L. D., King, D. and Palo, R. (2012). Synthesis of methanol and dimethyl ether from syngas over Pd/ZnO/Al₂O₃ catalysts. **Catalysis Science & Technology**. 2: 2116-2127.
- Lin, H. K., Chiu, H. C., Tsai, H. C., Chien, S. H. and Wang, C. B. (2003). Synthesis, characterization and catalytic oxidation of carbon monoxide over cobalt oxide. **Catalysis Letters**. 88: 169-174.
- Ma, W., Jacobs, G., Keogh, R., Bukur, D. B. and Davis, B. H. (2012). Fischer-Tropsch synthesis: Effect of Pd, Pt, Re, and Ru noble metal promoters on the activity and selectivity of a 25% Co/Al₂O₃ catalyst. **Applied Catalysis A: General**. 437-438: 1-9.
- Mabaso, E. H. (2005). **Nanosized Iron Crystallites for Fischer-Tropsch Synthesis**. Ph.D. Thesis, University of Cape Town, South Africa.
- Morales, A. E., Mora, E. S. and Pal, U. (2007). Use of diffuse reflectance spectroscopy for optical characterization of un-supported nanostructures. **Revista Mexicana de Físicas**. 53: 18-22.

- Morales, F. and Weckhuysen, B. (2006). Promotion effects in Co-based Fischer-Tropsch catalysis. **The Royal Society of Chemistry**. 19: 1-40.
- Okamoto, Y., Nagata, K., Adachi, T., Imanaka, T., Inamura, K. and Takyu, T. (1990). Preparation and characterization of highly dispersed cobalt oxide and sulfide catalysts supported on SiO₂. **The Journal of Physical Chemistry**. 95: 310-319.
- Panpranot, J., Kaewkun, S., Prasertthadam P. and Goodwin, J. G. (2003). Effect of cobalt precursors on the dispersion of cobalt on MCM-41. **Catalysis Letters**. 91: 95-102.
- Panpranot, J., Pattamakomsan, K., Prasertthadam, P. and Goodwin, J. G. (2004). Impact of the silica support structure on liquid-phase hydrogenation on Pd catalysts. **Industrial & Engineering Chemistry Research**. 43: 6014-6020.
- Park, J. Y., Lee, Y. J., Karandikar, P. R., Jun, K. W., Bae, J. W., Ha, K. S. and Park, H. G. (2012). Fischer-Tropsch catalysts deposited with size-controlled Co₃O₄ nanocrystals Effect of Co particle size on catalytic activity and stability. **Applied Catalysis A: General**. 411-412: 15-23.
- Prieto, G., Martínez, A., Concepción, P. and Moreno-Tost, R. (2009). Cobalt particle size effects in Fischer-Tropsch synthesis: structural and in situ spectroscopic characterisation on reverse micelle-synthesised Co/ITQ-2 model catalysts. **Journal of Catalysis**. 266: 129-164.
- Steen, E. V., Sewell, G. S., Makhothe, R. A., Micklethwaite, C., Manstein, de Lange, H. M. and Connor, C. T. (1996). TPR study on the preparation of impregnated Co/SiO₂ catalysts. **Journal of Catalysis**. 162: 220-229.

- Solsona, B., Davis, T. E., Garcia, T., Vázquez, I., Dejoz, A. and Tayloy, S. H. (2008). Total oxidation of propane using nanocrystalline cobalt oxide and supported cobalt oxide catalysts. **Applied Catalysis B: Environmental**. 84: 176-184.
- Stonkus, V., Edolfa, K., Leite, L. and Sobczak J. W. (2009). Palladium-promoted Co-SiO₂ catalysts for 1,4-butanediol cyclization. **Applied Catalysis A: General**. 362: 147-154.
- Taghavimoghaddam, J., Knowles, G. P. and Chaffee, A. L. (2012). Preparation and characterization of mesoporous silica supported cobalt oxide as a catalyst for the oxidation of cyclohexanol. **Journal of Molecular Catalysis A: Chemical**. 358: 79-88.
- Tsubaki, N., Sun, S. and Fujimoto, K. (2001). Different functions of the noble metals added to cobalt catalysts for Fischer-Tropsch synthesis. **Journal of Catalysis**. 199: 236-246.
- Van Der Laan, G. P. and Beenackers, A. A. C. M. (1999) Kinetics and selectivity of the Fischer-Tropsch synthesis: A Literature review. **Catalysis: Review Science & Engeneer**. 41: 255-318.
- Van, T., Blik, H. F. J. and Prins, R. (1986). Characterization of supported cobalt and cobalt-Rhodium catalysts: I. Temperature-Programmed Reduction (TPR) and oxidation (TPO) of Co-R h/A₁O₃. **Journal of Catalysis**. 97: 200-209.
- Verduraz, F. B., Fiévet, F. Piquemal, J. Y., Brayner, R., Kabouss, K. E. and Soumare, Y. (2008). Nanoparticles of metal and metal oxides: some peculiar synthesis methods, size and shape control, application to catalysts preparation. **Brazilian Journal of Physics**. 39: 134-140.

- Wattoo, M., Mazhar, M., Tufail, M., Tirmizi, S. and Iqbal, J. (2008). X-ray diffraction analysis to study the effect of metal loading and calcinations and reduction temperature for supported palladium catalysts. **Journal of The Chemical Society of Pakistan**. 30: 377-384.
- Wang, S., He, J., Xi, J., Zhu, Y., Xi, Y. and Chen, J. G. (2008). Synthesis of bimetallic systems using replacement reactions. **Applied Surface Science**. 254: 2102-2109.
- Xiong, H., Zhang, Y., Liew, K. and Li, J. (2009). Ruthenium promotion of Co/SBA-15 catalysts with high cobalt loading for Fischer-Tropsch synthesis. **Fuel Processing Technology**. 90: 237-26.
- Xu, D., Li, W., Duan, H., Ge, Q. and Xu, H. (2005). Reaction performance and characterization of Co/Al₂O₃ Fischer-Tropsch catalysts promoted with Pt, Pd and Ru. **Catalysis Letters**. 102: 229-235.
- Zhang, Q., Kang, J. and Wang, Y. (2010). Development of novel catalysts for Fischer-Tropsch synthesis: tuning the product selectivity. **ChemCatChem**. 2: 1030-1050.
- Zhang, Q., Li, X., Asami, K., Asasoka, K. and Fujimoto, K. (2005). Direct synthesis of LPG fuel from syngas with the hybrid catalyst based on modified Pd/SiO₂ and zeolite. **Catalysis Today**. 104: 30-36.
- Zhang, Y., Liu, Y., Yang, G., Sun, S. and Tsubaki, N. (2007). Effects of impregnation solvent on Co/SiO₂ catalyst for Fischer-Tropsch synthesis: A highly active and stable catalyst with bimodalsized cobalt particles. **Applied Catalysis A: General**. 321: 79-85.

CHAPTER IV

EFFECT OF SUPPORT MORPHOLOGY AND Pd PROMOTER ON Co/SBA-15 FOR FISCHER-TROPSCH SYNTHESIS

Abstract

An influence of support morphology and Pd promoter on physicochemical properties and catalytic performance of Co/SBA-15 in Fischer-Tropsch Synthesis (FTS) was investigated. SBA-15(M) from a hydrothermal synthesis with decane addition had smaller particle size, larger pore size and shorter cavity length which enhanced the dispersion of cobalt oxides, eased diffusion of reactants and improved the FTS performance. 10Co/SBA-15(M) provided the highest and most steady conversions of CO and H₂ with the highest yield of C₅–C₉ products. The addition of Pd enhanced the reduction of cobalt oxides but produced more methane and light paraffins.

4.1 Introduction

Fischer-Tropsch Synthesis (FTS) is a reaction of CO and H₂ to produce fuels (Zhang, Kang and Wang, 2010). The reaction involves adsorption of CO on active sites, hydrogenation to CH_x monomers and polymerization to the products (Zhang, Kang and Wang, 2010). The most superior catalyst for FTS is cobalt (Co).

Its performance could be enhanced by dispersion on a support with uniform pores and high surface area (Ghampson et al., 2010). Particularly, SBA-15 is a promising support because it has uniform hexagonal channels and high thermal stability (González et al., 2009). Reducibility of cobalt oxides to active FTS catalyst could be enhanced by dispersion on SBA-15 (Ghampson et al., 2010).

From our recent study, FTS catalytic performance of 10Co/SiO₂ (with 10 wt. % Co) in terms of CO and H₂ conversions and selectivity for gasoline was improved by adding Pd promoter (Osakoo et al., 2014). In this work, a further improvement in the conversions and selectivity of gasoline was made by changing the support to SBA-15 with different morphologies. Prieto et al. (2009) reported that a dispersion of bimetallic Ru-Co was influenced by the cavity length of SBA-15. Short cavity length eased a diffusion of CO to the catalyst active sites and gave a steady performance (Prieto et al., 2009). Our recent work showed that the addition of Pd in the Co catalysts increased hydrogenation reactions (Osakoo et al., 2014). Furthermore, the presence of Pd could prevent a formation of hard waxes which caused the catalyst deactivation (Guczi et al., 2001; Panpranot et al., 2005).

In this work SBA-15(M) was synthesized with and without the addition of decane and used as a support for Co and Co-Pd. The catalysts were characterized by N₂ adsorption–desorption, scanning electron microscopy (SEM) and transmission electron microscopy (TEM), X-ray diffraction (XRD), X-ray absorption near edge structure (XANES) and temperature-programmed reduction with hydrogen (H₂-TPR); and tested for FTS.

4.2 Experimental

4.2.1 Synthesis of SBA-15 mesoporous silica

4.2.1.1 Synthesis of modified SBA-15 (SBA-15(M))

Two point four grams of $\text{EO}_{20}\text{PO}_{70}\text{EO}_{20}$ (P123) was dissolved in 84 mL HCl solution (1.20 M), followed by the addition of 0.027 g of NH_4F thereafter the mixture was then stirred at a given temperature at 42 °C until the solution became clear (12 h). Then, 13.7g of decane and 6.64 g of TEOS were pre-mixed and introduced into the solution under mechanical stirring (300-360 rpm) (final molar ratio of P123/HCl/ NH_4F / H_2O /TEOS/decane = 1/260/1.8/11278/77/235). Decane was used as a swelling agent to control the pore size of the mesostructured silica via expansion of micelles. The above mixture solution was stirred at 42 °C for 20 h, and then transferred into an autoclave for further reaction at 100 °C for 48 h. Finally, the product was collected by filtration, washed with distilled water many times until pH nearly 6.5, dried at 80 °C overnight and calcined at 550 °C for 5 h to remove the templates and to get SBA-15(M) (Zhang et al., 2006).

4.2.1.2 Synthesis of SBA-15

Three grams of $\text{EO}_{20}\text{PO}_{70}\text{EO}_{20}$ (P123) was dissolved in 108 mL HCl solution (1.70 M) and then the mixture was stirred at 42 °C until the solution become clear(12 h). Afterward, 8g of TEOS was added slowly into the solution under mechanical stirring (300-360 rpm) (final molar ratio of P123/HCl/ H_2O / SiO_2 = 1/350/11100/55). The above mixture was stirred at 42 °C for 4 h, and then transferred into an autoclave for further reaction at 120 °C for 72 h. Finally, the product was collected by filtration, washed with distilled water many times until pH nearly 6.5,

dried at 80 °C overnight and calcined at 550 °C for 5 h to remove the templates (Prieto et al., 2009).

4.2.2 Catalyst preparation

4.2.2.1 Preparation of mono-metallic catalyst (10Co/SBA-15(M) and 10Co/SBA-15) by incipient wetness impregnation

The impregnated catalysts with absolute ethanol were prepared according to the method in the literature (Zhang et al., 2007) by dissolving $\text{Co}(\text{NO}_3)_2 \cdot 6\text{H}_2\text{O}$ with 10 wt% of Co in absolute ethanol with an appropriate amount of each pore volume material (SBA-15(M) and SBA-15). Incipient wetness volumes of the SBA-15 and SBA-15(M) were 6.0 and 8.0 mL/g, respectively. The pH of impregnating solutions was measured by a pH meter (Jenway 3510). Afterward, the cobalt nitrate solution was impregnated onto the supports. The impregnated catalyst were dried at room temperature for overnight and 120 °C for 12 h and calcined at 300 °C for 3 h.

4.2.2.2 Preparation of bimetallic catalyst Pd-Co (0.2Pd-10Co/SBA-15(M) and 0.2Pd-10Co/SBA-15) by co-incipient wetness impregnation

The catalysts were prepared by dissolving the desired amount $\text{Co}(\text{NO}_3)_2 \cdot 6\text{H}_2\text{O}$ and 0.05 M of PdCl_2 in absolute ethanol with an appropriate amount of each pore volume material (SBA-15(M) and SBA-15). The pH of impregnating solutions was measured by a pH meter (named pH meter). Afterward, the mixture solution of cobalt nitrate and PdCl_2 was impregnated to the supports. The impregnated catalyst will be dried at room temperature for overnight and 100 °C for 16 h and calcined at 300 °C for 3 h (Petrio et al., 2009).

4.2.3 Catalyst characterization

The calcined catalysts were characterized by N₂ adsorption–desorption analysis using a Micromeritics ASAP 2010 at -77 °C. Prior to the analysis, each sample was degassed at 300 °C under vacuum. TEM micrographs were obtained from a Tecnai G20 (FEI-2012, LaB6) with an accelerating voltage of 200 kV. Each sample powder was dispersed in absolute ethanol, dropped on a carbon-coated copper grid, dried and transferred into the TEM chamber. SEM micrograph was obtained from a JEOL (JSM-7800F). The sample was coated with gold by sputtering. XRD patterns were obtained from a Bruker AXS D5005 with Cu K α radiation. Additional information on the state of cobalt after calcination was studied by XANES in transmission mode at Beamline 8, the Synchrotron Light Research Institute (Thailand) with a procedure described in (Chapter III). The catalyst reduction behavior was investigated by H₂-TPR using 5 vol.% H₂ in argon with a procedure described in (Chapter III).

4.2.4 Catalytic testing for FTS

The catalytic testing in FTS was done in a stainless steel fixed-bed reactor as described previously (Chapter III). The calcined catalyst (1 g) was reduced at 350 °C for 12 h. A typical FTS was carried out at 230 °C and 5 bar for 8 h with the final gas mixture, N₂:H₂:CO volume ratio of 8:22:11 (total flow rate of 41 mL/min) corresponding to H₂:CO = 2. The permanent gases (H₂, CO, CH₄ and CO₂) were analyzed on-line by a GC equipped with a thermal conductivity detector (Hewlett Packard 5890). The C₂–C₄ gaseous products were analyzed on-line by another GC equipped with a flame ionization detector (Agilent Technologies 6890N). Cyclohexane (0.13 mol% in argon) was added as an internal standard to the product

stream before the GC analysis. The liquid products (C₅–C₉) were analyzed on-line by a GC (Agilent Technologies 6890N) equipped with a mass spectrometer detector (Hewlett Packard 5973).

The following equations were used to obtain some information resulting from catalytic studies:

$$\text{CO conversion rate (mol/g}_{\text{cat}} \cdot \text{h)} = \left(\frac{\dot{n}_{\text{CO}_{\text{in}}} - \dot{n}_{\text{CO}_{\text{out}}}}{\dot{n}_{\text{CO}_{\text{in}}}} \right) \times 60 \quad \text{.....(4.1)}$$

$$\text{H}_2 \text{ conversion rate (mol/g}_{\text{cat}} \cdot \text{h)} = \left(\frac{\dot{n}_{\text{H}_2 \text{ in}} - \dot{n}_{\text{H}_2 \text{ out}}}{\dot{n}_{\text{H}_2 \text{ in}}} \right) \times 60 \quad \text{.....(4.2)}$$

$$\% \text{ CH}_4 \text{ selectivity} = \left(\frac{\dot{n}_{\text{CH}_4 \text{ in}}}{\dot{n}_{\text{CO}_{\text{in}}} - \dot{n}_{\text{CO}_{\text{out}}}} \right) \times 100 \quad \text{.....(4.3)}$$

The yield, (Y_i)_c and selectivity, (S_i)_c of a product on a carbon basis is:

$$\text{C}_i \text{ selectivity (\% C)} = \left(\frac{\dot{n}_{\text{C}_i} \times \text{N}}{\dot{n}_{\text{CO reacted}}} \right) \times 100 \quad \text{.....(4.4)}$$

$$\text{C}_i \text{ yield (\% C)} = \left(\frac{\dot{n}_{\text{C}_i} \times \text{N}}{\dot{n}_{\text{CO in}}} \right) \times 100 \quad \text{.....(4.5)}$$

Chain growth probability (α) obtained from ASF plot in the C₃–C₉ hydrocarbon range;

$$\log (W_n/n) = (n) \log \alpha + c \quad \text{.....(4.6)}$$

Where \dot{n} = molar flow rate (mole/min), C_i = hydrocarbon with i carbon atoms, N = carbon number

4.3 Results and discussion

4.3.1 Characterization by N₂ adsorption-desorption

Adsorption–desorption isotherm of all samples is shown in Figure 4.1. Surface area and porosity are summarized in Table 4.1. The isotherm of SBA-15 (Figure. 4.1A) was type IV according to the IUPAC classification (Condon, 2006) similar to that in (Prieto et al., 2009). The initial gas uptake was from adsorption on external surface and in micropores. A hysteresis loop was observed at the P/P₀ range of 0.65–0.85. The initial uptake from Co and Co-Pd catalysts was lower than that from SBA-15 indicating a lower surface area; the hysteresis loop was smaller implying that metal oxides partially occupied the channels of SBA-15. The pore size became smaller after loaded with Co and Co-Pd (Figure 4.2A) suggesting that the pores were partially occupied.

Compared with SBA-15, the isotherm of SBA-15(M) had lower initial gas uptake with a larger and wider hysteresis loop (Figure 4.1B). The hysteresis loop at P/P₀ range of 0.65–0.85 was from mesopores and at the higher range reflected partial filling of the macropore network (Sun et al., 2007). The pore size of SBA-15(M) indicated a slightly larger diameter than that of SBA-15 (Figure 4.2B). The addition of decane to the synthesis gel of SBA-15 interrupted the particle growth producing product with less uniformity, shorter cavity length and lower surface area. The difference in surface area (SBA-15 > SBA-15(M)) was from the swelling effect which was explained by Zhang et al. (2006) and the presence of macropores. The consequent Co and Co-Pd catalysts from impregnation also had lower surface area and pore volume (Table 4.1).

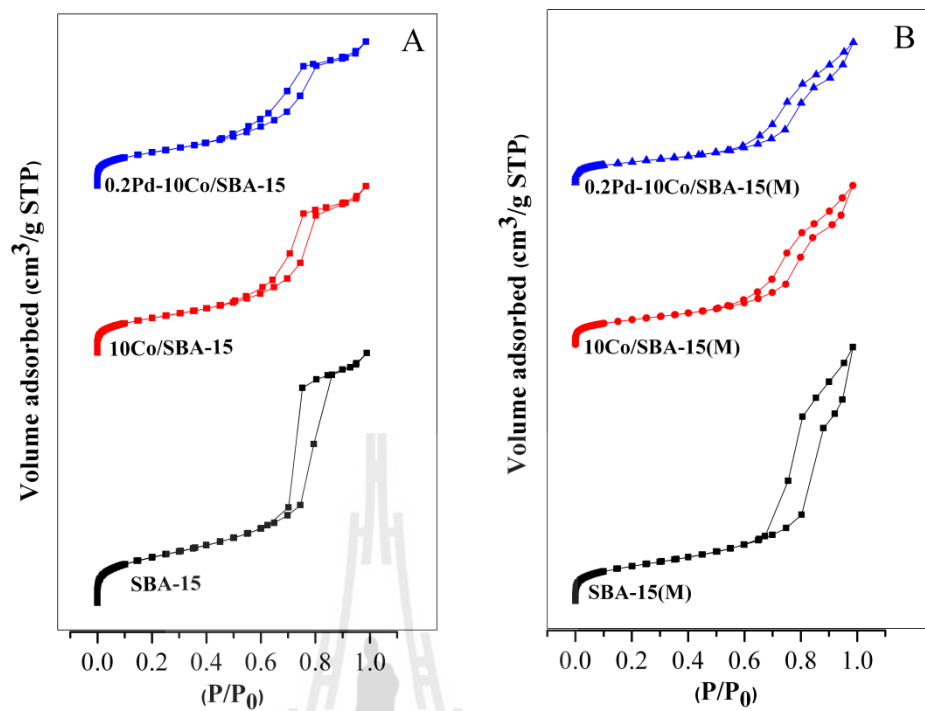


Figure 4.1 N₂ adsorption–desorption isotherms of (A) SBA-15 and its supported catalysts and (B) SBA-15(M) and its supported catalysts.

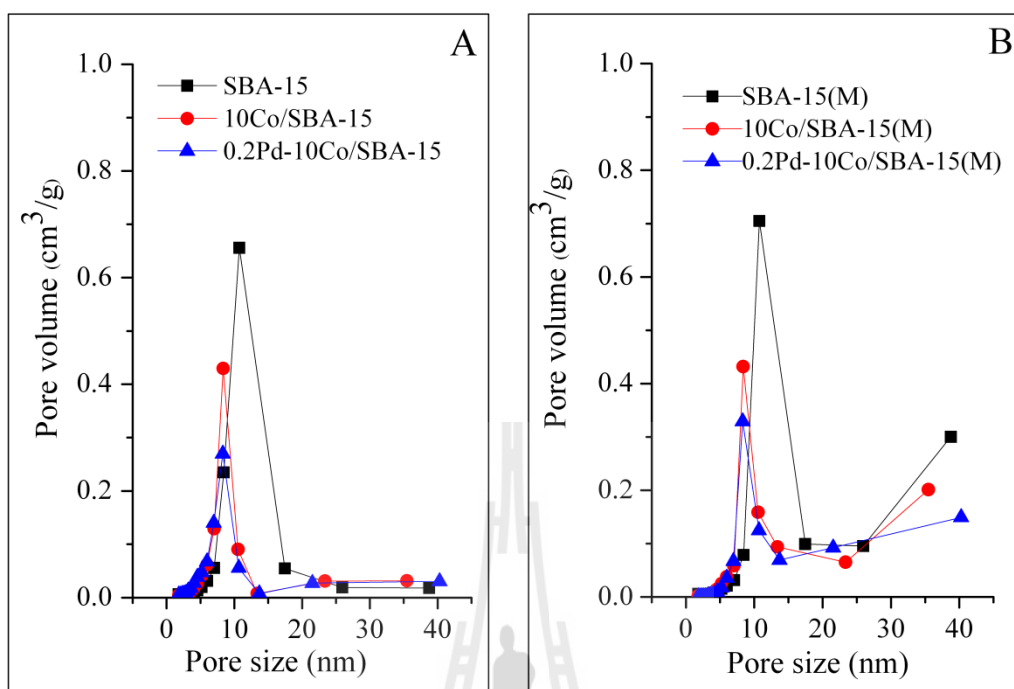


Figure 4.2 Pore size distribution; (A) SBA-15 and its supported catalysts and (B) (SBA-15(M) and its supported catalysts.

Table 4.1 Textural properties of SBA-15 and calcined catalysts determined by N₂ adsorption–desorption and XRD.

Catalysts	BET surface area (m ² /g)	Micropore area (m ² /g)	Pore volume (cm ³ /g)	^a Pore diameter(nm)	^b Crystal size of Co ₃ O ₄ (nm)
SBA-15	633	48.1	1.45	10.6	-
SBA-15(M)	487	47.2	1.48	12.1	-
0.2Pd-10Co/SBA-15	397	41.6	0.85	8.8	12.7
0.2Pd-10Co/SBA-15(M)	307	35.0	0.83	10.8	11.5
10Co/SBA-15	488	41.6	0.97	7.7	10.5
10Co/SBA-15(M)	358	42.4	0.94	10.4	9.7

^a Mean mesopore size (based on maximum for BJH pore size distribution).

^b Crystal size of Co₃O₄ (nm) calculated by Scherrer equation: $d = \frac{0.89\lambda}{B \cos\theta}$

4.3.2 Support characterization by SEM and TEM

SEM micrographs of SBA-15 and SBA-15(M) are shown in Figure 4.3. Particles of SBA-15 were uniform in shape and size with diameter and length approximately 0.5 and 1.0 μm. The particles of SBA-15(M) were less uniform and much smaller in size. Macropores could be observed on several particles. Furthermore, the difference in morphology was observed from TEM micrographs. The shorter cavity length, less particle size uniformity and macropores were observed from SBA-15(M) (Figure 4.3). Similar observation was reported by Sun et al. (2007).

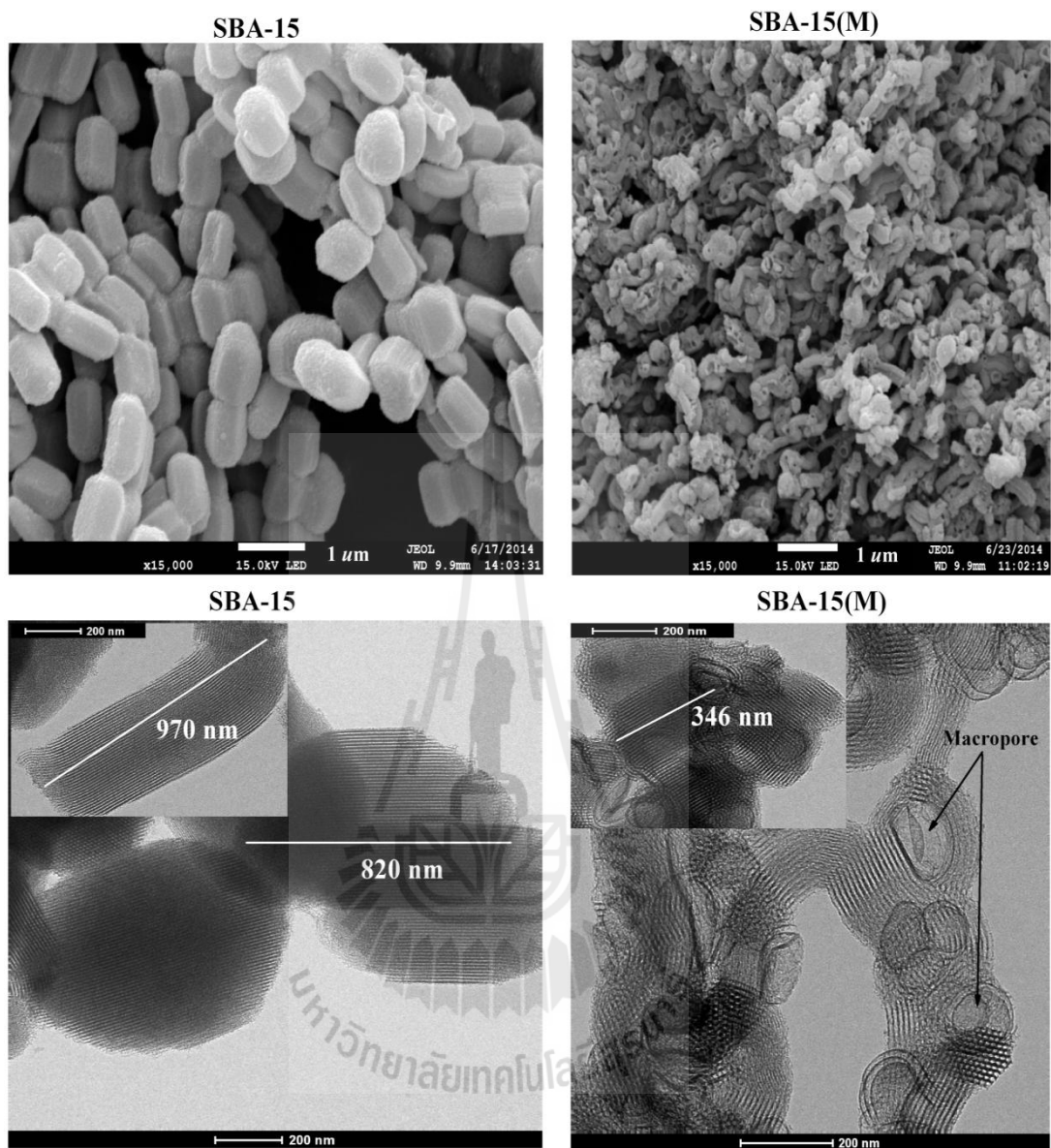


Figure 4.3 (Top) SEM and (bottom) TEM micrographs of SBA-15 and SBA-15(M).

4.3.3 Catalyst Characterizations by XRD and TEM

The XRD pattern of SBA-15 and its catalysts in low-angle range (Figure. 4.4A) show the characteristic peaks of ordered hexagonal mesoporous structure (Zhang et al., 2006; Tong et al., 2011; Taghavimoghaddam, Knowles and chaffee, 2012). All peaks in the pattern of 10Co/SBA-15 and 0.2Pd-10Co/SBA-15 had lower intensity than those of SBA-15 due to secondary scattering by metal oxides (Zhang et al., 2006; Taghavimoghaddam, Knowles and chaffee, 2012). The oxides likely resided in the cavities and the confined nanoparticles could decrease scattering contrast between the channel and the wall. The distribution of the oxides could be seen in the TEM image (Figure. 4.5).

Compared with SBA-15, the XRD peaks of SBA-15(M) slightly shifted to lower angle (Figure 4.4B). The intensity of the first peak was higher indicating the abundance of the plane (100). The addition of decane to the synthesis gel could interrupt particle growth, caused the micelle expansion and resulted in smaller and less uniform particle size with shorter channel length (Zhang et al., 2006; Sun et al., 2007).

XRD patterns in the high-angle range of the catalysts after calcination (Figure. 4.4C) consisted of peaks corresponding to spinel Co_3O_4 [JCPDS PDFNo.42-1467]. The crystallite sizes calculated from Scherrer equation are included in Table 4.1. The size decreased in the following order: 0.2Pd-10Co/SBA-15 > 0.2Pd-10Co/SBA-15(M) > 10Co/SBA-15 > 10Co/SBA-15(M). The crystallite size of Co_3O_4 on SBA-15(M) was smaller than that on SBA-15 indicating a better dispersion than on SBA-15. The crystallite sizes in monometallic catalysts were smaller than in the bimetallic ones probably from an influence of Pd during the impregnation. The

difference in crystallite size was also confirmed by XANES. In addition, the peaks of Pd oxides were not observed by XRD due to low loading.

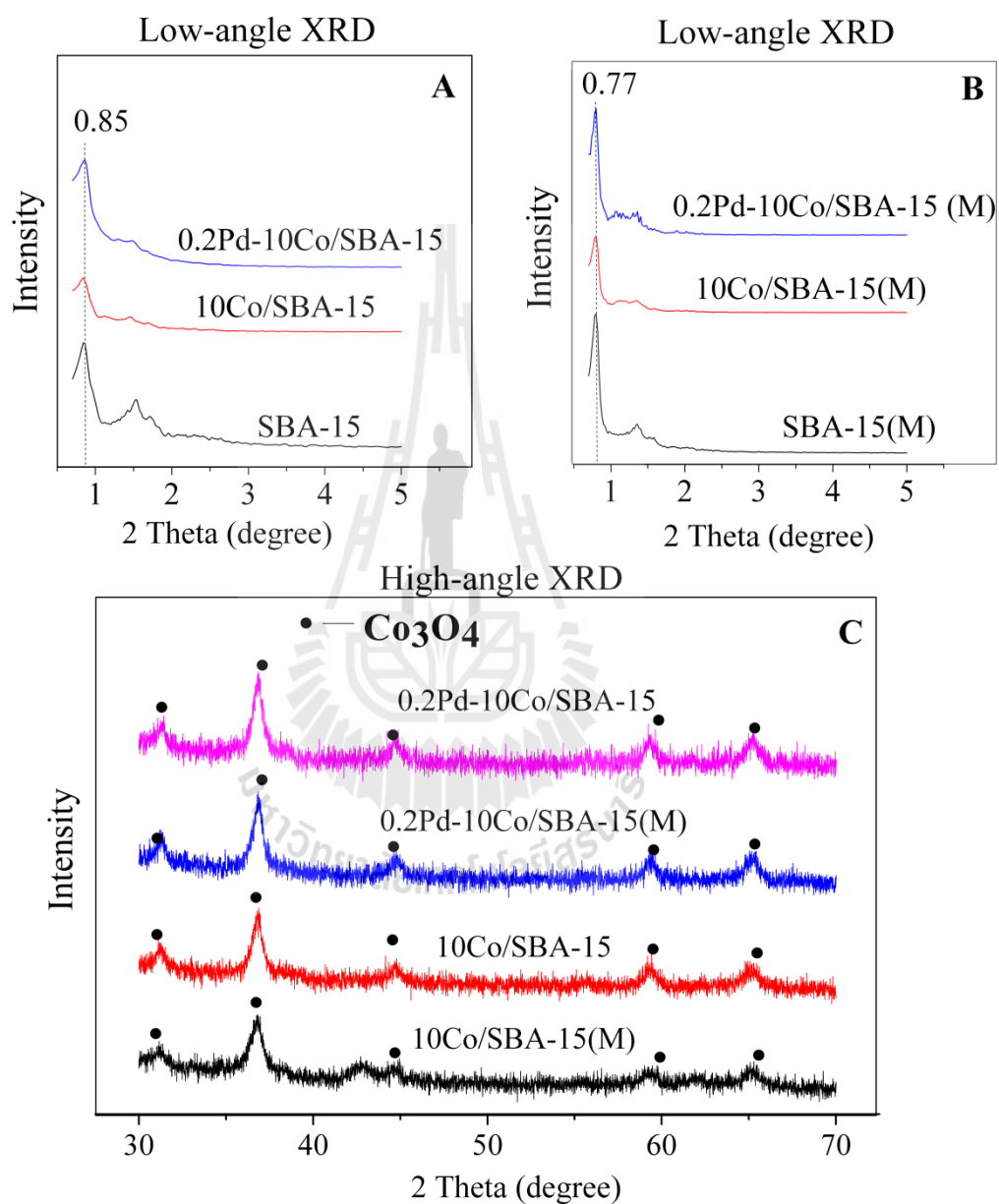


Figure 4.4 XRD patterns of support and calcined catalysts: (A) and (B) low-angle range and (C) high-angle range.

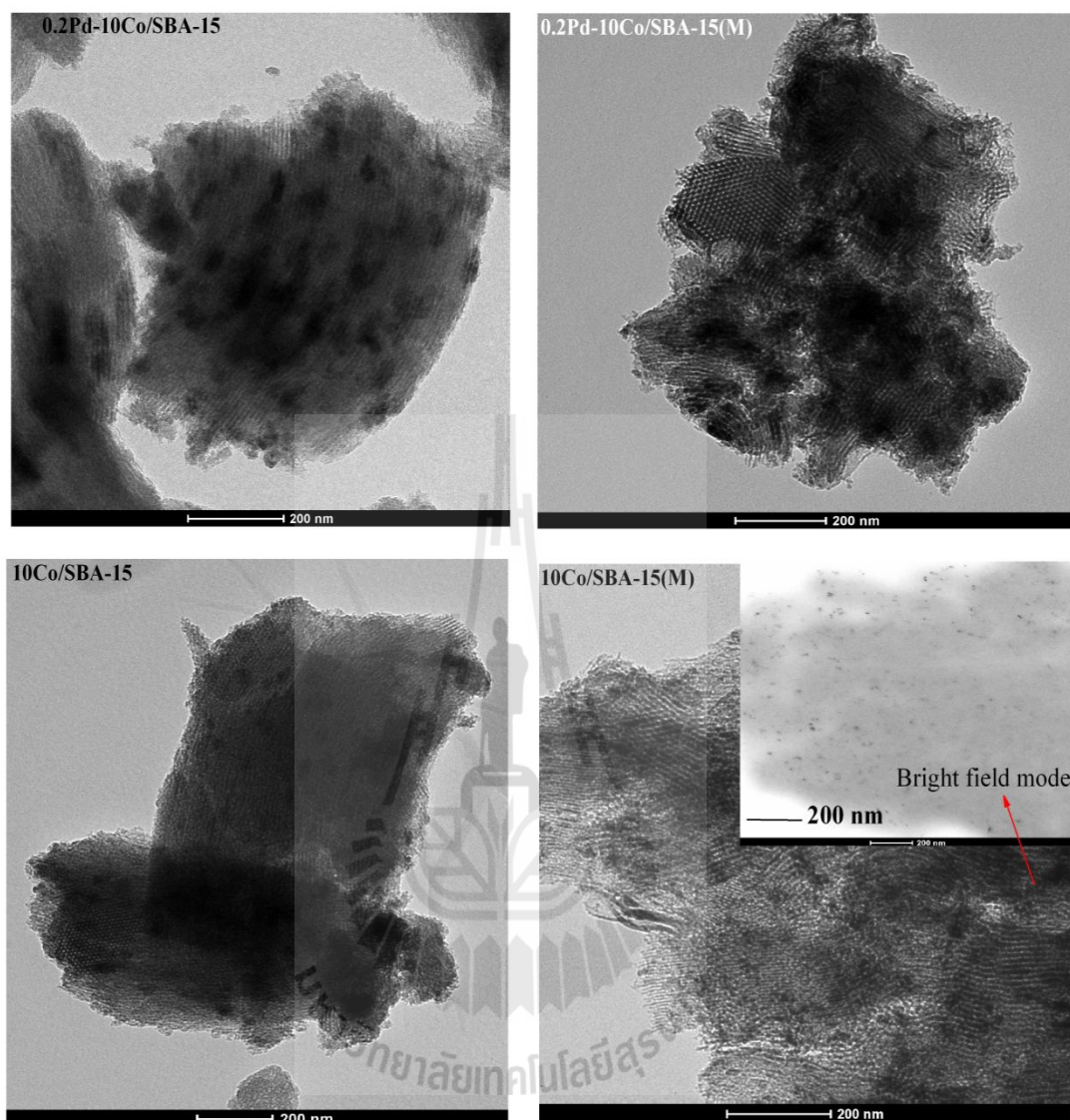


Figure 4.5 TEM images of calcined catalysts.

4.3.4 Characterization by XANES

XANES spectra of the calcined catalysts were similar to that of Co_3O_4 (Figure 4.6). The white line intensity (the strongest peak) decreased as follows: $0.2\text{Pd-}10\text{Co/SBA-}15 > 0.2\text{Pd-}10\text{Co/SBA-}15(\text{M}) > 10\text{Co/SBA-}15 > 10\text{Co/SBA-}15(\text{M})$. The lower intensity indicated the smaller particle size of Co_3O_4 which meant a better

dispersion. Thus, the best dispersion was in 10Co/SBA-15(M). The results from XANES were consistent with the crystallite size from XRD. In another study (Osakoo et al., 2013) XANES showed that catalysts prepared by reverse micelle precipitation had better dispersion of Co_3O_4 on SiO_2 than that from impregnation.

Furthermore, the distribution of metal cations from impregnation on the support depended on electrostatic interactions between the metal precursor and the support silanol groups (Mäki-Arvela and Murzin, 2013). At the pH above the point of zero charge (PZC), the surface charge is negative. The PZC of SBA-15 was at the pH ~ 3.6 (Gao et al., 2007), lower than the pH values of the Co impregnating solutions for SBA-15 and SBA-15(M) which were 4.12 and 4.23, respectively. Thus, the support surface charge became negative and interacted strongly with the cobalt cations leading to a high dispersion. In contrast, the pHs of Co-Pd impregnating solution for SBA-15 and SBA-15(M) were 2.24 and 2.63, respectively, lower than the PZC of SBA-15. Consequently, the surface charge became positive and repulsed the metal cations leading to low dispersion (Mäki-Arvela and Murzin, 2013).

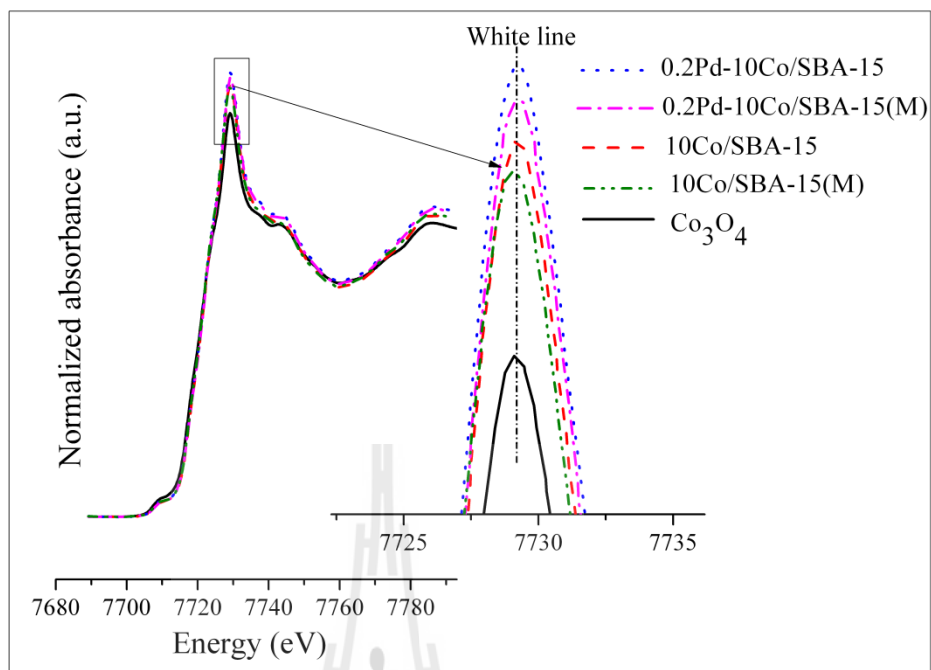


Figure 4.6 XANES spectra of calcined catalysts.

4.3.5 Characterization by TPR

The TPR profiles of monometallic catalysts (Figure. 4.7) consisted of three peaks corresponding to the reduction of Co_3O_4 to CoO , CoO to Co^0 and cobalt species with strong metal-support interaction to Co^0 (Taghavimoghaddam, Knowles and chaffee, 2012). The bimetallic catalysts had two peaks at a lower temperature than the monometallic catalysts. The presence of Pd enhanced the reducibility of cobalt oxides. The Pd^{2+} ions were reduced easily (Stonkus et al., 2009) and the resulting metallic Pd sites became the adsorption sites for hydrogen which could spill over to reduce the adjacent cobalt oxides (Roessner, Roland and Braunschweig, 1995). The reduction peak above 600°C was not observed in the profiles of bimetallic catalysts suggesting that the cobalt species had a weaker interaction with the support (Xiong et al., 2009)

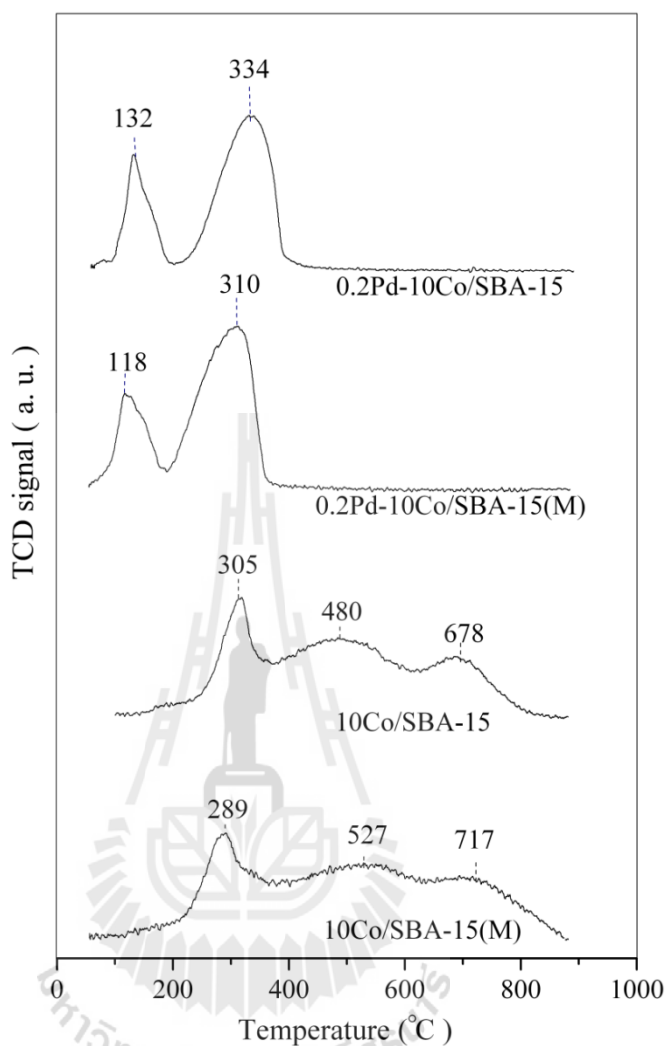


Figure 4.7 H₂-TPR profiles of calcined catalysts.

4.3.6 FTS activity

Conversions of CO and H₂ from all catalysts are shown in Figure 5. The most steady conversion and selectivity was obtained from 10Co/SBA-15(M). The conversions from mono- and bimetallic catalysts on SBA-15(M) were higher than those on SBA-15. The shorter cavity length and the presence of macropores in SBA-15(M) could enhance diffusion of the reactants, intermediates, and products (Witoon,

Chareonpanich and Limtrakul, 2011). On the same support, the conversions from the monometallic catalysts were higher than those from the bimetallic catalysts. This could be the consequence of the better dispersion of cobalt, i.e., richer adsorption sites for CO and hydrogen (Osakoo et al., 2013). In the case of bimetallic catalysts, the H₂ conversions increased gradually with time because of the presence of Pd enhanced hydrogen adsorption (Roessner, Roland and Braunschweig, 1995).

Table 4.2 shows the product selectivity at 8 h, including alcohol, CO₂, CH₄, paraffins and olefins in C₂–C₄, C₅–C₉ and C₁₀₊, yield of C₅–C₉ products; and chain growth probability (α). Compared to the results from previous work (Osakoo et al., 2013), changing the support from SiO₂ to SBA-15 increased conversions of CO and H₂, selectivity for gasoline range and paraffins. On SBA-15, the monometallic catalysts produced a small amount of CO₂ probably from the water–gas shift reaction (WGS) catalyzed by the unreduced cobalt oxide which interacted strongly with the support (Matinez et al., 2003). 10Co/SBA-15 gave the highest C₁₀₊ selectivity and α , probably due to the longest residence time of reactants and intermediates. With shorter cavity length in 10Co/SBA-15(M), the C₁₀₊ selectivity and α slightly decreased in concurrence with the increase of CO₂, alcohol and CH₄. With the Pd promoter, 0.2Pd-10Co/SBA-15 was found to give higher selectivity of alcohol, paraffin and C₅–C₉. The presence of Pd increased the hydrogenation rate which lowered the chain growth probability and the ratio of α -olefin/ β -olefin in C₄ (Figure 4.9). Pd also promoted the formation of oxygenated products, particularly ethanol and methanol (Ma et al., 2012). Note that the selectivity from all catalysts was not compared at similar conversions. Despite having the lowest selectivity for C₅–C₉ product, 10Co/SBA-15(M) still gave the highest yield of C₅–C₉ due to the highest

conversions of CO and H₂. The yield was also higher than that from 10Co/SiO₂ (Osakoo et al., 2013).

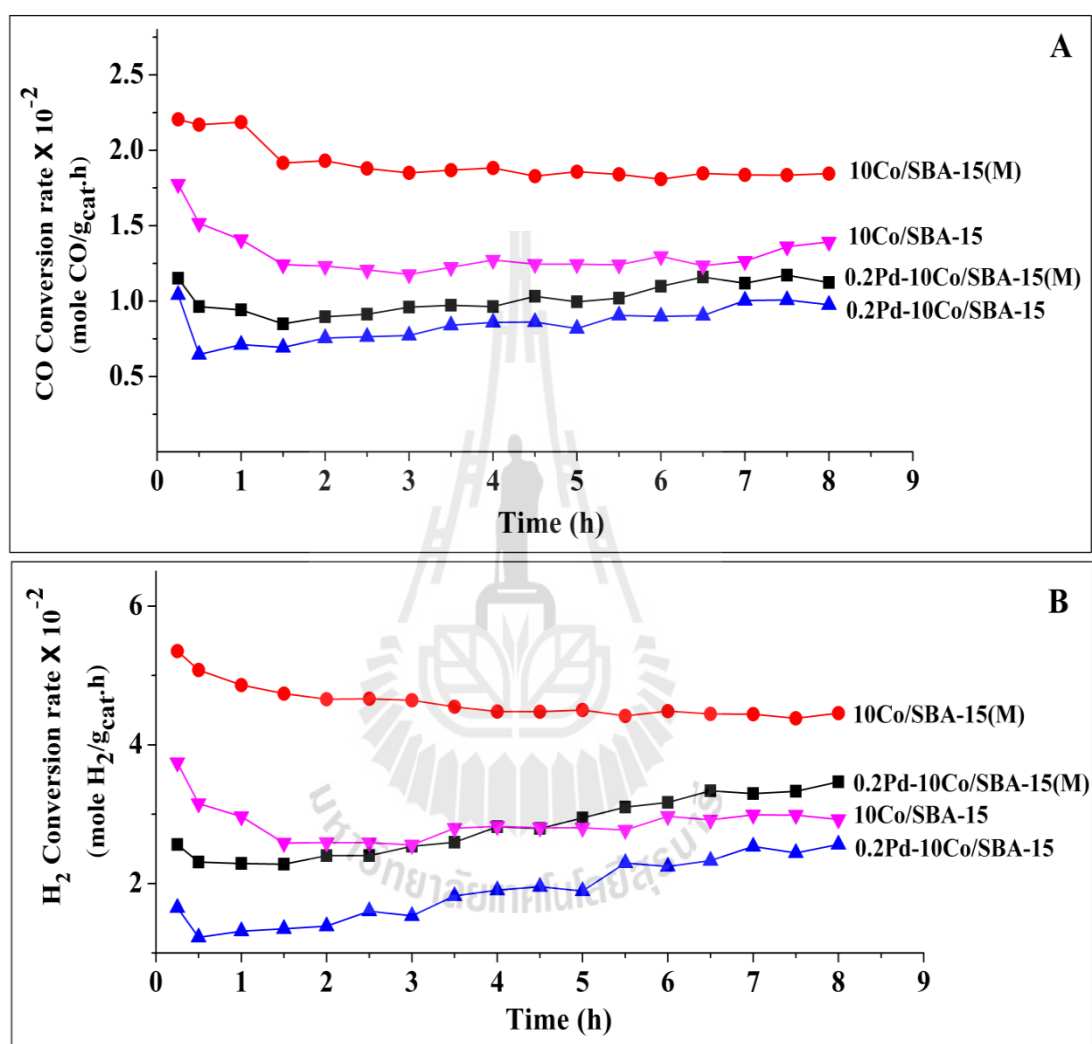


Figure 4.8 Conversions of CO and H₂ as a function of time on stream.

Table 4.2 FTS activity, CO₂ selectivity and hydrocarbon selectivities calculated at 8 h of time on stream.

Samples	$-r_{\text{CO}} \times 10^{-2}$ (mol CO/g _{cat} .h)	$-r_{\text{H}_2} \times 10^{-2}$ (mol H ₂ /g _{cat} .h)	% CO ₂ selectivity ^a	% ROH selectivity ^a	% Hydrocarbon selectivity ^a					C ₅ -C ₉ yield	α^b
					CH ₄	paraffin		olefin			
						C ₂ -C ₄	C ₂ -C ₄	C ₅ -C ₉	C ₁₀₊		
10Co/SBA-15	1.4	2.9	2.3	0.2	20.3	7.7	2.4	23.0	44.1	15.4	0.80
0.2Pd-10Co/SBA-15	0.8	2.5	0.0	0.7	26.1	15.7	1.1	31.5	24.9	8.3	0.74
10Co/SBA-15(M)	1.8	4.5	3.4	0.3	24.2	7.4	1.5	19.4	43.8	16.9	0.76
0.2Pd-10Co/SBA-15(M)	1.1	3.4	0.0	0.8	27.8	16.1	0.5	24.9	29.9	9.8	0.71
10Co/SiO ₂	0.7	1.1	0.0	0.7	4.8	2.6	3.8	17.0	71.1	3.9	0.83

^a Calculation based on % C,

^b Chain growth probability (α) obtained from ASF plot in the C₃-C₉ hydrocarbon range; $\log (Wn/n) = (n) \log \alpha + c$

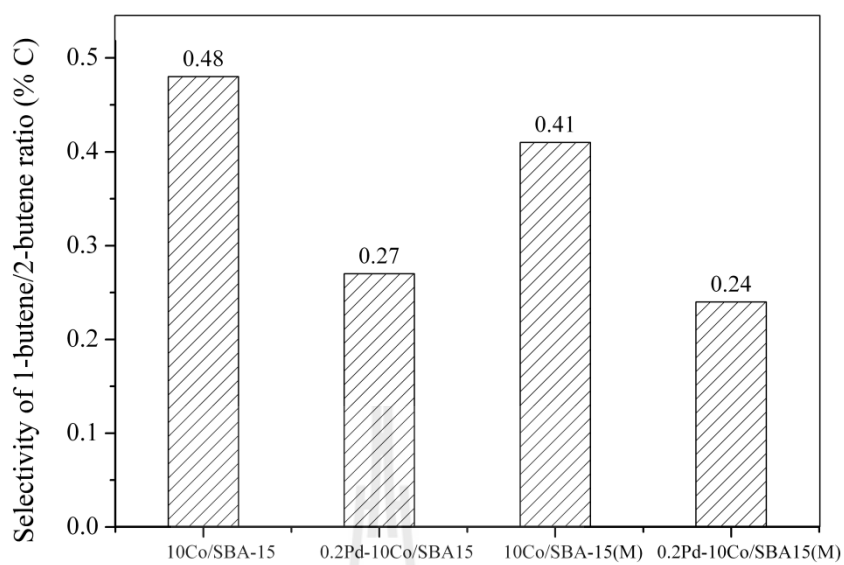
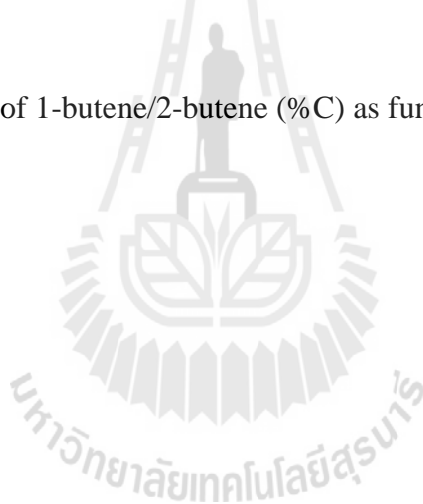


Figure 4.9 Selectivity of 1-butene/2-butene (%C) as function of catalysts.



4.4 Conclusions

Physicochemical properties of Co/SBA-15, Co-Pd/SBA-15, Co/SBA-15(M) and Co-Pd/SBA-15(M) were compared. SBA-15(M) had smaller and less uniform particle size, with shorter cavity length than SBA-15. In Co and Co-Pd catalysts, cobalt phase was Co_3O_4 and the crystallite size decreased in the following order: 0.2Pd-10Co/SBA-15 > 0.2Pd-10Co/SBA-15(M) > 10Co/SBA-15 > 10Co/SBA-15(M). In catalytic testing for Fischer-Tropsch Synthesis (FTS), the conversions of CO and H_2 on Co/SBA-15(M) were higher and more steady than those on Co/SBA-15 likely due to the ease of diffusion of reactants to and from the active sites. The addition of Pd enhanced the reduction of cobalt oxides and changed the FTS activity. The bimetallic catalysts gave lower CO conversion, olefin formation and chain growth probability, but higher alcohols, light paraffins and $\text{C}_5\text{--C}_9$ selectivity than the monometallic ones. However, the highest yield of $\text{C}_5\text{--C}_9$ products was obtained from 10Co/SBA-15(M).

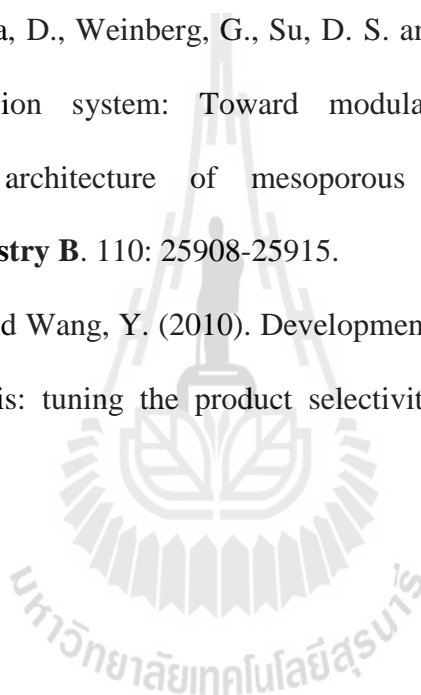
4.5 References

- Condon, J. B. (2006). **Surface Area and Porosity Determination by Physisorption: Measurement and Theory**, Elsevier, Oxford, United Kingdom.
- Gao, Q., Xu, Y., Wu, D. and Sun, Y. (2007). Adsorption of Amino Acids on SBA-15-type Mesoporous Materials. **Studies in Surface Science and Catalysis**. 170: 961-966.
- Ghampson, I. T., Newman, C., Kong, L., Pier, E., Hurley, K. D., Pollock, R. A., Walsh, B. R., Goundie, B., Wright, J., Wheeler, M. C., Meulenberg, R. W., Desisto, W. J., Frederick, B. G., and Aulin, R. N. (2010). Effect of pore

- diameter on particle size, phase, and turnover frequency in mesoporous silica supported cobalt Fischer-Tropsch catalyst. **Applied Catalysis A: General**. 388: 57-67.
- González, O., Perez, H., Navarro, P., Almedia, L. C., Pacheco, J. G. and Montes, M. (2009). Use of different mesostructured materials based on silica as cobalt supports for the Fischer-Tropsch synthesis. **Catalysis Today**. 143: 140-147
- Guczi, L., Borkó, L., Schay, Z., Bazin, D. and Mizukami, F. (2001). CO hydrogenation and methane activation over Pd-Co/SiO₂ catalysts prepared by sol/gel method. **Catalysis Today**. 65: 51-57.
- Ma, W., Jacobs, G., Keogh, R., Bukur, D. B. and Davis, B. H. (2012). Fischer-Tropsch synthesis: Effect of Pd, Pt, Re, and Ru noble metal promoters on the activity and selectivity of a 25%Co/Al₂O₃ catalyst. **Applied Catalysis A: General**. 437-438: 1-9.
- Mäki-Arvela, P. and Murzin, D. Y. (2013). Effect of catalyst synthesis parameters on the metal particle size. **Applied Catalysis A: General**. 451: 251-281
- Martínez, A., López, C., Márquez, F. and Díaz, I. (2003). Fischer-Tropsch synthesis of hydrocarbons over mesoporous Co/SBA-15 catalysts: The influence of metal loading, cobalt precursor, and promoters. **Journal of Catalysis**. 220: 486-499.
- Osakoo, N., Henkel, R., Loiha, S., Roessner, F. and Wittayakun, J. (2013). Palladium-promoted cobalt catalysts supported on silica prepared by impregnation and reverse micelle for Fischer-Tropsch synthesis. **Applied Catalysis A: General**. 464-465: 269-280.

- Panpranot, J., Tangjitwattakorn, O., Praserttham, P. and Goodwin Jr, J.G. (2005). Effects of Pd precursors on the catalytic activity and deactivation of silica-supported Pd catalysts in liquid phase hydrogenation. **Applied Catalysis A: General**. 292: 322-327.
- Prieto, G., Martı́nez, A., Murciano, R. and Arribas, M.A. (2009). Cobalt supported on morphologicallytailored SBA-15 mesostructures: the impact of pore length on metal dispersion and catalytic activity in the Fischer-Tropsch synthesis. **Applied Catalysis A: General**. 367: 146-15.
- Roessner, F., Roland, U. and Braunschweig, T. (1995). **Journal of the Chemical Society, Faraday Transactions**. 91: 1539-1545.
- Stonkus, V., Edolfa, K. Leite, L. and Sobczak J. W. (2009). Palladium-promoted Co-SiO₂ catalysts for 1, 4-butanediol cyclization. **Applied Catalysis A: General**. 362: 147-154.
- Sun, J., Ma, D., Zhang, H., Bao, X., Weinberg, G. and Su, D. (2007). Macro-mesoporous silicas complex and the carbon replica. **Microporous Mesoporous Materials**. 100: 356-360
- Taghavimoghaddam, J., Knowles, G. P. and Chaffee, A. L. (2012). Preparation and characterization of mesoporous silica supported cobalt oxide as a catalyst for the oxidation of cyclohexanol. **Journal of Molecular Catalysis A: Chemical**. 358: 79-88.
- Tang, C., Zhang, H., Sun, C., Li, J., Qi, L., Quan, Y., Gao, F. and Dong, L. (2011). An efficient strategy for highly loaded, well dispersed and thermally stable metal oxide catalysts. **Catalysis Communications**. 12: 1075-1078.

- Witoon, T., Chareonpanich, M. and Limtrakul, J. (2011). Effect of hierarchical meso-macroporous silica supports on Fischer-Tropsch synthesis using cobalt catalyst. **Fuel Processing Technology**. 92: 1498-1505.
- Xiong, H., Zhang, Y., Liew, K. and Li, J. (2009). Ruthenium promotion of Co/SBA-15 catalysts with high cobalt loading for Fischer-Tropsch synthesis. **Fuel Processing Technology**. 90: 237-26.
- Zhang, H., Sun, J., Ma, D., Weinberg, G., Su, D. S. and Bao, X. (2006). Engineered complex emulsion system: Toward modulating the pore length and morphological architecture of mesoporous silicas. **The Journal of Physical Chemistry B**. 110: 25908-25915.
- Zhang, Q., Kang, J. and Wang, Y. (2010). Development of novel catalysts for Fischer-Tropsch synthesis: tuning the product selectivity. **ChemCatChem**. 2: 1030-1050.



CHAPTER V

COMPARISON OF PdCo/SBA-15 PREPARED BY CO-IMPREGNATION AND SEQUENTIAL IMPREGNATION FOR FISCHER-TROPSCH SYNTHESIS

Abstract

Properties and catalytic performance of bimetallic Pd-Co/SBA-15 prepared by co-impregnation (0.2Pd-10Co-CIP) and sequential impregnation (0.2Pd-10Co-SIP) for Fischer-Tropsch synthesis (FTS) were investigated. After calcination, Co_3O_4 was formed and located inside the channels of SBA-15 and on external surface. The particle size of Co_3O_4 in 0.2Pd-10Co-CIP were slightly larger than that in 0.2Pd-10Co-SIP resulting in lower surface area and pore size due to more pore blocking. The larger particle size also resulted in lower reduction temperature. From FTS testing, higher conversions of CO and H_2 as well as yield of $\text{C}_5\text{-C}_9$ products were obtained from 0.2Pd-10Co-SIP.

5.1 Introduction

Fischer-Tropsch Synthesis (FTS) is a reaction of CO and H_2 to produce fuels (Zhang, Kang and Wang, 2010). The reaction involves adsorption of CO on active sites, hydrogenation to CH_x monomers and polymerization to the products (Zhang, Kang and Wang, 2010). The most superior catalyst for FTS is cobalt (Co) which gave

high selectivity for C_{5+} products and low oxygenated by-products. Its catalytic performance could be enhanced by dispersion on a support with uniform pores and high surface area (Ghampson et al., 2010), particularly, SBA-15 which has uniform hexagonal channels and high thermal stability (González et al., 2009). The specific pore diameter and length of SBA-15 determines the size of active particle in the cavities.

Recently, properties of bimetallic catalyst 0.2Pd-10Co/SBA-15 consisting of 10 wt% of Co and 0.2 wt% of Pd on SBA-15 with large and small particles were reported (Osakoo et al., 2014). Pd was added by co-impregnation to enhance the reducibility of cobalt oxides. From catalytic testing in FTS, 0.2Pd-10Co/SBA-15 had the highest selectivity for the products in gasoline range (C_5 - C_9). However, it showed unsteady and lower conversions of CO and H_2 than other catalysts. The size of cobalt oxide particles in 0.2Pd-10Co/SBA-15 was also larger than that in other catalysts probably from agglomeration during calcination. The pH of the impregnating solution which contained a mixture of $Co(NO_3)_2$ and $PdCl_2$ was 2.2, lower than the point of zero charge (PZC) of the SBA-15 support which occurred at the pH \sim 3.6 (Gao et al., 2007). Consequently, the support surface charge was positive during impregnation, repulsed the metal cations and led to a poor dispersion (Mäki-Arvela and Murzin, 2013). The effect of PZC may be avoided by changing the Pd loading method to sequential impregnation and the better dispersion was expected.

The goal of this work was to compare properties and FTS performance of bimetallic 0.2Pd-10Co/SBA-15 catalysts prepared by co-impregnation and sequential impregnation. Before testing in FTS, the catalysts were characterized by X-ray

diffraction (XRD), transmission electron microscopy (TEM), N₂ adsorption-desorption analysis, H₂-temperature programmed reduction (H₂-TPR), diffuse reflectance ultraviolet-visible spectroscopy (DR-UV-vis), X-ray absorption spectroscopy (XAS, including X-ray absorption near edge structure (XANES) and extended X-ray absorption fine structure (EXAFS) spectroscopy) and Fourier transform infrared spectroscopy.

5.2 Experimental

5.2.1 Catalyst preparation

SBA-15 was synthesized through a conventional hydrothermal method using a mixture of P123:HCl:H₂O:SiO₂ with a mole ratio 1:350:11100:55 and conditions described in (Osakoo et al., 2014; Zhang et al., 2006). Bimetallic Pd-Co catalysts containing 10 wt% of Co and 0.2 wt% of Pd supported on SBA-15 were prepared by co-impregnation (CIP) and sequential impregnation (SIP). For CIP method, SBA-15 was impregnated by a mixed solution of Co(NO₃)₂·6H₂O and PdCl₂ in absolute ethanol with the incipient wetness volume (6.0 mL/g) as described in (Chapter IV) and measured pH of impregnated solution by pH meter (Jenway 3510). For SIP, the SBA-15 was impregnated with a solution of Co(NO₃)₂·6H₂O in absolute ethanol with incipient wetness volume to produce 10 wt% Co, dried at room temperature overnight and at 120 °C for 12 h and calcined at 300 °C for 3 h to get 10Co/SBA-15. Then the obtained 10Co/SBA-15 was impregnated with a solution of PdCl₂ in absolute ethanol, dried and calcined similarly to the monometallic one. The catalysts from both preparation methods were named 0.2Pd-10Co-CIP and 0.2Pd-10Co-SIP, respectively.

5.2.2 Catalyst characterization

The calcined catalysts were characterized by XRD on a Bruker AXS D5005 with Cu K α radiation. Surface area and porosity was analyzed by N₂ adsorption-desorption using a Micromeritics ASAP 2010 at -77 °C in which the sample was degassed at 300 °C under vacuum before the analysis. TEM micrographs were obtained from a Tecnai G20 (FEI-2012, LaB6) with an accelerating voltage of 200 kV. Each sample powder was dispersed in absolute ethanol, dropped on a carbon-coated copper grid, dried and transferred into the TEM chamber. The Pd and Co content in the spent catalysts were determined by Energy Dispersive X-ray Spectroscopy (EDS) which is an attachment to the TEM. The catalyst reduction behavior was investigated by H₂-TPR using 5 vol% H₂ in Ar with a procedure described in (Chapter III). After the reduction, the catalysts were cooled to 50 °C in Ar flow and immediately passivated in molten wax under Ar atmosphere and analyzed by XRD (Jacobs et al., 2007).

State of cobalt and palladium in the calcined and reduced catalysts were studied by DR-UV-vis using a Shimadzu UV-2456 spectrophotometer in reflectance mode at room temperature against a BaSO₄ reference. The spectra were plotted according to the Kubelka-Munk equation (Osakoo et al., 2013). Additional information was obtained from analysis by XAS at Beamline 8 of the Synchrotron Light Research Institute, Thailand. The XANES and EXAFS spectra of Co K-edge were recorded at room temperature in transmission mode with a measurement procedure described in (Osakoo et al., 2013). Functional groups in the calcined catalysts were studied by FT-IR (Perkin Elmer, Spectrum GX). Each sample powder

was ground with KBr, with a weight ratio 1: 100, dried at 110°C for 10 h and pressed to form a pellets.

5.2.3 Catalytic testing for FTS

The catalytic testing in FTS was done in a stainless steel fixed-bed reactor as described previously (Osakoo et al., 2013). The calcined catalyst (1 g) was reduced at 350 °C for 12 h. A typical FTS was carried out at 230 °C and 5 bar for 8 h with the final gas mixture, N₂:H₂:CO volume ratio of 8:22:11 (total flow rate of 41 mL/min) corresponding to H₂:CO = 2. The permanent gases (H₂, CO, CH₄ and CO₂) were analyzed on-line by a GC equipped with a thermal conductivity detector (Hewlett Packard 5890). The C₂-C₄ gaseous products were analyzed on-line by another GC equipped with a flame ionization detector (Agilent Technologies 6890N). Cyclohexane (0.13 mol% in Ar) was added as an internal standard to the product stream before the GC analysis. The liquid products (C₅-C₉) were analyzed online by a GC (Agilent Technologies 6890N) equipped with a mass spectrometer detector (Hewlett Packard 5973).

The following equations were used to obtain some information resulting from catalytic studies:

$$\text{CO conversion rate (mol/g}_{\text{cat}} \cdot \text{h)} = \left(\frac{\dot{n}_{\text{CO}_{\text{in}}} - \dot{n}_{\text{CO}_{\text{out}}}}{\dot{n}_{\text{CO}_{\text{in}}}} \right) \times 60 \quad \dots\dots(5.1)$$

$$\text{H}_2 \text{ conversion rate (mol/g}_{\text{cat}} \cdot \text{h)} = \left(\frac{\dot{n}_{\text{H}_2 \text{ in}} - \dot{n}_{\text{H}_2 \text{ out}}}{\dot{n}_{\text{H}_2 \text{ in}}} \right) \times 60 \quad \dots\dots(5.2)$$

$$\% \text{ CH}_4 \text{ selectivity} = \left(\frac{\dot{n}_{\text{CH}_4 \text{ in}}}{\dot{n}_{\text{CO}_{\text{in}}} - \dot{n}_{\text{CO}_{\text{out}}}} \right) \times 100 \quad \dots\dots(5.3)$$

The yield, (Y_i)_c and selectivity, (S_i)_c of a product on a carbon basis is:

$$C_i \text{ selectivity (\% C)} = \left(\frac{\dot{n}_{C_i} \times N}{\dot{n}_{CO \text{ reacted}}} \right) \times 100 \quad \dots(5.4)$$

$$C_i \text{ yield (\% C)} = \left(\frac{\dot{n}_{C_i} \times N}{\dot{n}_{CO \text{ in}}} \right) \times 100 \quad \dots(5.5)$$

Chain growth probability (α) obtained from ASF plot in the C₃-C₉ hydrocarbon range;

$$\log (W_n/n) = (n) \log \alpha + c \quad \dots(5.6)$$

Where \dot{n} = molar flow rate (mole/min), C_i = hydrocarbon with i carbon atoms, N = carbon number

5.3 Results and Discussion

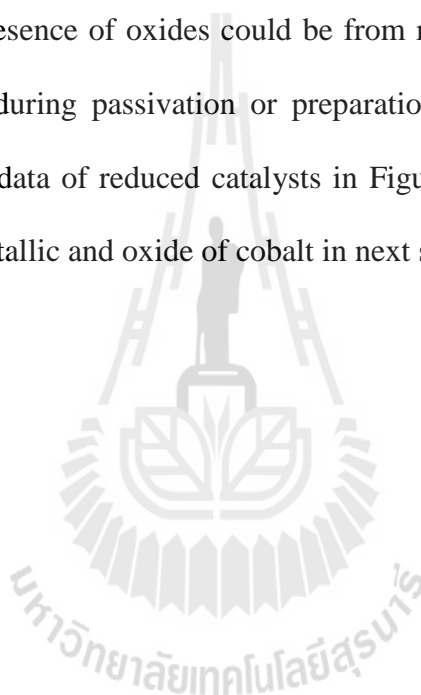
5.3.1 Catalyst characterizations by XRD and TEM

XRD pattern of SBA-15, 0.2Pd-10Co-CIP and 0.2Pd-10Co-SIP are shown in Figure 5.1. Peaks in low angle range (Figure 5.1A) are characteristics of SBA-15 (Osakoo et al., 2014). From the catalysts, the intensity of the first peak remained high whereas that of the other peaks were barely visible. TEM images (Figure 5.2) indicates that cobalt oxide resides mainly in the cavities of SBA-15. The confined nanoparticles in the cavity could decrease scattering contrast between the pore and the walls of the support (Osakoo et al., 2014; Taghavimoghaddam, Knowles and chaffee, 2012).

The XRD patterns of calcined catalysts in high angle (Figure 5.1B) consisted of peaks corresponding to spinel Co₃O₄ [JCPDS PDF No.42-1467] with similar intensity. From calculation by Scherrer formula, the crystalline size of Co₃O₄ in 0.2Pd-10Co-CIP and 0.2Pd-10Co-SIP were 12.7 and 10.8 nm, respectively. The peaks corresponding to Pd oxides in bimetallic catalysts were not observed due to low Pd loading (Osakoo et al., 2013). The forms of cobalt from both catalysts were also

confirmed by DR-UV-Vis, XANES and EXAFS (Figure 5.2 and Figure 5.3A and 5.3C) in next section.

The XRD patterns of reduced catalysts in high angle are displayed in Figure 5.1C. All catalyst consisted of peaks corresponding to metallic cobalt with hexagonal closed pack (hcp) as a major form compared to face-centered cubic closed pack (fcc) (Ducreux et al., 2009). The peaks corresponding to oxides of cobalt were observed in both catalysts. The presence of oxides could be from re-oxidation when the samples were exposed to air during passivation or preparation for the XRD analysis. The XANES and EXAFS data of reduced catalysts in Figure 5.3B and 5.3D showed the mixed character of metallic and oxide of cobalt in next section.



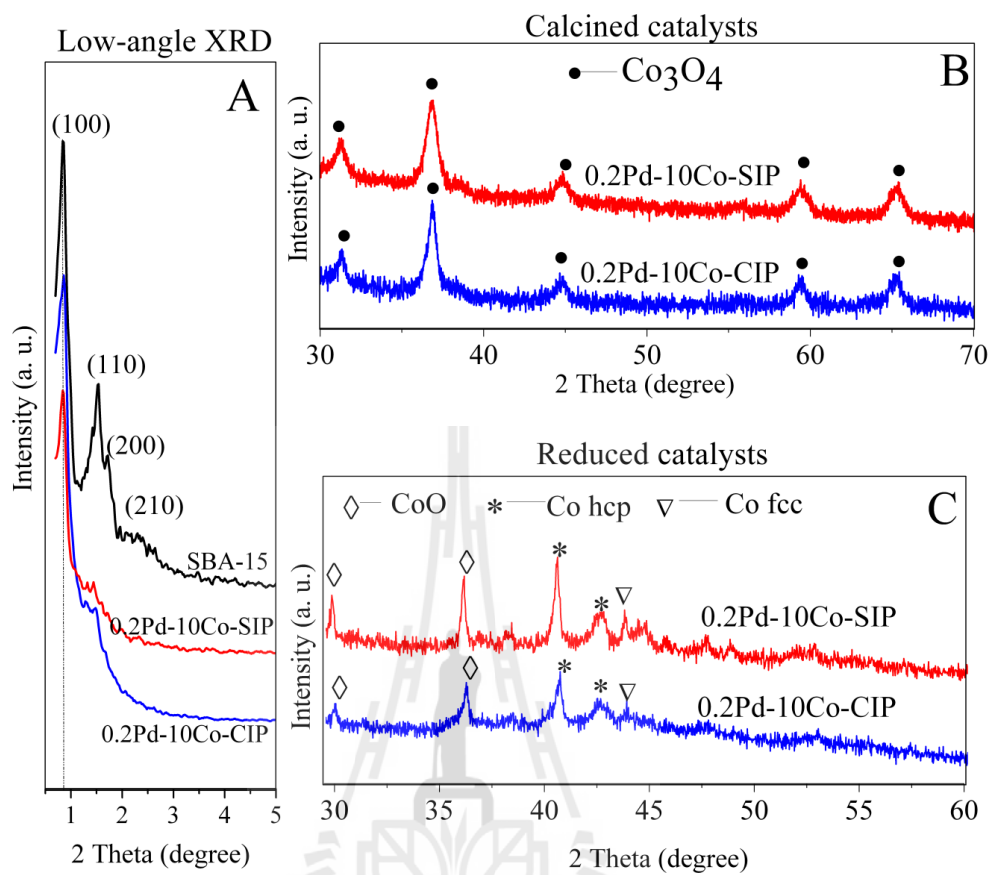


Figure 5.1 XRD patterns: (A) low-angle, (B) high-angle of calcined catalysts and (C) high-angle of reduced catalysts.

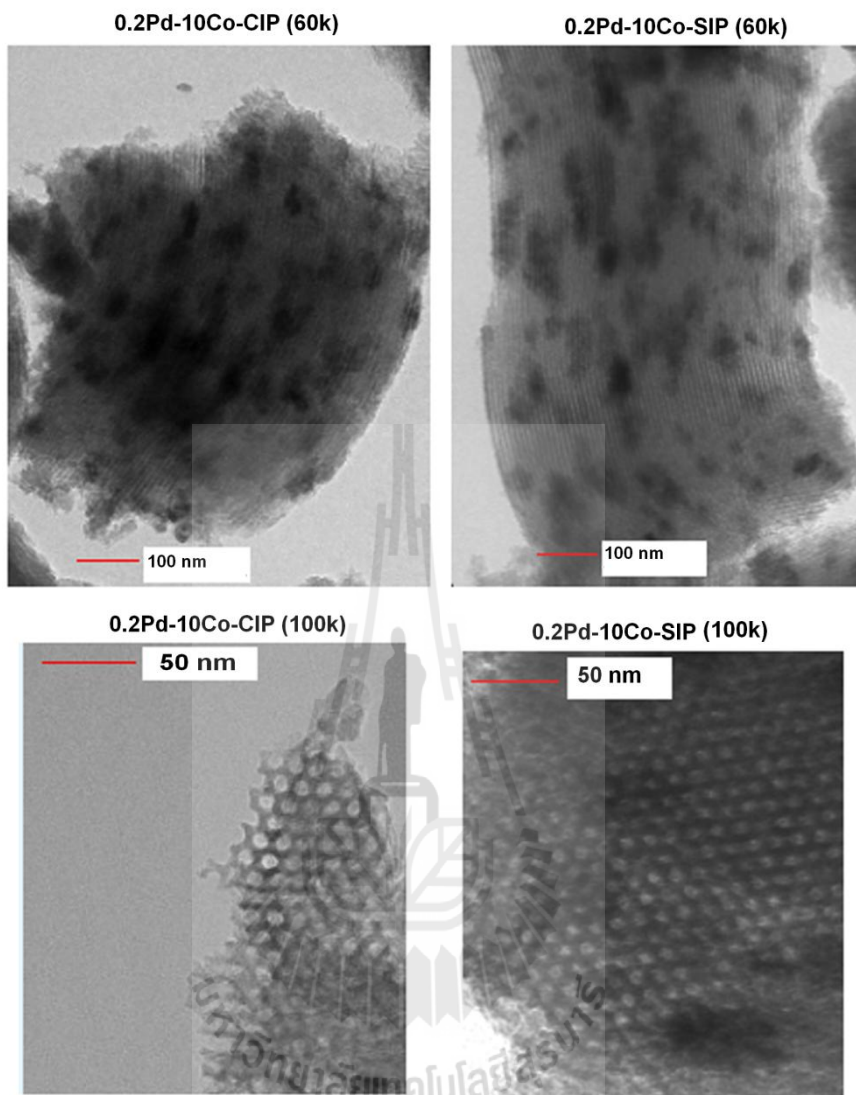


Figure 5.2 TEM images of calcined catalysts.

5.3.2 Catalyst characterizations by DR-UV-vis

DR-UV-vis spectra of SBA-15 and the calcined catalysts are shown in Figure 5.3A. The spectra of SBA-15 consisted of only one band centered around 220 nm corresponding to charge transfer from O^{2-} to Si^{4+} . For comparison, 0.2Pd/SBA-15 was prepared and characterized. An additional band around at 280 nm was observed, attributing to charge transfer in PdO (Verduraz et al., 2008). Spectra of both catalysts

consisted of five bands at 225, 269 (shoulder), 354, 414 and 704 nm. The first three bands were assigned to ligand-to-metal charge transfer (LMCT) from oxygen to Co^{3+} and Co^{2+} , respectively. The fourth band was from d-d electronic transition in octahedral coordinated Co^{3+} in well-ordered spinel Co_3O_4 species. The last band was ascribed to the electronic ligand-field transition ${}^4\text{A}_2(\text{F}) \rightarrow {}^4\text{T}_1(\text{P})$ of Co^{2+} in tetrahedral coordinate (Osakoo et al., 2013).

The spectra of all catalysts after reduction are shown in the Figure 5.3B broad flat band which covered the range of CoO (400-700 nm) implied a possibility of re-oxidation of the metallic cobalt to CoO which could occur during the passivation or the storing period. Similar observation was previously reported on the catalysts supported on silica (Osakoo et al., 2013).

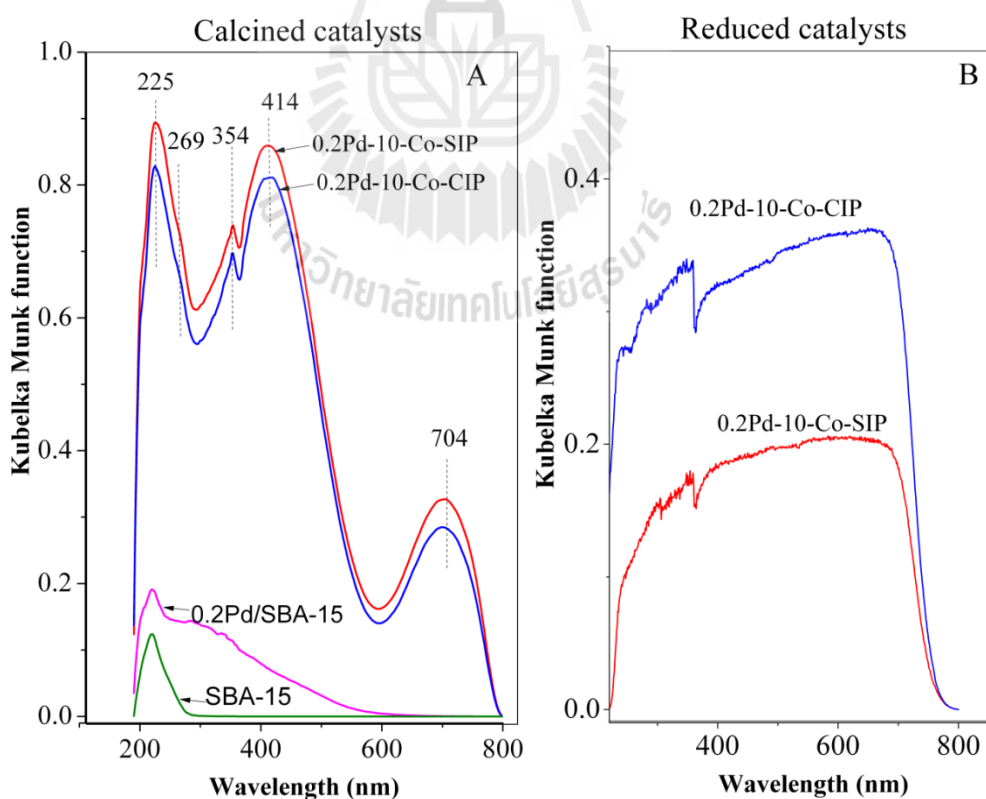


Figure 5.3 DR-UV-vis spectra of SBA-15 and catalysts.

5.3.3 Catalyst characterizations by XANES and EXAFS

The XANES spectra of calcined and reduced catalysts are shown in Figure 4A and 4B, respectively. Values of pre-edges, K edges and shifts of K-edge from that of the foil are listed in Table 5.1. The XANES spectra of both bimetallic catalysts were similar to that of Co_3O_4 (Figure 5.4A) and the edge shifts were similar in Table 5.2. The results suggested that Co_3O_4 was mainly generated in both catalysts after calcination were consistent with XRD and DR-UV-vis (Figure 5.3). The intensity of white line in 0.2Pd-10Co-CIP was higher than 0.2Pd-10Co-SIP (Figure. 5.4A). The less intense white line implied a better dispersion of Co_3O_4 , namely, smaller cluster size of Co_3O_4 (Osakoo et al., 2014). The result suggested a higher tendency of sintering of cobalt oxides in the presence of Pd prepared by CIP.

The quantities of cobalt phases in the calcined catalysts estimated by Linear Combination Fit (LCF) in the Athena Program are shown in Table 2. Co_3O_4 was the major component in all catalysts. Co_2SiO_4 was not observed in both catalysts. The absence of this phase in the bimetallic catalysts could be from the influence of Pd compared with 10Co/SBA-15 in (Osakoo et al., 2014). The LCF result was consistent with that from H_2 -TPR. A small amount CoCl_2 was observed in 0.2Pd-10Co-CIP probably from anion exchange anion between nitrate and chloride in the mixed solution of PdCl_2 and $\text{Co}(\text{NO}_3)_2$ or formation of chlorodinitrosyl cobalt complex, $\text{Co}(\text{NO})_2\text{Cl}$ as suggested by EXAFS (Figure 5.4C) which was difficult to remove by calcination at 300 °C (Xu et al., 2009).

The XANES spectra of reduced catalysts in Figure 5.4B show a mixed characteristic of metallic cobalt and oxides. Although the catalysts were reduced in

the flow reactor and immediately passivated in wax, they could be re-oxidized during the process or afterward. Because both catalysts were passivated in similar manner, it was assumed that they have similar extent of exposure to air. The LCF results of the reduced catalysts indicated that metallic Co was a major species and the higher reducibility was from 0.2Pd-10Co-SIP (Table 2). The observation of CoCl_2 in 0.2Pd-10Co-CIP implied that the reduction required a longer time or higher temperature.

Figure 5.4C shows EXAFS spectra of calcined catalysts compared with Co_3O_4 and $\text{Co}(\text{NO})_2\text{Cl}$ standard. The similarity of spectra indicated that spinel Co_3O_4 was the major component in 0.2Pd-10Co-SIP and 0.2Pd-10Co-CIP whereas the contributions from Co-N and Co-Cl were more obvious in 0.2Pd-10Co-CIP. The highest intensity of the second Co shell around Co was observed in 0.2Pd-10Co-CIP attributing to the existence of cobalt oxide with large particle size.

Figure 5.4D shows EXAFS data of the reduced catalysts compared with that of cobalt foil. The Co-Co contribution was observed in both samples confirming the reduction of cobalt oxides to the metallic form. However, the magnitude of Co-Co contribution for all catalysts was smaller than that of Co foil. This could be from the disorder in the metallic crystal structure induced by the presence of CoO and the decrease in the metal particle size (Osakoo et al., 2013; Ishida et al., 2013). The higher FT magnitude in 0.2Pd-10Co-SIP could be from higher reducibility of Co_3O_4 . Although 0.2Pd-10Co-CIP was lower temperature reduction, it had larger pore blocking, Pd covering on Co_3O_4 and the presence of $\text{Co}(\text{NO})_2\text{Cl}$ resulting to hinder the reduction of Co_3O_4 (Zhao et al., 2012; Lapidus, Tsapkina and Krylova, 2005).

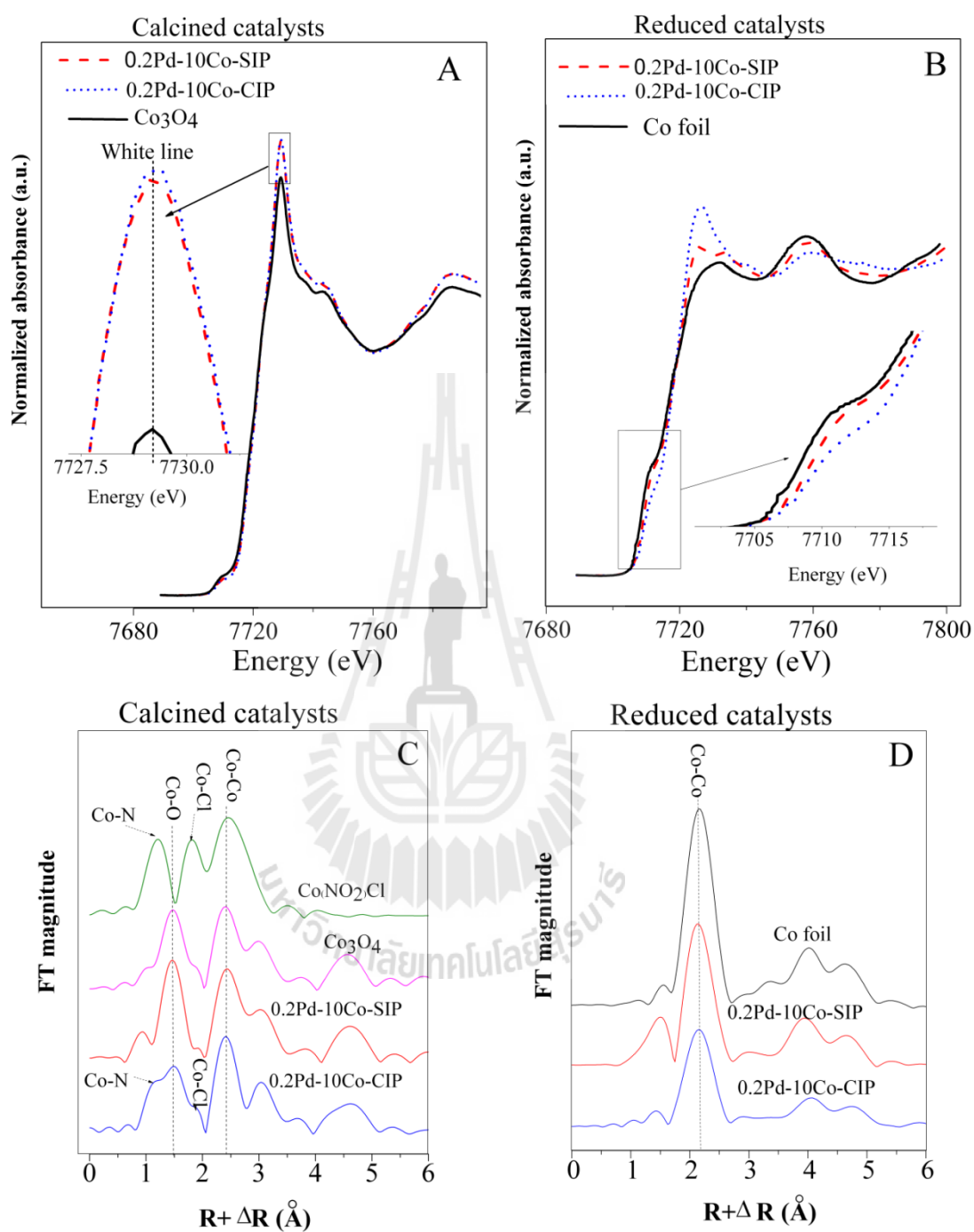


Figure 5.4 XANES spectrum of Co K-edge: (A) calcined catalysts; (B) reduced catalysts and EXAFS spectrum of Co K-edge: (C) calcined catalysts; (D) reduced catalysts.

Table 5.1 Co K-edge energy position for calcined and reduced catalysts with respect to Co metal foil (7709 keV). The edge position was obtained by the first derivative process.

Standards	Pre-edge position	K-edge position	ΔE (eV)
Co foil	-	7709.0	0.0
CoO	7709.3	7716.2	8.2
Co ₃ O ₄	7709.8	7720.9	11.9
Co ₂ SiO ₄	7710.3	7718.1	9.1
Co(NO ₃) ₂	7710.0	7717.3	8.3
CoCl ₂	7709.5	7718.0	8.8
Calcined catalysts			
0.2Pd-10Co-SIP	7709.7	7720.9	12.1
0.2Pd-10Co-CIP	7709.5	7721.1	12.1
Reduced catalysts			
0.2Pd-10Co-SIP	-	7709.9	0.9
0.2Pd-10Co-CIP	-	7715.3	7.3

Table 5.2 Composition of calcined and reduced catalysts suggested by Linear Combination Fitting (LCF) of XANES spectra.

Catalysts	Components						R-factor x10 ⁻⁴
	Co ⁰	CoO	Co ₃ O ₄	Co(NO ₃) ₂	CoCl ₂	Co ₂ SiO ₄	
Calcined catalysts							
0.2Pd-10Co-SIP	0.0	0.0	100	0.0	0.0	0.0	19
0.2Pd-10Co-CIP	0.0	0.0	91.4	0.0	8.6	0.0	16
Reduced catalysts							
0.2Pd-10Co-SIP	84.4	12	0	0.0	0.0	0.0	4
0.2Pd-10Co-CIP	48.4	42.6	0	0.0	7	0.0	8

5.3.4 Catalyst characterizations by N₂ adsorption-desorption

Adsorption-desorption isotherm of SBA-15, 0.2Pd-10Co-CIP and 0.2Pd-10Co-SIP are shown in Figure 5.5. The isotherm of SBA-15 (Figure 5.5A) was type IV according to the IUPAC classification (Osakoo et al., 2014; Condon, 2006). The initial gas uptake was from adsorption on external surface and in micropores. A hysteresis loop was observed at the P/P₀ range of 0.65–0.85. The initial uptake from both catalysts was lower than that from SBA-15 indicating a lower surface area. The hysteresis loops and corresponding pore sizes (Figure 5.5B) were smaller suggesting that metal oxides partially occupied and blocked the channels of SBA-15 (Zhao et al., 2012). The surface areas and pore volumes are summarized in Table 5.3. The higher BET surface areas and larger pore volume from 0.2Pd-10Co-SIP suggested the better dispersion of metal oxides after calcination.

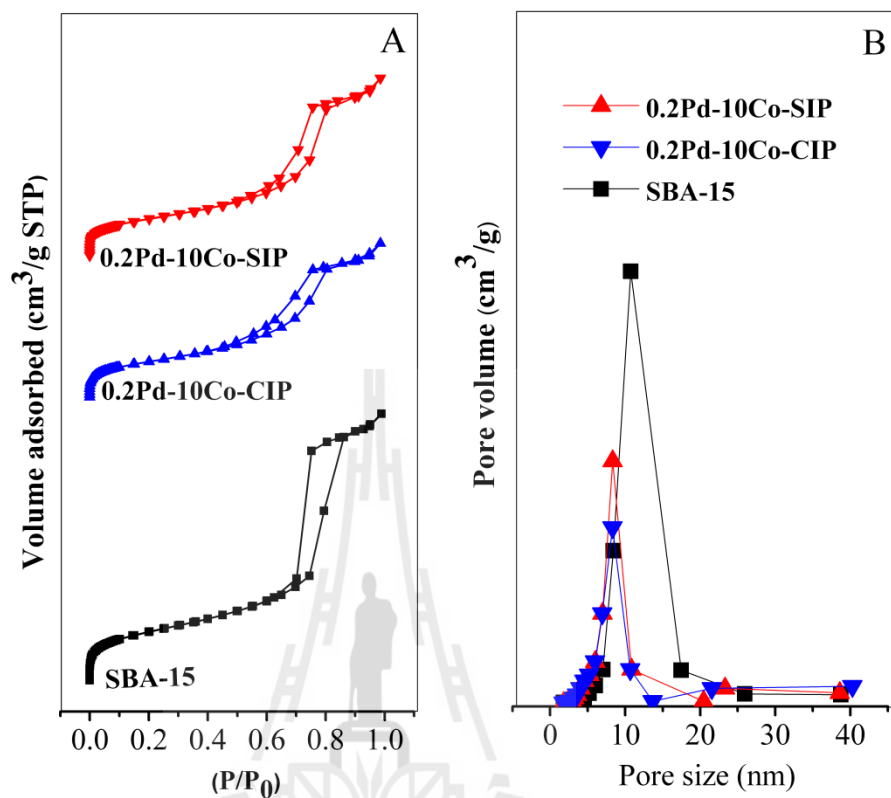


Figure 5.5 N₂ adsorption–desorption isotherms (A) and pore size distribution (B).

Table 5.3 Textural properties of SBA-15 support and calcined catalysts as determined by N₂ adsorption – desorption.

Catalysts	Textural properties			^a Crystal size of Co ₃ O ₄ (nm)
	BET surface	Micropore	Pore volume	
	area (m ² /g)	area (m ² /g)	(cm ³ /g)	
0.2Pd-10Co-SIP	473	42.6	0.95	10.8
0.2Pd-10Co-CIP	397	41.6	0.85	12.7
SBA-15	633	48.1	1.45	-

5.3.5 Catalyst characterizations by TPR

The TPR profiles of 0.2Pd-10Co-CIP and 0.2Pd-10Co-SIP are shown in Figure 5.6. The TPR profiles of the catalysts consisted of two peaks corresponding to the reduction of Co_3O_4 to CoO and CoO to Co^0 , respectively. Compared to the TPR profile of 10Co/SBA-15 catalyst (Osakoo et al., 2014), the reduction peaks of these bimetallic catalysts occurred at the lower temperature. The presence of Pd enhanced the reducibility of cobalt oxides because Pd^{2+} ions can be reduced easily (Stonkus et al., 2009) and became adsorption sites for hydrogen which could spill over to reduce the nearby cobalt oxides (Roessner, Roland and Braunschweig, 1995). The reduction peaks from 0.2Pd-10Co-CIP occurred at lower temperature than those of 0.2Pd-10Co-SIP probably due to a larger particle size and better mixing of Pd and Co species on the support which allowed a better hydrogen spillover (Osakoo et al., 2013). Satsuma et al. (2014) also suggested a better mixing of Pd and Co in bimetallic Pd-Co/ Al_2O_3 prepared by co-impregnation than by sequential impregnation.

Distribution of metal cations on the support during impregnation could be affected by electrostatic interactions between the precursor and the support (Mäki-Arvela and Murzin, 2013). The SBA-15 is mesoporous silica which is rich of silanol groups ($-\text{Si}-\text{OH}$) on the surface. Its point of zero charge (PZC) was at the pH about 3.6 (Gao et al., 2007). At the pH below the PZC, the oxides surface has positive charge and vice versa. In the case of 0.2Pd-10Co-SIP, the pH of the impregnating cobalt solution (to produce Co/SBA-15 for sequential impregnation) was 4.12, higher than the PZC of SBA-15. Thus, cobalt cations could be distributed homogeneously with interaction negatively charged surface. After 10Co/SBA-15 was impregnated with the Pd solution, it was calcined to produce 0.2Pd-10Co-SIP. Calcination two

times could make the crystal size of Co_3O_4 larger than that in monometallic (10Co/SBA-15) (Osakoo et al., 2014). In contrast, the pH of the impregnating solution to produce 0.2Pd-10Co-CIP was 2.24, lower than the PZC of SBA-15. Consequently, the surface of the support repulsed with the metal cations which caused them to agglomerate more easily leading to poorer dispersion of the cobalt oxides (Mäki-Arvela and Murzin, 2013).

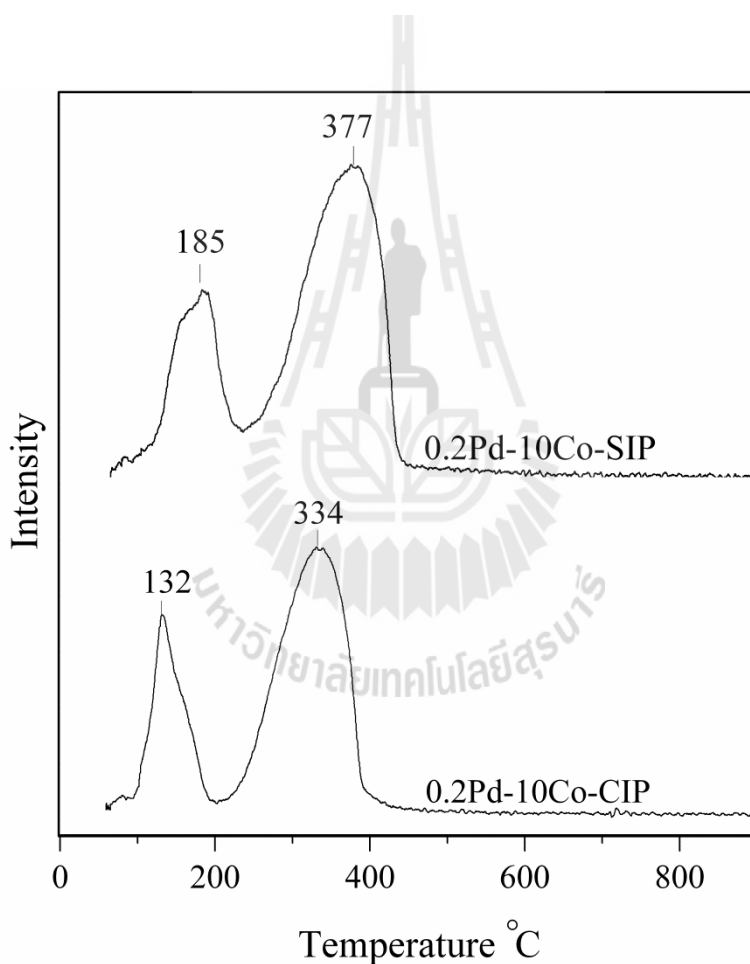


Figure 5.6 H₂-TPR profiles of 0.2Pd-10Co-CIP and 0.2Pd-10Co-SIP.

5.3.6 Catalyst characterizations by FTIR

Figure 5.7 shows the FT-IR spectra of SBA-15 and calcined catalysts. The spectra of SBA-15 included bands at 1087, 807 and 464 cm^{-1} corresponding to the Si–O–Si stretching (Rintramee et al., 2012); around 960 cm^{-1} corresponding to either Si–OH or Si–O–Si stretching; around 1630 cm^{-1} corresponding to the deformation modes of OH bonds of adsorbed H_2O ; and around 3440 cm^{-1} corresponding to the presence of surface OH groups with strong H–bonding interactions to each other (Taghavimoghaddam, Knowles and chaffee, 2012; Tanga et al., 2008). The interaction of the OH groups with the metal ions from impregnation decreased the band. The decrease could indicate the increase of metal-support interaction including probably due to the presence of Co_2SiO_4 species (Tsoncheva et al., 2012). The inset A shows that the intensity of 0.2Pd-10Co-CIP was higher than that of 0.2Pd-10Co-SIP. Such results agreed to that from XANES and TPR. Moreover, the catalysts exhibited a spectrum similar to that of SBA-15 with additional bands at 660 and 570 cm^{-1} which corresponded to Co–O vibrations in the cobalt oxide lattice (Taghavimoghaddam, Knowles and chaffee, 2012). The inset B in Figure 5.7 shows that the band of 0.2Pd-10Co-CIP was slightly more intense than from 0.2Pd-10Co-SIP inferring the larger particle size of cobalt oxides. This observation conformed to the results from XRD and TEM.

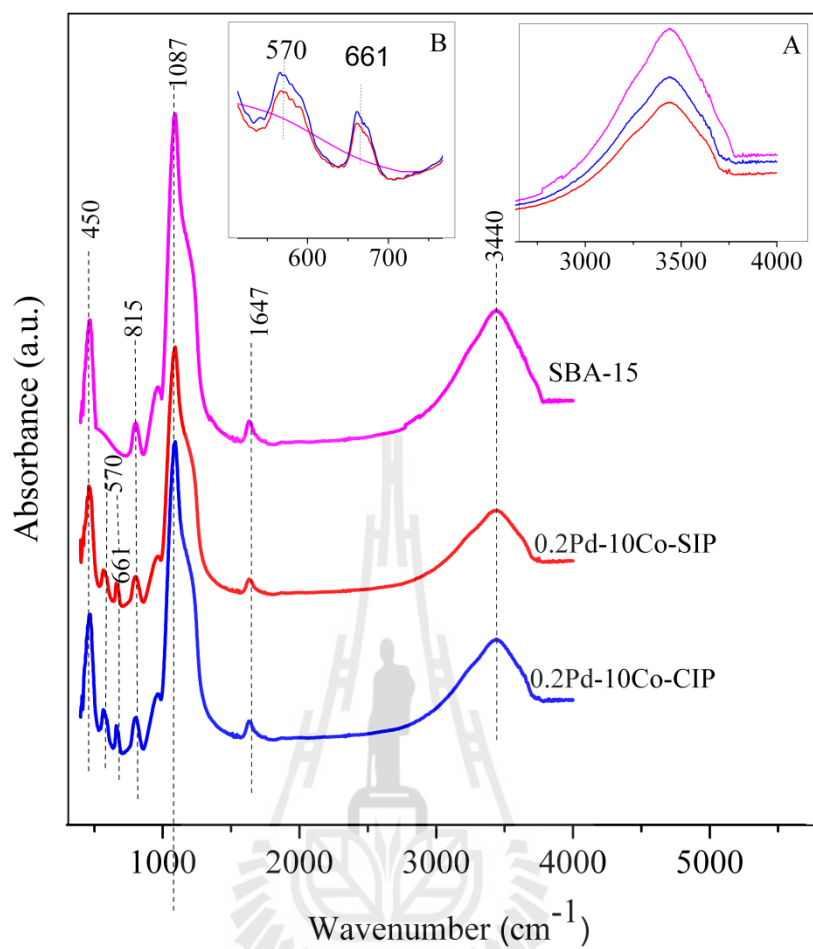


Figure 5.7 FTIR spectra of calcined catalysts.

5.3.7 Catalytic testing for FTS

Conversion rates of CO and H₂ are shown in Figure 5.8. The conversions from 0.2Pd-10Co-SIP were higher than those on 0.2Pd-10Co-CIP. This could be the consequence of the better dispersion of cobalt oxides which provided richer adsorption sites for CO and hydrogen (Osakoo et al., 2014). In the case of 0.2Pd-10Co-CIP, the H₂ conversions increased gradually with time because Pd on Co enhanced hydrogen adsorption (Ma et al., 2012).

Table 5.4 shows the product selectivity at 8 h including alcohol, CO₂, CH₄, paraffins and olefins in C₂–C₄, C₅–C₉ and C₁₀₊; and chain growth probability (α). The 0.2Pd-10Co-SIP gave higher C₅–C₉ selectivity and yield than 0.2Pd-10Co-CIP and other catalysts in our previous works (Osakoo et al., 2014; Osakoo et al., 2013). The α yield of 0.78 suggested the maximum yield in the gasoline range (Zhang, Kang and Wang, 2010).

Compared to 0.2Pd-10Co-CIP, 0.2Pd-10Co-SIP had lower hydrogenation because it provided a higher chain growth probability, selectivity of C₂–C₄ olefins, the ratio of α -olefin/ β -olefin in C₄ (i.e., 0.32 vs. 0.27) and lower CH₄ selectivity. Note that a mild hydrogenation rate during FTS was required to control the chain length of target hydrocarbon (C₅–C₉). Thus, the addition of Pd by sequential impregnation probably allowed better dispersion of Pd on SBA-15 which resulted in better catalytic performance.

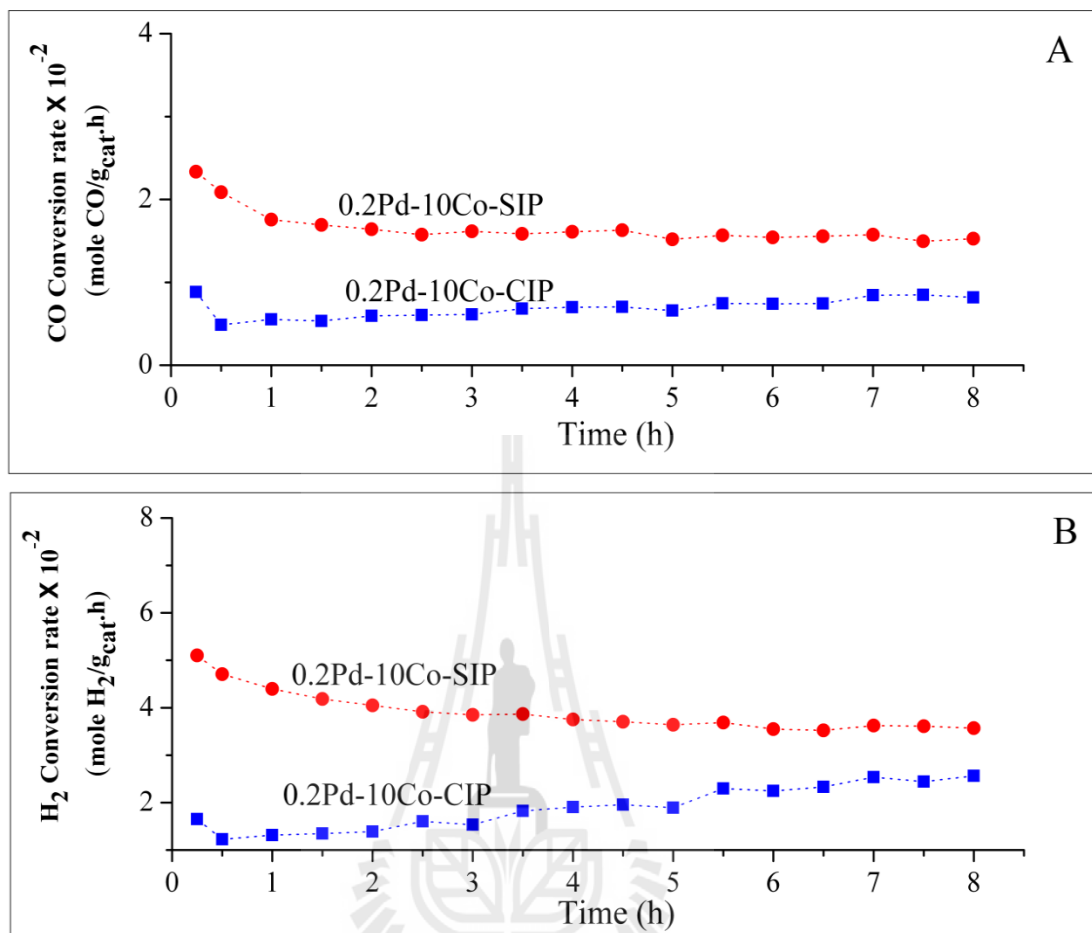


Figure 5.8 Catalytic performance on FTS: (A) CO conversions rate; (B) H₂ conversions rate.

Table 5.4 FTS activity, CO₂ selectivity and hydrocarbon selectivity calculated at 8 h of time on stream.

Samples	$-r_{\text{CO}} \times 10^{-2}$ (mol CO/g _{cat} ·h)	$-r_{\text{H}_2} \times 10^{-2}$ (mol H ₂ /g _{cat} ·h)	% ROH selectivity	% CO ₂ selectivity	% Hydrocarbon selectivity ^a					% Yield ^a (C ₅ –C ₉)	α^b
					CH ₄	Paraffin C ₂ –C ₄	Olefin C ₂ –C ₄	C ₅ –C ₉	C ₁₀ +		
					0.2Pd-10Co-SIP	1.56	3.59	0.3	0.0		
0.2Pd-10Co-CIP	0.82	2.54	0.7	0.0	26.1	15.7	1.1	31.5	24.9	8.3	0.74
10Co/SBA-15	1.39	2.92	0.2	2.3	20.3	7.7	2.4	23.0	44.1	15.4	0.80
10Co/SBA-15(M)	1.84	4.45	0.3	3.2	24.2	7.4	1.5	19.4	43.8	16.9	0.76

^a Calculated based on %C

^b Chain growth probability (α) obtained from ASF plot in the C₃–C₉ hydrocarbon range; $\log (Wn/n) = (n) \log \alpha + c$

5.4 Conclusions

Bimetallic catalysts containing 0.2 wt% Pd and 10 wt% Co on SBA-15 were prepared by co-impregnation (0.2Pd-10Co-CIP) and sequential impregnation (0.2Pd-10Co-SIP). The Co_3O_4 particle size in 0.2Pd-10Co-SIP was slightly smaller than that in 0.2Pd-10Co-CIP. The oxides particle resided in the cavities of SBA-15 and lowered the surface area and pore volume. The presence of Pd by both methods lowered reduction temperature of Co_3O_4 and CoO. The 0.2Pd-10Co-SIP provided higher conversions of CO and H_2 as well as selectivity and yield of $\text{C}_5\text{--C}_9$ products.

5.5 References

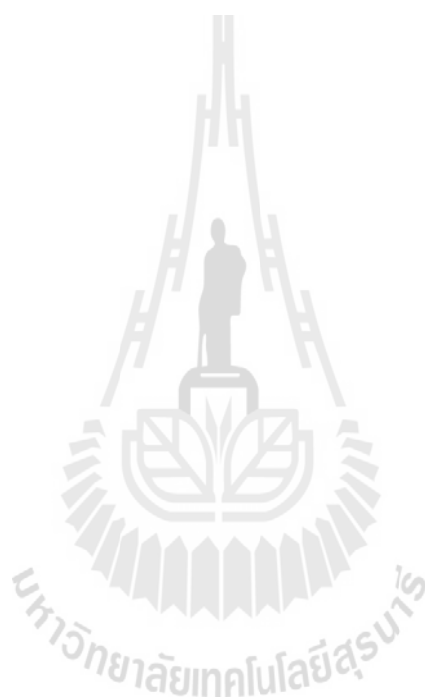
- Condon, J. B. (2006). **Surface Area and Porosity Determination by Physisorption: Measurement and Theory**, Elsevier, Oxford, United Kingdom.
- Ducreux, O., Rebours, B., Lynch, J., Roy-Auberger, M. and Bazin, D. (2009). Microstructure of supported cobalt Fischer-Tropsch catalysts. **Oil & Gas Science and Technology – Rev. IFP**. 64: 49-62.
- Gao, Q., Xu, Y., Wu, D. and Sun, Y. (2007). Adsorption of Amino Acids on SBA-15-type Mesoporous Materials. **Studies in Surface Science and Catalysis**. 170: 961-966.
- Ghampson, I. T., Newman, C., Kong, L., Pier, E., Hurley, K. D., Pollock, R. A., Walsh, B. R., Goundie, B., Wright, J., Wheeler, M. C., Meulenberg, R. W., Desisto, W. J., Frederick, B. G. and Aulin, R. N. (2010). Effect of pore diameter on particle size, phase, and turnover frequency in mesoporous silica supported cobalt Fischer-Tropsch catalyst. **Applied Catalysis A: General**. 388: 57-67.

- González, O., Perez, H., Navarro, P., Almedia, L. C., Pacheco, J. G. and Montes, M. (2009). Use of different mesostructured materials based on silica as cobalt supports for the Fischer-Tropsch synthesis. **Catalysis Today**. 143: 140-147
- Ishida, T., Yanagihara, T., Liu, X., Ohashi, H., Hamasaki, A., Honma, T., Oji, H., Yokoyama, T. and Tokunaga, M. (2013). Synthesis of higher alcohols by Fischer-Tropsch synthesis over alkali metal-modified cobalt catalysts. **Applied Catalysis A: General**. 458: 145-154.
- Janger, S. and Vannerberg, N. G. (1967). The crystal structure of modification dinitrosylcobalt chloride $[\text{Co}(\text{NO})_2 \text{Cl}]_n$. **Acta chemical scandinavica**. 21: 1183-1192.
- Jacobs, G., Ji, Y., Davis, B. H., Cronauer, D., Kropf, A. J. and Marshall, C. L. (2007). Fischer-Tropsch synthesis: Temperature programmed EXAFS/XANES investigation of the influence of support type, cobalt loading, and noble metal promoter addition to the reduction behavior of cobalt oxide particles. **Applied Catalysis A: General**. 333: 177-191.
- Lapidus, A. L., Tsapkina, M. V., Krylova, A. Y. and Tonkonogov, B. P. (2005). Bimetallic cobalt catalysts for the synthesis of hydrocarbons from CO and H₂. **Russian Chemical Reviews**. 74: 577-586
- Ma, W., Jacobs, G., Keogh, R., Bukur, D. B. and Davis, B. H. (2012). Fischer-Tropsch synthesis: Effect of Pd, Pt, Re, and Ru noble metal promoters on the activity and selectivity of a 25%Co/Al₂O₃ catalyst. **Applied Catalysis A: General**. 437-438: 1-9.
- Mäki-Arvela, P. and Murzin, D. Y. (2013). Effect of catalyst synthesis parameters on the metal particle size. **Applied Catalysis A: General**. 451: 251-281.

- Osakoo, N., Henkel, R., Loiha, S., Roessner, F. and Wittayakun, J. (2013). Palladium-promoted cobalt catalysts supported on silica prepared by impregnation and reverse micelle for Fischer-Tropsch synthesis. **Applied Catalysis A: General**. 464-465: 269-280.
- Osakoo, N., Henkel, R., Loiha, S., Roessner, F. and Wittayakun, J. (2014). Effect of support morphology and Pd promoter on Co/SBA-15 for Fischer-Tropsch Synthesis. **Catalysis Communications**. 56: 168-173.
- Rintramee, K., Föttinger, K., Rupprechter, G. and Wittayakun, (2012). Ethanol adsorption and oxidation on bimetallic catalysts containing platinum and base metal oxide supported on MCM-41. **Applied Catalysis B: Environmental**. 115-116: 225-235.
- Roessner, F., Roland, U. and Braunschweig, T. (1995). **Journal of the Chemical Society, Faraday Transactions**. 91: 1539-1545.
- Satsuma, A., Tojo, T., Okuda, K., Yamamoto, Y., Arai, S. and Oyama, J. (2014). Effect of preparation method of Co-promoted Pd/alumina for methane combustion. **Catalysis Today**. 224: 308-314.
- Stonkus, V., Edolfa, K., Leite, L. and Sobczak, J. W. (2009). Palladium-promoted Co-SiO₂ catalysts for 1,4-butanediol cyclization. **Applied Catalysis A: General**. 362: 147-154.
- Taghavimoghaddam, J., Knowles, G. P. and Chaffee, A. L. (2012) Preparation and characterization of mesoporous silica supported cobalt oxide as a catalyst for the oxidation of cyclohexanol. **Journal of Molecular Catalysis A: Chemical**. 358: 79-88.

- Tang, C. W., Wang, C. B. and Chien, S. H. (2008). Characterization of cobalt oxides studied by FT-IR, Raman, TPR and TG-MS. **Thermochimica Acta**. 473: 68-73.
- Tsoncheva, T., Gallo, A., Scotti, N., Dimitrova, M., Delaigle, R., Gaigneaux, E., Kovacheva, D., Santo, V. D. and Ravasio, N. (2012). Optimization of the preparation procedure of cobalt modified silicas as catalysts in methanol decomposition. **Applied Catalysis A: General**. 417-418: 209-219.
- Verduraz, F. B., Fiévet, F., Piquemal, J. Y., Brayner, R., Kabouss, K. E. and Soumare, Y. (2008). Nanoparticles of metal and metal oxides: some peculiar synthesis methods, size and shape control, application to catalysts preparation. **Brazilian Journal of Physics**. 39: 134-140
- Xu, S., Wang, L., Chu, W. and Yang, W. (2009). Influence of Pd precursors on the catalytic performance of Pd-H₄SiW₁₂O₄₀/SiO₂ in the direct oxidation of ethylene to acetic acid. **Journal of Molecular Catalysis A: Chemical**. 310: 138-143
- Zhang, H., Sun, J., Ma, D., Weinberg, G., Su, D. S. and Bao, X. (2006). Engineered complex emulsion system: Toward modulating the pore length and morphological architecture of mesoporous silicas. **The Journal of Physical Chemistry B**. 110: 25908-25915.
- Zhang, Q., Kang, J. and Wang, Y. (2010). Development of novel catalysts for Fischer-Tropsch synthesis: tuning the product selectivity. **ChemCatChem**. 2: 1030-1050.

Zhao, Y., Zhang, Y., Chen, J., Li, J., Liew, K. and Nordin, M. R. B. (2012). SBA-16-supported cobalt catalyst with high activity and stability for Fischer-Tropsch synthesis. **ChemCatChem**. 4: 265-272.



CHAPTER VI

CONCLUSIONS

SiO₂-supported cobalt catalysts (10 wt% Co) were prepared by impregnation (IP) and precipitation using the reverse micelle (RM) method. Co₃O₄ generated after calcination of 10Co-IP had larger particle sizes than that of 10Co-RM. The formation of Co₂SiO₄ species was observed from both catalysts. After Pd was added to both Co containing catalysts, the structure and particle size of Co₃O₄ did not change; a small amount of CoCl₂ was suggested; and the reducibility of cobalt was improved. The structure of metallic cobalt catalysts prepared by IP was mainly hcp, in contrast to the RM series where a mixed phase of hcp and fcc was found. The FTS activity of the SiO₂-support cobalt catalysts depended on particle size, reducibility and Pd addition. At similar amounts of Co and Pd, the IP series showed a higher CO conversion than that of catalysts of the RM series and the CO conversion was improved by the addition of 0.2 wt% Pd in both series. The highest CO conversion was obtained from 0.2Pd-10Co-IP. In terms of product selectivity, the IP series produced more olefins than the RM series. The addition of Pd enhanced the formation of alkanes, including methane, heavy paraffins, methyl-branched paraffin and alcohols. The improvement of Co supported on SiO₂ for FTS accomplished a strategy to produce desired paraffin products in two ranges: the formation

of C₂–C₄ paraffins is enhanced in the RM series, while the C₅–C₉ paraffins (gasoline) are selectively produced with 0.2Pd-10Co-IP.

The physicochemical properties of Co/SBA-15, Co-Pd/SBA-15, Co/SBA-15(M) and Co-Pd/SBA-15(M) were compared. SBA-15(M) had smaller and less uniform particle size, with shorter cavity length than SBA-15. In Co and Co-Pd catalysts, the cobalt phase was Co₃O₄ and the crystallite size decreased in the following order: 0.2Pd-10Co/SBA-15 > 0.2Pd-10Co/SBA-15(M) > 10Co/SBA-15 > 10Co/SBA-15(M). In catalytic testing for Fischer-Tropsch Synthesis (FTS), the conversions of CO and H₂ on Co/SBA-15(M) were higher and steadier than those on Co/SBA-15, likely due to the ease of diffusion of reactants to and from the active sites. The addition of Pd enhanced the reduction of cobalt oxides and changed the FTS activity. The bimetallic catalysts gave lower CO conversion, olefin formation and chain growth probability, but higher alcohols, light paraffins and C₅–C₉ selectivity than the monometallic ones. However, the highest yield of C₅–C₉ products obtained from 10Co/SBA-15(M).

Bimetallic catalysts containing 0.2 wt% Pd and 10 wt% Co on SBA-15 were prepared by co-impregnation (0.2Pd-10Co-CIP) and sequential impregnation (0.2Pd-10Co-SIP). The Co₃O₄ particle size in 0.2Pd-10Co-SIP was slightly smaller than that in 0.2Pd-10Co-CIP. The oxide particles resided in the cavities of SBA-15 and lowered the surface area and pore volume. The presence of Pd by both methods lowered reduction temperature of Co₃O₄ and CoO. The 0.2Pd-10Co-SIP provided higher conversions of CO and H₂, as well as selectivity and yield of C₅–C₉ products.

APPENDICES



APPENDIX A

FISCHER-TROPSCH EXPERIMENTS AND PRODUCT ANALYSIS

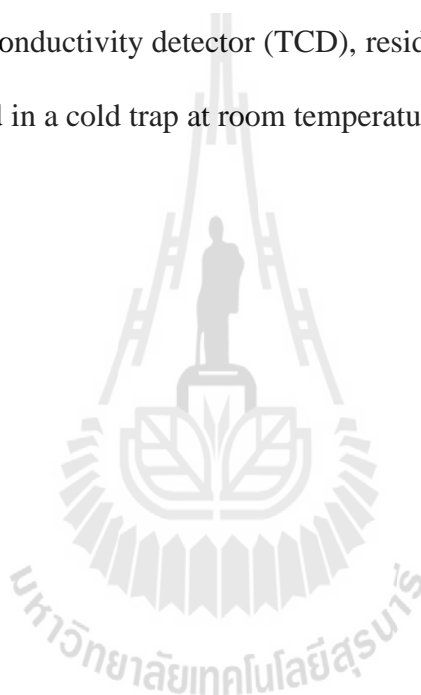
A 1 Fischer-Tropsch reactor

Figure B-1 shows the physical setup of the Fischer-Tropsch apparatus in this work. The catalytic testing for FTS was carried out in a U-tube fixed-bed reactor made from stainless steel (O.D., 0.635 mm and I.D., 0.5 mm), which was centered in an aluminum block containing two heating elements at the edges to minimize temperature gradients. Two thermocouples measured and controlled the temperature of the aluminum block and the reactor. The gas supply consisted of the reactants, pressure and balance gases, including carbon monoxide, hydrogen, nitrogen (pressure and balance gas) and a mixture of argon/cyclohexane as an internal standard (0.13 mol % cyclohexane in argon).

All gases were controlled by mass flow controllers (MFC, F-1 - 5) except the nitrogen line used to pressurize the reactor. Desired flow rate and pressure at 5.0 bar were adjusted and at the outlet of the reactor (carbon monoxide, hydrogen, nitrogen, nitrogen, argon/cyclohexane and nitrogen/pressure) was controlled by using a needle valve (NV). A 4-way valve (4WV) provided the switching of mixture gases from running through the

reactor or through a bypass line. To keep liquid products (C_5 - C_{11}) from the Fischer-Tropsch synthesis in the gas phase for the *online* gas chromatographic analyses, all lines after the reactor were heated to 180 °C until the gas chromatograph equipped with a thermal conductivity detector (GC-TCD)

A hot trap after the reactor is adjusted at 100 °C to avoid blocking of the 1/16" tubes at the gas chromatographs by organic products (C_{12+}). In order to minimize damages the thermal conductivity detector (TCD), residue C_{5+} organic products in the gas phase are collected in a cold trap at room temperature before the TCD.



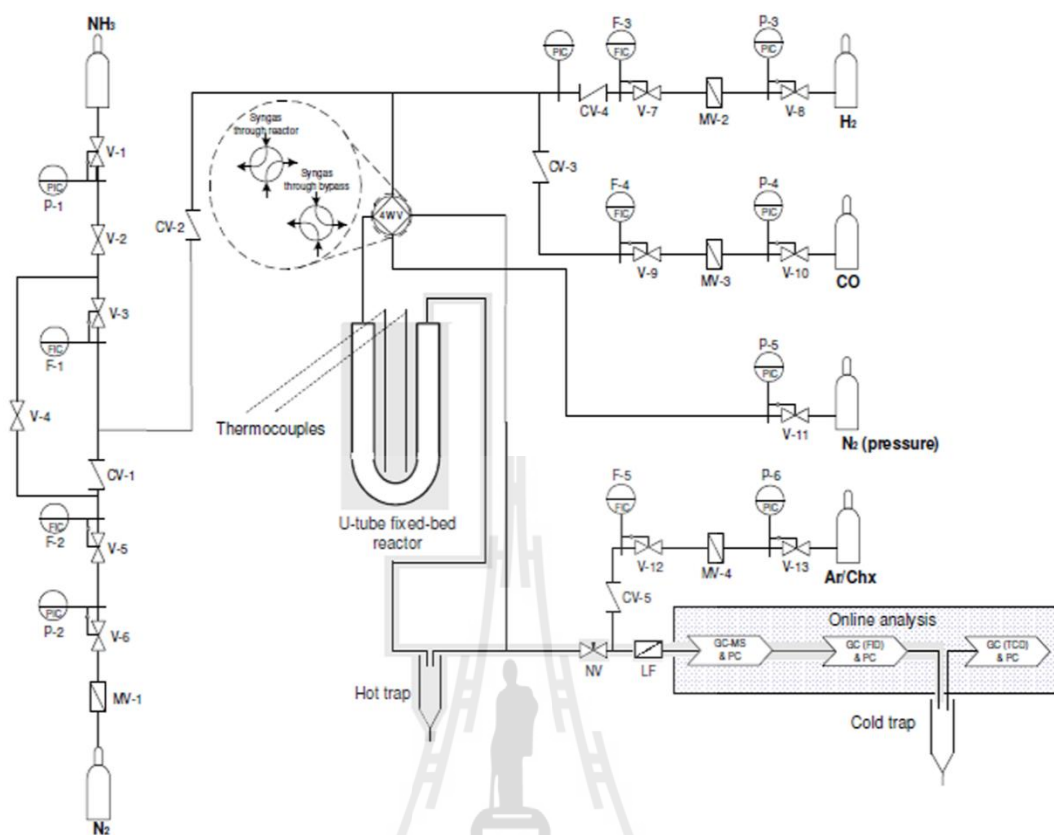


Figure A 1 Physical set-up of the experimental equipment for the Fischer-Tropsch experiments: CV-1 - 5 check valves, F-1 - 5 flow control, LF line filter, NV needle valve, MV-1 - 4 magnetic valves, V-1 - 13 one way valves, 4WV 4-way valve (shaded areas represent temperature controlled heated zones). The flow chart reactor diagram was adapted from Henkel (2012). The apparatus was developed at the Carl von Ossietzky University of Oldenburg (<http://www.roessner.chemie.uni-oldenburg.de>).

A 2 Product analysis

Online samples of the gas phase were taken via 6-way valves on top of every gas chromatograph and analyzed using different detectors (TCD, FID and MS). A 1 mL sample loop was filled with the product and leaded onto the GC column by switching the 6-way valve. Liquid phase samples (C₁₂₊) were collected after every Fischer-Tropsch experiment from the hot trap and selected samples were analyzed *offline*.

A 2.1 Gas chromatographic analysis: GC-TCD (*online*)

The consumption of CO, H₂ and the product of CO₂ and CH₄ were measured by using a HP 5890 gas chromatograph equipped with a thermal conductivity detector (GC-TCD) and nitrogen as a carrier gas. Separation of these compounds was performed on carbosieve II column. During the FTS measurement, temperature of the detector was kept constant at 180 °C. Additional details about GC-TCD parameter can be seen in Table A.1.

Ar was used as internal standard (IS) to calculate the molar flow rate (\dot{n}) of those compounds from the area (A) and the calibration factor f_{TCD} :

$$\dot{n}_i = f_{TCD,i} \cdot \left(\frac{A_i}{A_{Ar}} \right) \cdot \dot{n}_{Ar} \quad \dots\dots\dots (A.1)$$

$$\dot{n}_{Ar} = \left(\frac{\chi_{Ar} \cdot V_{IS(NTP)}}{V_A} \right) \quad \dots\dots\dots (A.2)$$

Where χ_{Ar} is the molar concentration of argon within the mixture argon / cyclohexane; $V_{IS(NTP)}$ is the volumetric flow rate of internal standard gas and V_A is Avogadro's volume. The obtained $f_{TCD,i}$ value was calibrated in constant intervals related to argon of a compound i. A known mixture of CO, CO₂, H₂, Ar and CH₄ was

prepared and the flow rates were controlled by mass flow controllers. The $f_{TCD,i}$ could be calculated following the equation A 3 The obtained calibration factors and retention time for the measurements with the GC-TCD are shown in Table A.2. An example pattern of spectra from GC-TCD can be seen in Figure A 2.

$$f_{TCD,I} = \left(\frac{[i] \cdot A_i}{[Ar] \cdot A_{Ar}} \right) \quad \dots\dots (A 3)$$

Table A 1 Parameter for GC-TCD analysis (Hewlett Packard 5890 (*online*)).

Parameter	Type or condition
Detector	Thermal conductivity detector (TCD) $T_{Detector} = 180 \text{ }^\circ\text{C}$
Column	Packed column (3 m x 1/8" O.D.)
Stationary phase	Carbosieve S-II, 80/100
Carrier gas	Nitrogen
Flow rate	15 mL/min
Injector	Splitless
Oven temperature	150 $^\circ\text{C}$ isothermal
Analyte	H ₂ , Ar (internal standard), CO, CH ₄ , CO ₂

Table A 2 Calibration factors $f_{\text{TCD},i}$ and retention time for each compound analyzed with the GC-TCD.

Compound	Calibration factor ($f_{\text{TCD},i}$)	Retention time (min)
Hydrogen (H ₂)	4.46	2.13
Argon (Ar)	1.00 ^a	3.66
Carbon monoxide (CO)	18.10	4.45
Methane (CH ₄)	0.64	7.95
Carbon dioxide (CO ₂)	14.0	14.84

^aCalibration factor of Ar was set as 1

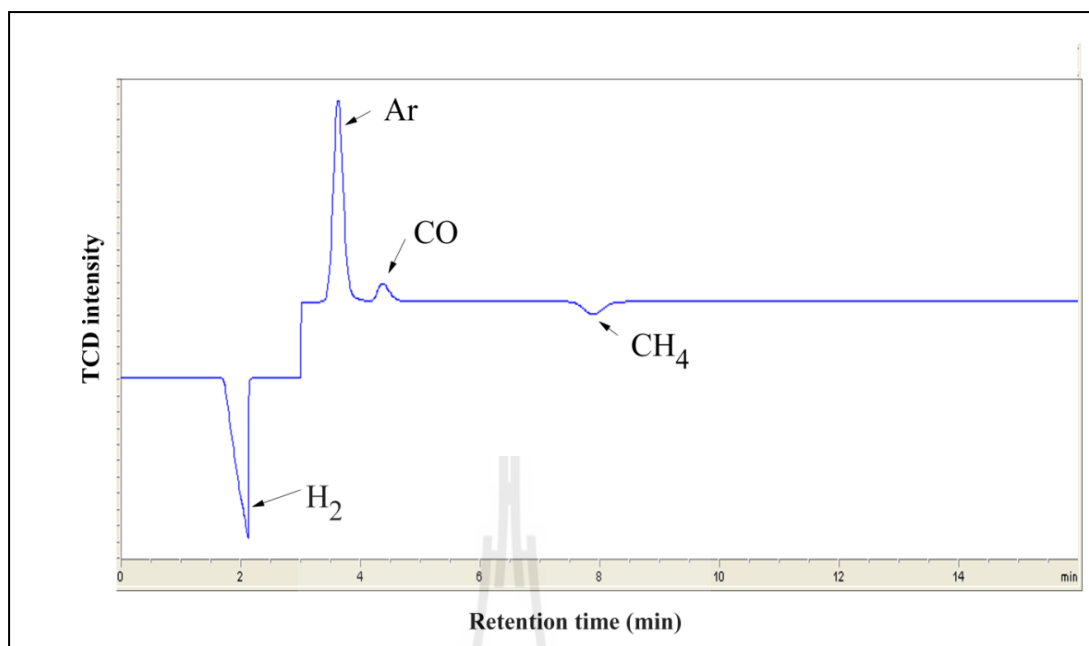


Figure A 2 Spectra of reactant, internal standard and product gases detected with GC-TCD.

A 2.2 Gas chromatographic analysis: GC-FID (*online*)

The organic products from FTS were detected and recorded by using two gas chromatographs equipped with flame ionization detector (GC-FID) and mass spectrometer (GC-MS)

A HP 6890 gas chromatograph with a FID and an Agilent HP Plot Q capillary column was performed to analyze all *n*-paraffin and α -olefins from C₂–C₉ generated during FTS. An advantage of the Agilent HP Plot Q capillary column was good to separate light hydrocarbon (C₂–C₄) even at higher oven temperature for *n*-paraffin and α -olefins from C₅–C₉. Moreover acetaldehyde, 2-methyl propane and β -butene were analyzed with the GC-FID as well. Additional parameters and retention time for GC-FID analysis can be found in Table A 3 and Table A 4. The example gas chromatograms for FT products are shown in Figure A 3.

According to the detector was FID, the FTS products (carbon atoms) were ionized in a flame resulting to a response signal in the detector. This response was linear but detection of carbon atoms at different oxidation states (oxygenates) resulted in a lower response signal (Cairns et al., 2008; Robert et al., 2012). This could be solved by using response factors $f_{FID,i}$ for the quantification of oxygenates such as acetaldehyde and alcohol:

$$f_{FID,i} = \left(\frac{N_C}{N_{C(No\ O)} + N_{C(with\ O)}} \right) \dots\dots\dots (A\ 4)$$

Where N_C is the number of all carbon atoms and the response of carbon atoms (not bonded to an oxygen atom) is 1. $N_{C(with\ O)}$ is the response of carbon atom bonded to an oxygen atom with a single bond. It's $f_{FID,I}$ is 0.55 but the carbon atoms with a C=O double bond are considered to generate no signal.

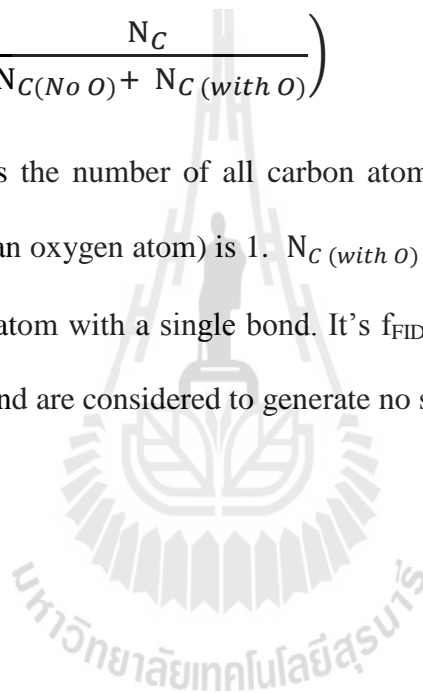


Table A 3 Parameter for GC-FID analysis (Hewlett Packard 6890 (*online*)).

Parameter	Type or condition
Detector	Flame ionization detector (FID) $T_{Detector} = 250\text{ }^{\circ}\text{C}$
Column	Agilent HP Plot Q (15 m, 0.32 mm I.D., 0.20 μm film thickness)
Stationary phase	Divinylbenzene/-styrol
Carrier gas	Hydrogen
Flow rate	3 mL/min for 1 min at 1 mL/min to 1 mL/min
Column head pressure	1.4 bar
Injector	Split $T_{Injector} = 230\text{ }^{\circ}\text{C}$ Split ratio = 1:1
Temperature program	40 $^{\circ}\text{C}$, 3 min isothermal at 8 $^{\circ}\text{C}/\text{min}$ to 120 $^{\circ}\text{C}$, 5 min isothermal at 8 $^{\circ}\text{C}/\text{min}$ to 230 $^{\circ}\text{C}$, 10 min isothermal
Analyte	<i>n</i> -paraffin, α -olefins from C ₂ –C ₉ , acetaldehyde, 2-methyl propane and β -butene

Cyclohexane was used as internal standard (IS) to calculate the molar flow rate (\dot{n}) of each organic compound:

$$\dot{n}_i = \left(\frac{N_{\text{CHX}}}{N_i} \right) \cdot \left(\frac{f_{\text{FID},i} \cdot A_i}{f_{\text{FID},\text{CHX}} \cdot A_{\text{CHX}}} \right) \cdot \dot{n}_{\text{CHX}} \quad \dots\dots\dots (\text{A } 5)$$

$$\dot{n}_{\text{CHX}} = \left(\frac{\chi_{\text{CHX}} \cdot V_{\text{IS}}(\text{NTP})}{V_A} \right) \quad \dots\dots\dots (\text{A } 6)$$

Where N_i is carbon number; A_i is the area of hydrocarbon compound i ; \dot{n}_{CHX} , \dot{n}_i are molar flow rate of cyclohexane and hydrocarbon compound i and χ_{CHX} is the concentration of cyclohexane in the mixture argon/cyclohexane.



Table A 4 The retention time (min) of all hydrocarbon compounds detected and recorded by GC-FID.

Compound	Retention time (min)	Compound	Retention time (min)
Methane	0.75	2- Methylbutane	18.66
Ethene	1.19	Propanal	19.63
Ethane	1.46	<i>n</i> -Pentene-(1)	20.10
Propene	7.84	<i>n</i> -Pentane	20.75
Propane	8.35	1-hexene	24.99
Acetaldehyde	12.05	<i>n</i> -hexane	25.13
1-Methylpropene	12.30	Cyclohexane (IS)	25.80
2-Methylpropane	12.64	1-Heptene	28.22
<i>n</i> -Butene-(1)	13.24	<i>n</i> -Heptane	28.37
<i>n</i> -Butane	13.69	1-Octene	30.90
tr.- <i>n</i> -Butene-(2)	13.84	<i>n</i> -Octane	31.02
cis.- <i>n</i> -Butene-(2)	14.07	1-Nonene	33.56
Ethanol	16.86	<i>n</i> -Nonane	33.73

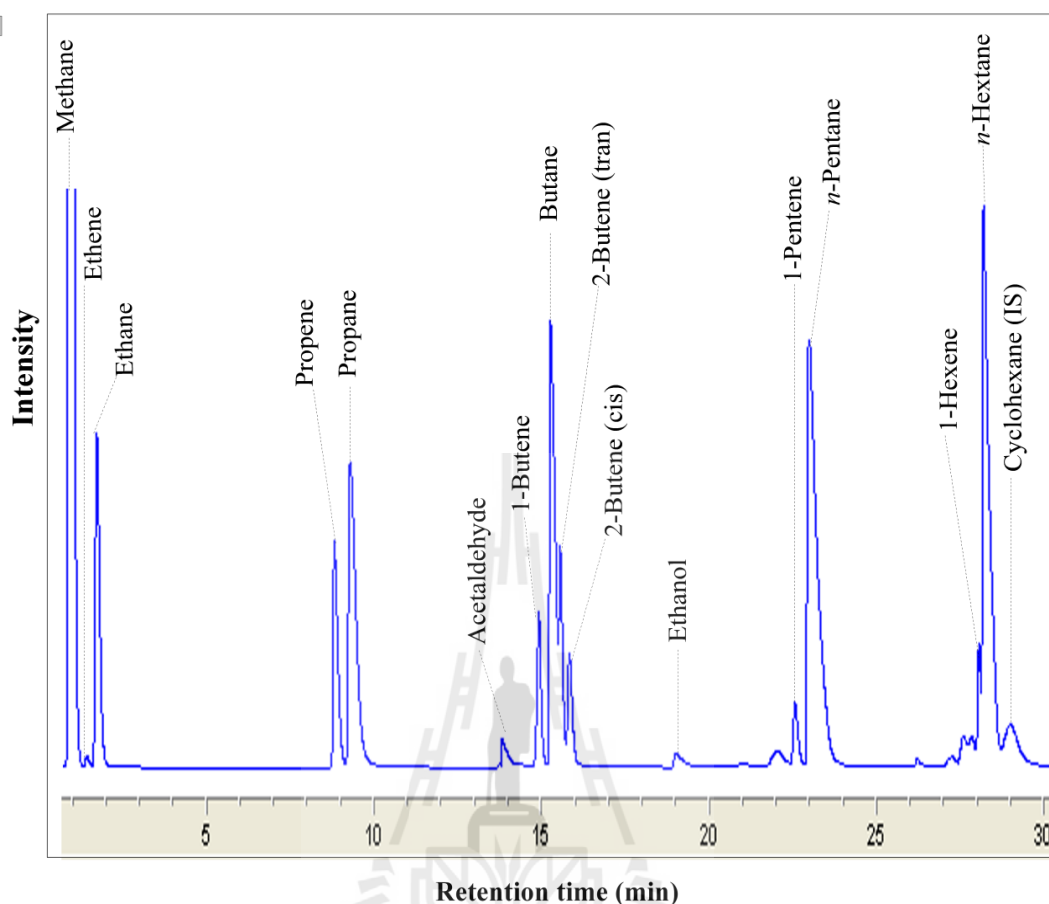


Figure A 3 Gas chromatogram for FT products from C₁–C₆ detected with GC-FID (C₇– C₉) compounds are not shown).

A 2.2 Gas chromatographic analysis: GC-MSD (*online*)

To confirm and quantify additional product classes including all oxygenated, branch and β -olefin hydrocarbons during FTS, a HP 6890 gas chromatograph equipped with a mass spectrometer (GC-MS) was used for analysis. The obtained mass spectra of each compound was compared with a database (National Institute Standard and Technology, NIST).

During the Fischer-Tropsch synthesis, a broad product spectra, consisting of paraffins, olefins or oxygenates was difficult to separate, identify and evaluate. The

GC-MS technique has an advantage which extracts characteristic ions from the organic molecules and the separation of several peaks becomes more accuracy (Figure A 4). A list of the extracted ions m/z used in this work can be found in Table A 6.

Figure A 5 illustrates hydrocarbon products including *n*-paraffins, branch paraffins, α - and β -olefins from C_5 – C_9 and some oxygenated products from C_1 – C_2 . The injection of sample was employed *online* with a 6-way valve with a 1 mL sample loop. Moreover the GC oven was cooled with liquid nitrogen at -40 °C to accurate separation of long chain hydrocarbons. Solvent delay for 12 minutes of each sample analysis was taken to avoid any damages of the filaments due to large amounts of inorganic gases such as CO, H_2 , Ar and CO_2 . Additional parameters and retention time for GC-MS analysis can be found in Table A 5 and Table A 6.

In practice, the analysis of hydrocarbon compounds with a mass spectrometer was more complicated than with a flame ionization detector because a mass spectrometer did not show a linear response signal with different concentrations. All products which are going to be quantified by the GC-MS had to be calibrated (APPENDIX B). Due to the prices or the availability of branched chemicals such as 2 and 3-methylpentane, 2 and 3-methylhexane for example, those compound classes could not be directly calibrated on the GC-MS. However, the quantification of all branched hydrocarbons in this work were used the accompanied calibration of a similar extracted ions (43 and 57 m/z) compound such as *n*-pentane and *n*-hexane.

An extracted ions and an internal standard cyclohexane, the molar flow rate of an organic compound could be calculated:

$$\dot{n}_i = \left(A_{MS,i} \left(\frac{A_i}{A_{CHX}} \right)^2 + B_{MS,i} \left(\frac{A_i}{A_{CHX}} \right) \cdot \dot{n}_{CHX} \right) \quad \dots\dots\dots(A\ 7)$$

The calibration factors $A_{MS,i}$ and $B_{MS,i}$ were obtained from a polynomial 2nd order from the calibration of hydrocarbon compound i with cyclohexane.

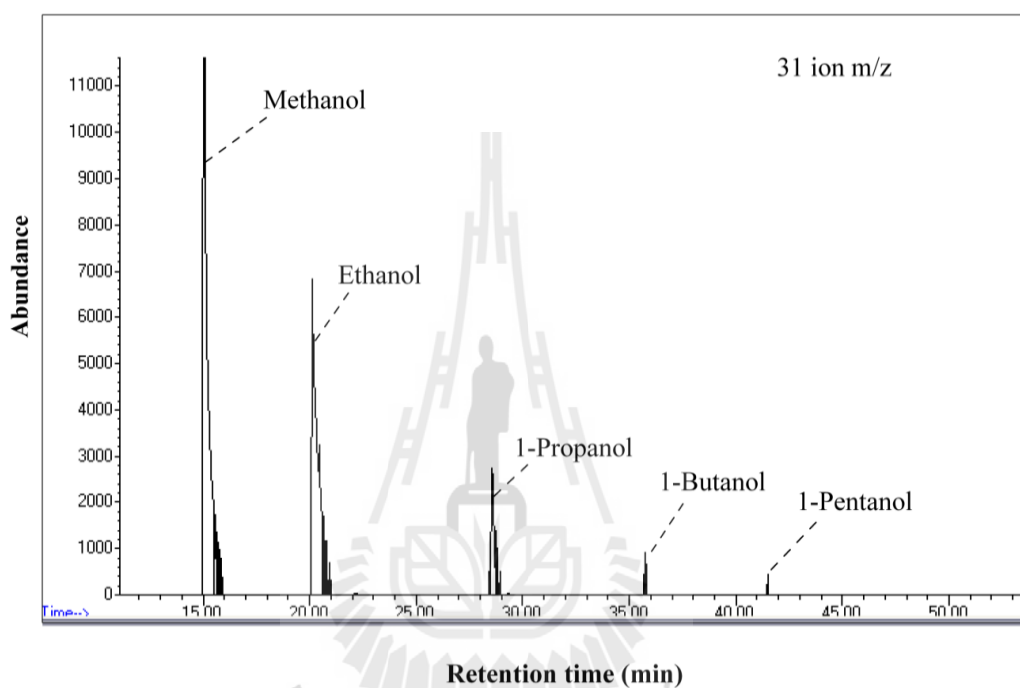


Figure A 4. Mass spectra (EI) of alcohols and extracted ion chromatogram for ion $m/z = 31$ from FTS.

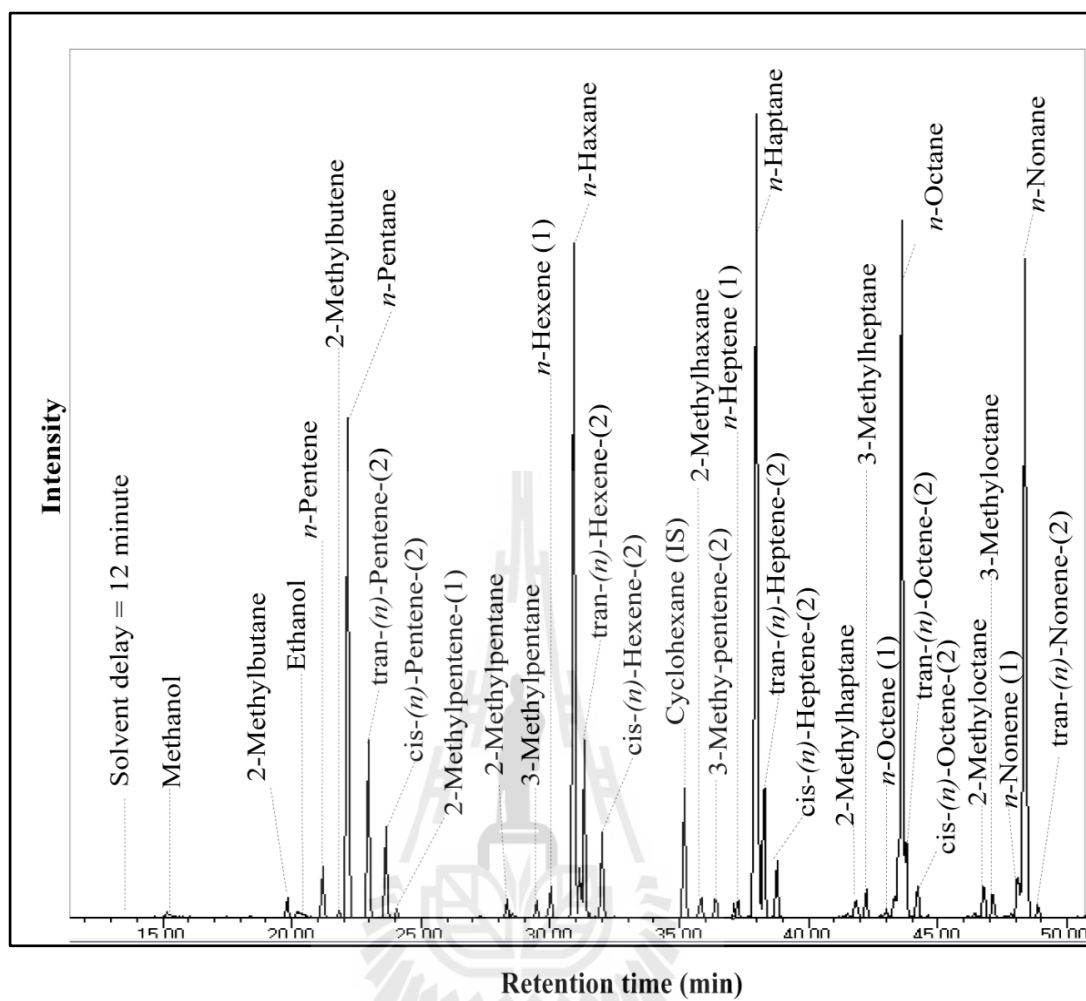


Figure A 5 Gas chromatogram for FT products detected with GC-MSD.

Table A 5 Parameter for GC-MSD analysis (Hewlett Packard 6890/5973 (*online*)).

Parameter	Type or condition
Mass spectrometer	Hewlett Packard 5973
Detector	Mass selective detector (MSD) $T_{\text{Detector}} = 150\text{ }^{\circ}\text{C}$ $T_{\text{Transfer line}} = 200\text{ }^{\circ}\text{C}$
Mode	Electron-impact (EI) $T_{\text{Source}} = 230\text{ }^{\circ}\text{C}$
Scan range	12 – 300 amu @ 4.83 scans/sec
Gas chromatograph	Hewlett Packard 6890 (<i>online</i>)
Column	Optima 1 MS Accent (60 m, 0.25 mm I.D., 0.25 μm film thickness) at 1 mL/min to 1 mL/min
Stationary phase	Dimethyl-polysiloxane
Carrier gas	Helium
Flow rate	2.7 mL/min
Column head pressure	1.4 bar

Table A 5 (Continued).

Injector	Split $T_{\text{Injector}} = 230\text{ }^{\circ}\text{C}$ Split ratio = 1:1
Temperature program	-40 $^{\circ}\text{C}$, 3 min isothermal at 8 $^{\circ}\text{C}/\text{min}$ to 120 $^{\circ}\text{C}$, 5 min isothermal at 8 $^{\circ}\text{C}/\text{min}$ to 230 $^{\circ}\text{C}$, 10 min isotherma
Analyte	<i>n</i> -and branched paraffins, α -and β -olefins and oxygenated products

Table A 6 The retention time (min) and specific ion (m/z) of all hydrocarbon compounds detected and recorded by GC-MSD.

Carbon number	Compound	Specific ion (m/z)	Retention time (min)
C ₁	Methanol	31	15.69
C ₂	Ethanol	31	20.35
C ₃	Propanal	31	20.58
	Propanol	31	28.54
C ₄	<i>n</i> -Butanol	31	35.72
C ₅	2-Methylbutane	43	19.92
	<i>n</i> -Pentene-(1)	42	21.29
	<i>n</i> -pentane	43	22.26
	tran-(<i>n</i>)-Pentene-(2)	55	22.99
	cis-(<i>n</i>)-Pentene-(2)	55	23.67
	<i>n</i> -Pentanol	31	41.50
	C ₆	2-Methylpentene-(1)	41
	2-Methylpentane	43	28.37
	3-Methylpentane	57	29.58
	<i>n</i> -Hexene	41	30.05
	<i>n</i> -Hexane	57	30.92
	tran-(<i>n</i>)-Hexene-(2)	41	31.18
	cis-(<i>n</i>)-Hexene-(2)	55	32.06
	Cyclohexane (IS)	84	35.23

Table A 6 (Continued).

Carbon number	Compound	Specific ion (m/z)	Retention time (min)
C ₇	2-Methylhexane	43	35.89
	3-Methylhexane	43	36.46
	1-Heptene	41	37.29
	<i>n</i> -Heptane	43	37.99
	tran-(<i>n</i>)-Heptene-(2)	41	38.30
	cis-(<i>n</i>)-Heptene-(2)	41	38.88
	C ₈	2-Methylheptane	43
3-Methylheptane		43	42.28
1-Octene		41	43.03
<i>n</i> -Octane		43	43.63
tran-(<i>n</i>)-Octene-(2)		41	43.78
cis-(<i>n</i>)-Octene-(2)		41	44.25
C ₉		2-Methyloctane	43
	3-Methyloctane	43	47.12
	1-Nonene	56	47.85
	<i>n</i> -Nonane	43	48.35
	tran-(<i>n</i>)-Nonene-(2)	55	48.86

References

- Cairns, P. (2008). **Oxygenates in Iron Fischer-Tropsch Synthesis: Is Copper a selectivity promoter?**. Ph.D. Thesis, University of Cape Town, South Africa.
- Henkel, R. (2012). **The influence of ammonia on Fischer-Tropsch synthesis and formation of N-containing compounds**. Ph.D. Thesis, der Carl von Ossietzky Universität Oldenburg, Germany.



APPENDIX B

CALIBRATION CURVE, SELECTED MOLAR FLOW RATE OF CATALYSTS AND ALPHA YIELD

B 1 Calibration curve

As mentioned above, for all FTS products detected and analyzed during the *online* GC analysis (GC-TCD, GC-FID and GC-MSD), calibration curves of the products had to be determined or calculated. Some calibration factors for GC-TCD were included in section Appendix A 2.1. An addition calibration curve of cyclohexane (IS) for GC-FID is shown in Figure B1

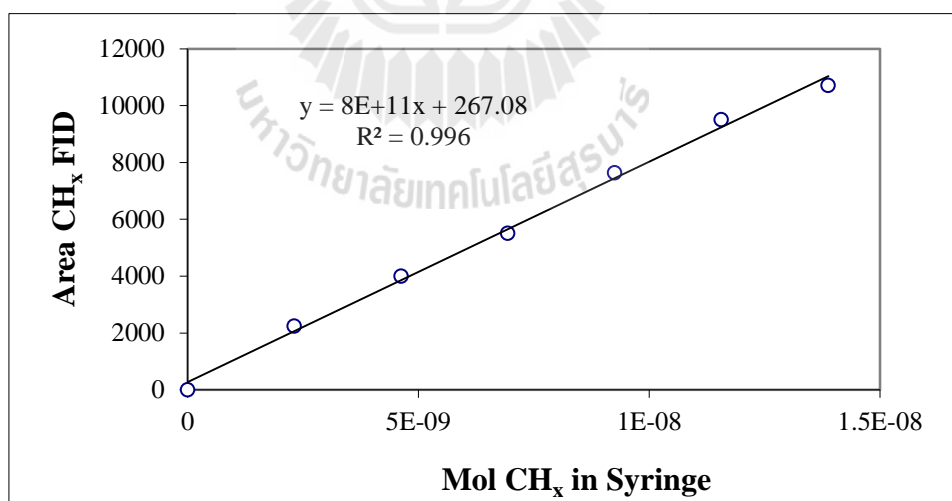


Figure B 1 The calibration curve of cyclohexane (IS) for GC-FID.

Briefly for GC-MS, the calibration of each analyte was injected thrice for 5 different volumes respectively (0.02 μL , 0.04 μL , 0.06 μL , 0.08 μL , and 0.1 μL). The molar ratio n_a/n_{is} (n_{is} is the amount of substance for the internal standard cyclohexane taken from the GC-FID chromatograms in Figure B 1 for every sample). Then it was plotted against the extracted ion area ratio m/z of the analyte and the cyclohexane (IS). A polynomial 2nd order gives the calibration factors $A_{MS,i}$ and $B_{MS,i}$ which are required to calculate the molar flow rate (equation A 7) of the specific organic compound formed during the Fischer-Tropsch reaction.

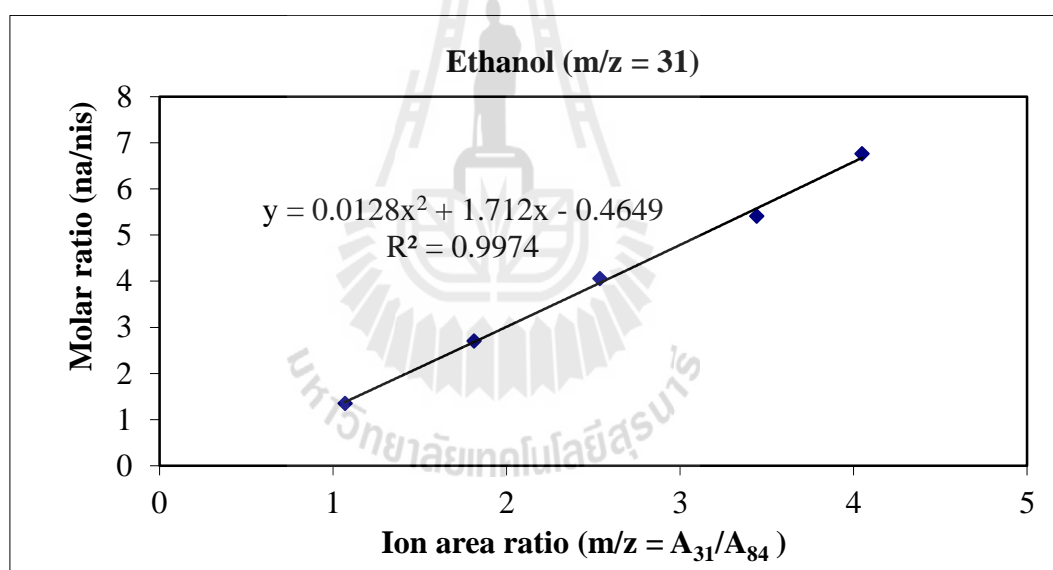


Figure B 2 Calibration curve of ethanol with the ion $m/z = 31$.

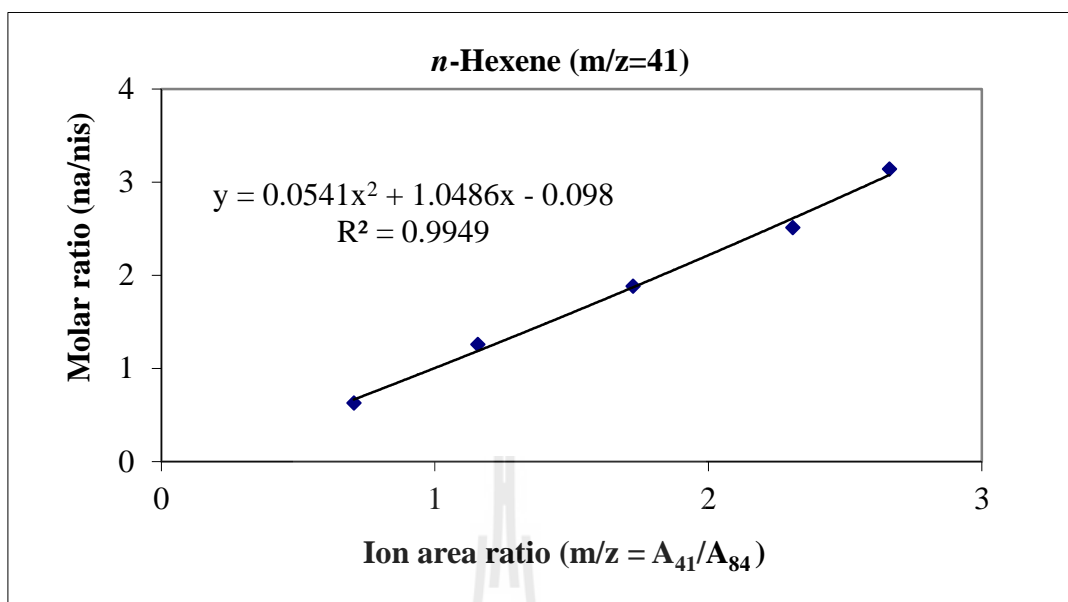


Figure B 3 Calibration curve for *n*-Octane with the ion m/z = 41.

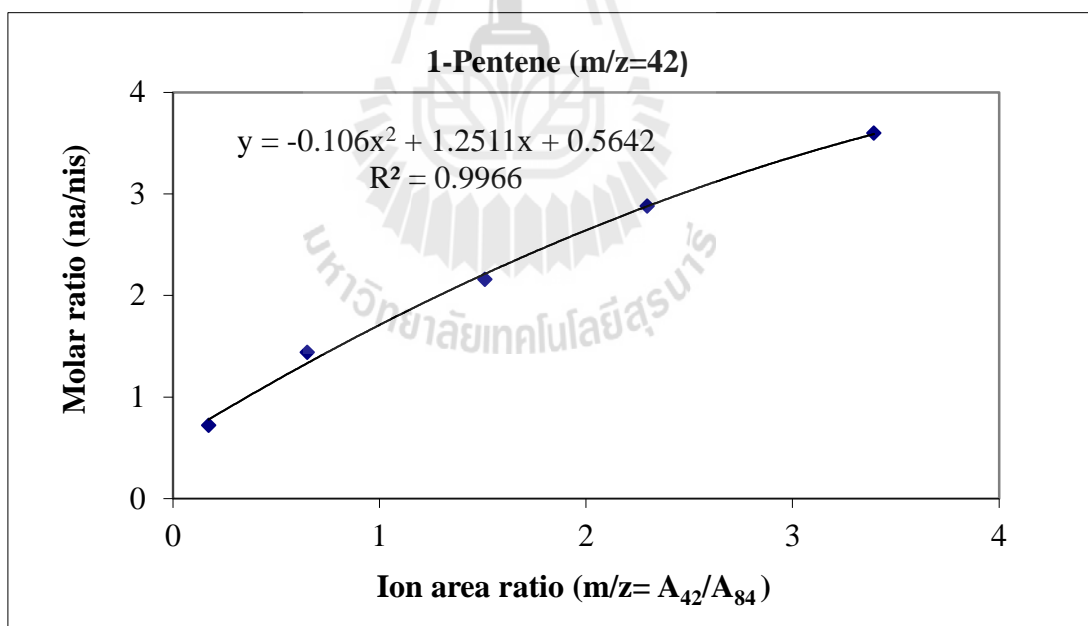


Figure B 4 Calibration curve for 1-Pentene with the ion m/z = 42.

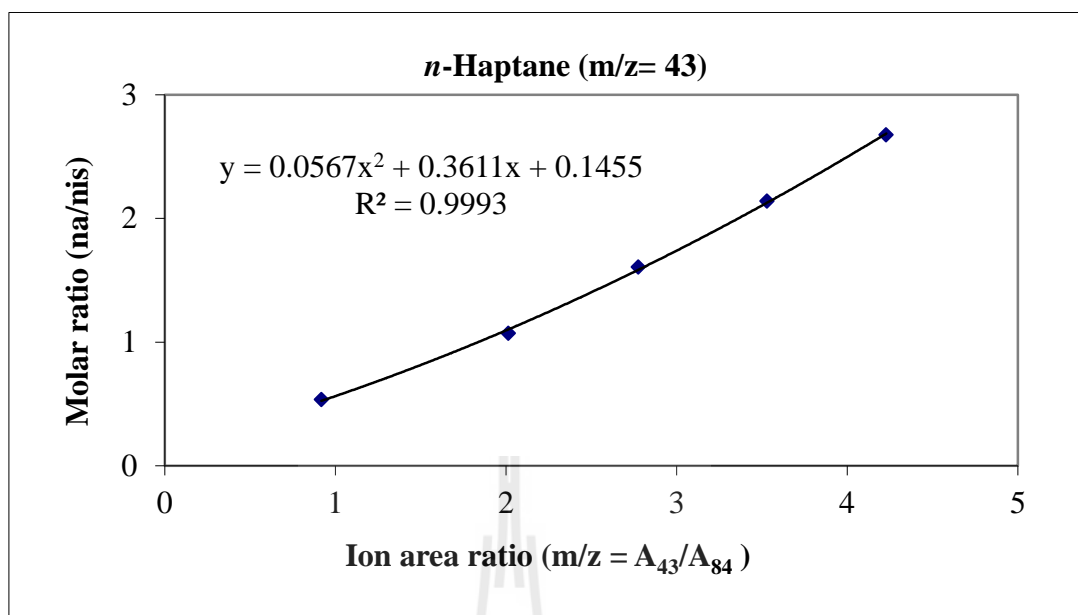


Figure B 5 Calibration curve for *n*-heptane with the ion m/z = 43.

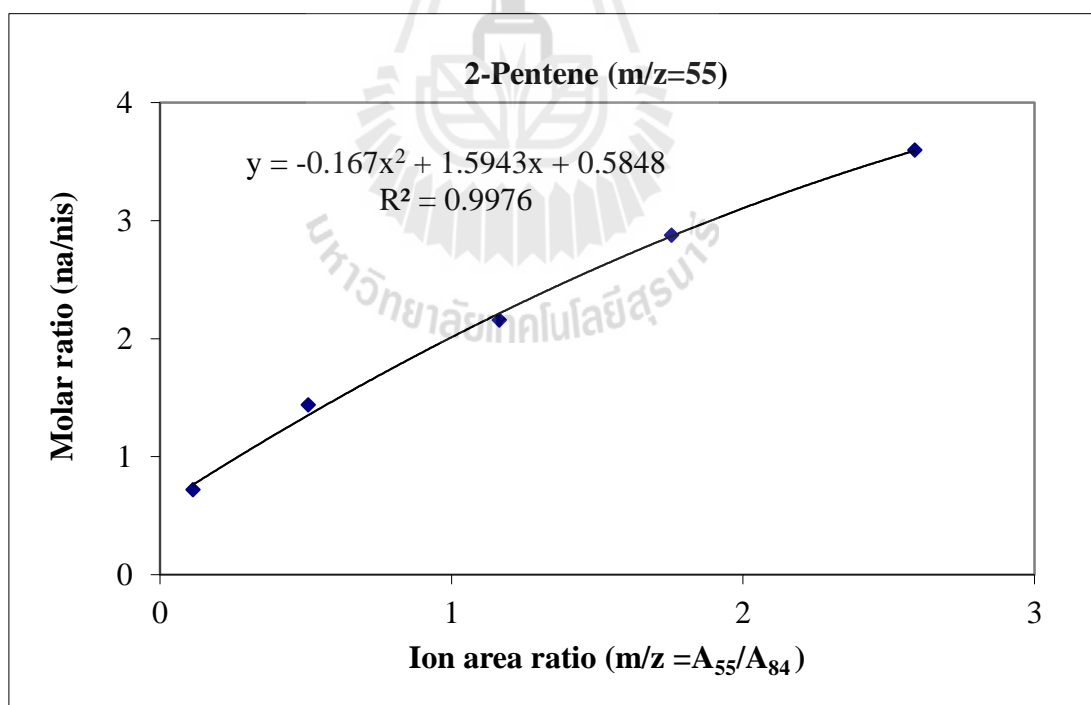


Figure B 6 Calibration curve for 2-Pentene with the ion m/z = 55.

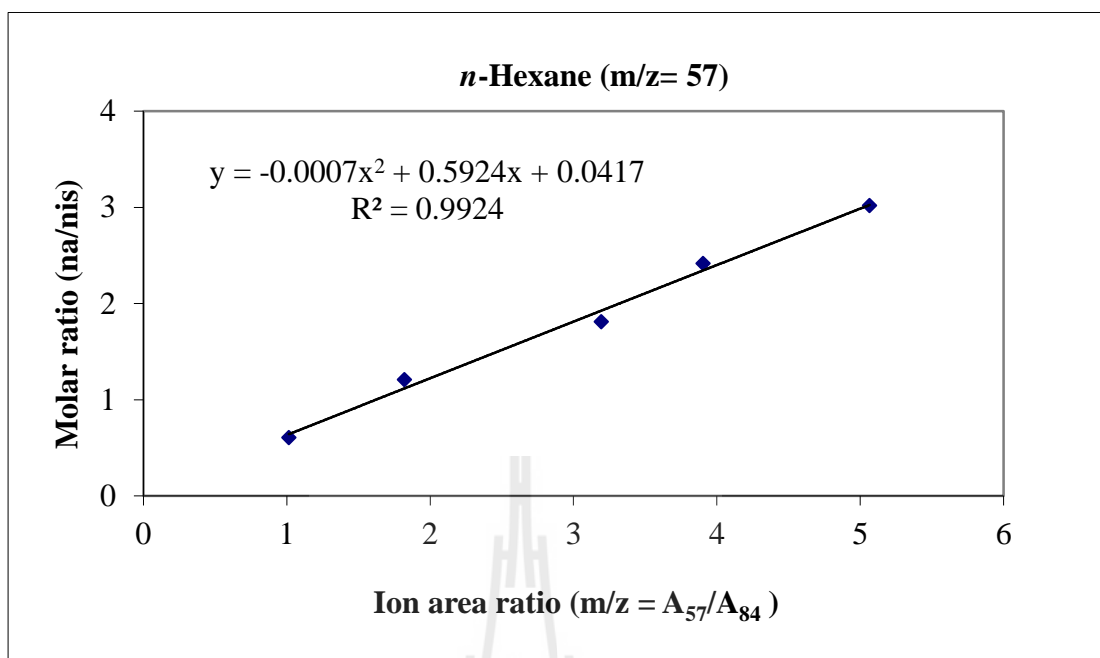


Figure B 7 Calibration curve for *n*-hexane with the ion m/z = 57.

B 2 Molar flow rate of catalysts

Not all samples are included the molar flow rate in this section. The sample named as 0.2Pd-10Co-SIP is selected for example catalyst to present the molar flow rate of all products and can be seen in below. In addition, the molar flow rate of hydrocarbon compounds for all catalysts in this work detected and calculated at 8 h of TOS will be presented as well.

Table B 1 Molar flow rate (mol/min) out of 0.2Pd-10Co-SIP as a function of time (h) on GC-TCD.

Time (h)	H ₂ (mol/min)	CO (mol/min)	CH ₄ (mol/min)
0.25	5.46E-05	6.20E-05	3.18E-05
0.5	1.20E-04	1.03E-04	5.12E-05
1	1.71E-04	1.58E-04	6.26E-05
1.5	2.07E-04	1.68E-04	6.67E-05
2	2.30E-04	1.77E-04	6.39E-05
2.5	2.52E-04	1.88E-04	6.27E-05
3	2.63 E-04	1.81E-04	6.39E-05
3.5	2.60E-04	1.86E-04	6.12E-05
4	2.79E-04	1.82E-04	6.04E-05
4.5	2.87E-04	1.79E-04	6.08E-05
5	2.97E-04	1.98E-04	6.58E-05
5.5	2.90E-04	1.89E-04	6.03E-05
6	3.13E-04	1.93 E-04	6.28E-05
6.5	3.17E-04	1.91E-04	5.93E-05
7	3.00E-04	1.88E-04	5.91E-05
7.5	3.03E-04	2.01E-04	5.74E-05
8	3.06E-04	1.90E-04	5.81E-05

Table B 2 Molar flow rate (mol/min) out of *n*-paraffin and methy-branched paraffin on 0.2Pd-10Co-SIP as a function of time (h) detected with GC-FID and GC-MSD.

Carbon number	Molar flow rate (mol/min) as function of time (h)				
	0.5	2	4	5.5	8
<i>n</i> -Paraffin					
2	2.29E-06	2.36E-06	2.09E-06	1.92E-06	2.09E-06
3	2.92E-06	2.78E-06	2.35E-06	2.13E-06	2.22E-06
4	2.28E-06	2.16E-06	1.84E-06	1.61E-06	1.63E-06
5	4.67E-06	3.09E-06	2.75E-06	2.77E-06	2.42E-06
6	2.60E-06	2.04E-06	1.85E-06	1.80E-06	1.71E-06
7	2.55E-06	1.71E-06	1.79E-06	1.58E-06	1.72E-06
8	1.43E-06	1.23E-06	1.20E-06	1.31E-06	1.20E-06
9	5.23E-07	5.71E-07	5.65E-07	5.67E-07	6.13E-07
Methyl-branched-Paraffin					
4	4.40E-08	5.10E-08	3.88E-08	2.55E-08	2.80E-08
5	2.31E-07	1.41E-07	1.21E-07	1.38E-07	1.07E-07
6	7.73E-07	5.22E-07	4.47E-07	4.31E-07	4.04E-07
7	3.34E-07	2.53E-07	2.28E-07	2.47E-07	2.08E-07
8	2.52E-07	1.97E-07	1.87E-07	2.28E-07	1.72E-07
9	1.86E-07	1.48E-07	1.45E-07	1.60E-07	1.47E-07

Table B 3 Molar flow rate (mol/min) out of α -olefin, linear olefin and alcohol on 0.2Pd-10Co-SIP as a function of time (h) detected with GC-FID and GC-MSD.

Carbon number	Molar flow rate (mol/min) as function of time (h)				
	0.5	2	4	5.5	8
α-Olefin					
2	4.64E-08	6.58E-08	7.48E-08	9.33E-08	9.94E-08
3	5.97E-07	1.01E-06	9.81E-07	9.02E-07	9.77E-07
4	3.15E-07	4.69E-07	4.38E-07	3.92E-07	4.35E-07
5	1.19E-07	2.06E-07	1.92E-07	1.92E-07	1.90E-07
6	1.51E-07	2.04E-07	1.87E-07	1.52E-07	1.52E-07
7	1.03E-07	1.61E-07	1.65E-07	1.72E-07	1.70E-07
8	4.86E-08	9.43E-08	9.87E-08	9.71E-08	9.15E-08
9	7.11E-09	3.49E-08	3.65E-08	3.83E-08	4.22E-08
Linear olefin					
4	1.34E-06	2.00E-06	1.89E-06	1.70E-06	1.79E-06
5	2.58E-06	2.25E-06	2.09E-06	2.44E-06	1.97E-06
6	9.14E-07	1.10E-06	1.07E-06	1.12E-06	9.92E-07
7	3.22E-07	4.49E-07	4.69E-07	5.09E-07	4.78E-07
8	4.98E-08	9.59E-08	1.01E-07	9.87E-08	9.65E-08
9	5.87E-08	1.01E-07	1.15E-07	1.33E-07	1.36E-07
Alcohol					
1	2.20E-07	5.59E-07	6.47E-07	6.79E-07	6.45E-07
2	4.48E-08	2.04E-07	2.27E-07	2.01E-07	2.29E-07
3	3.46E-09	2.79E-08	3.24E-08	3.53E-08	3.41E-08
4	0	7.87E-09	1.02E-08	1.25E-08	1.37E-08
5	0	9.96E-10	5.97E-09	9.26E-09	1.09E-08

Table B 4 Molar flow rate (mol/min) of *n*-paraffin and methyl-branched-paraffin based on carbon of catalyst supported SiO₂ series @ 8 h of TOS.

Carbon number	Catalysts					
	10Co-IP	0.2Pd-10Co-IP	1Pd-10Co-IP	10Co-RM	0.2Pd-10Co-RM	1Pd-Co-RM
n-Paraffin						
2	9.32E-07	3.915E-06	1.12E-06	2.02E-06	2.42E-06	7.46E-07
3	7.97E-07	7.53E-06	1.67E-06	3.26E-06	4.10E-06	7.51E-07
4	8.74E-07	7.33E-06	1.39E-06	2.21E-06	3.30E-06	4.35E-07
5	1.97E-06	9.07E-06	1.18E-06	2.05E-06	2.60E-06	2.62E-07
6	2.34E-06	7.34E-06	9.75E-07	1.32E-06	1.61E-06	1.32E-07
7	2.52E-06	5.79E-06	6.66E-07	8.66E-07	9.393E-07	6.70E-08
8	2.50E-06	4.97E-06	4.54E-07	5.67E-07	5.49E-07	3.21E-08
9	2.93E-06	4.58E-06	2.59E-07	4.01E-07	3.540E-07	1.80E-08
Methyl-branched-Paraffin						
4	6.89E-08	2.74E-07	5.08E-08	8.58E-08	1.58E-07	2.90E-08
5	1.05E-08	2.08E-07	7.82E-09	2.58E-08	5.73E-08	1.27E-08
6	2.63E-08	8.14E-07	2.86E-08	6.07E-08	1.33E-07	2.72E-08
7	3.88E-08	4.64E-07	1.28E-08	3.04E-08	5.44E-08	9.82E-09
8	2.15E-08	4.07E-07	1.538E-08	1.85E-08	4.04E-08	9.45E-09
9	3.95E-08	4.25E-07	1.39E-08	1.74E-08	3.90E-08	2.15E-08

Table B 5 Molar flow rate (mol/min) of α -olefin, linear olefin and alcohol based on carbon of catalyst supported on SiO₂ series @ 8 h of TOS.

Carbon number	Catalyst					
	10Co-IP	0.2Pd-10Co-IP	1Pd-10Co-IP	10Co-RM	0.2Pd-10Co-RM	1Pd-10Co-RM
α -Olefin						
2	3.58E-07	7.13E-08	2.01E-08	2.51E-08	2.49E-08	1.26E-08
3	1.88E-06	6.96E-07	3.92E-08	1.51E-07	8.24E-08	1.59E-08
4	1.43E-06	4.56E-07	1.59E-08	7.15E-08	3.45E-08	1.90E-09
5	1.20E-06	2.02E-07	8.92E-09	1.86E-08	5.42E-09	2.49E-09
6	6.44E-07	1.69E-07	1.70E-08	1.72E-08	0	0
7	3.90E-07	1.048E-07	1.31E-08	7.55E-09	0	0
8	3.91E-07	9.17E-08	1.52E-08	6.12E-09	0	0
9	3.20E-07	7.73E-08	1.23E-08	3.35E-09	0	0
Linear olefin						
4	2.13E-06	2.00E-06	2.26E-07	3.86E-07	3.59E-07	3.59E-08
5	1.71E-06	1.63E-06	1.16E-08	3.40E-08	1.18E-08	2.49E-09
6	1.02E-06	5.78E-07	1.70E-08	1.72E-08	0	0
7	6.85E-07	2.42E-07	1.31E-08	7.55E-09	0	0
8	5.04E-07	1.40E-07	1.52E-08	6.12E-09	0	1.21E-09
9	3.80E-07	1.15E-07	1.23E-08	3.35E-09	2.66E-09	0
Alcohol						
1	4.29E-09	3.57E-07	6.71E-08	2.12E-07	4.95E-07	2.90E-07
2	5.33E-07	8.25E-07	1.66E-07	4.77E-07	4.18E-07	8.37E-08
3	3.48E-08	1.19E-07	5.20E-10	2.56E-08	2.80E-08	0
4	3.05E-09	5.49E-08	0	1.03E-10	0	0
5	8.63E-09	4.50E-08	0	0	0	0

Table B 6 Molar flow rate (mol/min) of *n*-paraffin and methyl-branched-paraffin based on carbon of catalyst supported SBA-15 and SBA-15 (M) @ 8 h of TOS.

Carbon number	Catalysts			
	10CO/SBA-15	0.2Pd-10Co/SBA-15	10CO/SBA-15(M)	0.2Pd-10Co/SBA-15(M)
<i>n</i> -Paraffin				
2	4.19E-06	4.34E-06	5.36E-06	4.61E-06
3	5.40E-06	8.98E-06	8.34E-06	8.52E-06
4	4.95E-06	7.47E-06	8.10E-06	7.82E-06
5	1.04E-05	1.09E-05	1.38E-05	8.90E-06
6	9.67E-06	8.66E-06	1.14E-05	7.29E-06
7	8.17E-06	7.13E-06	8.50E-06	5.79E-06
8	6.28E-06	5.84E-06	5.19E-06	4.09E-06
9	6.07E-06	5.17E-06	2.76E-06	3.35E-06
Methyl-branched-Paraffin				
4	1.18E-07	1.86E-07	1.61E-07	2.75E-07
5	1.95E-07	1.55E-07	6.31E-07	2.57E-07
6	7.48E-07	4.13E-07	2.62E-06	7.22E-07
7	4.36E-07	2.41E-07	1.65E-06	3.87E-07
8	4.25E-07	2.48E-07	1.29E-06	3.61E-07
9	4.43E-07	2.81E-07	9.86E-07	3.30E-07

Table B 7 Molar flow rate (mol/min) of α -olefin, linear olefin and alcohol based on carbon of catalyst supported SBA-15 and SBA-15 (M) @ 8 h of TOS.

Carbon number	Catalysts			
	10CO/SBA-15	0.2Pd-10Co/SBA-15	10CO/SBA-15(M)	0.2Pd-10Co/SBA-15(M)
α -Olefin				
2	1.63E-07	6.17E-08	1.29E-07	7.52E-08
3	3.42E-06	1.03E-06	2.89E-06	3.87E-07
4	1.85E-06	6.88E-07	1.88E-06	2.86E-07
5	9.06E-07	2.14E-07	8.65E-07	1.49E-07
6	9.62E-07	3.32E-07	1.02E-06	1.70E-07
7	8.73E-07	2.69E-07	1.18E-06	1.15E-07
8	7.32E-07	1.580E-07	7.49E-07	5.22E-08
9	4.53E-07	1.44E-07	1.87E-08	1.87E-08
Linear olefin				
4	5.73E-06	3.28E-06	6.48E-06	1.47E-06
5	9.22E-06	2.75E-06	6.49E-06	1.21E-06
6	5.79E-06	1.24E-06	4.40E-06	5.28E-07
7	3.17E-06	5.53E-07	2.48E-06	2.34E-07
8	1.29E-06	2.17E-07	1.01E-06	8.34E-08
9	1.20E-06	2.22E-07	3.61E-07	6.21E-08
Alcohol				
1	1.74E-07	4.39E-07	4.03E-07	6.38E-07
2	2.72E-07	4.17E-07	3.98E-07	4.78E-07
3	3.72E-08	4.21E-08	6.49E-08	3.60E-08
4	2.52E-09	1.22E-08	2.35E-08	4.13E-09
5	2.36E-09	1.39E-09	8.48E-09	5.66E-10

Table B 8 Molar flow rate (mol/min) of all hydrocarbon compounds based on carbon of catalyst supported SBA-15 prepared by different Pd addition method @ 8 h of TOS.

Carbon number	Catalysts			
	0.2Pd-10Co-SIP	0.2Pd-10Co-CIP	0.2Pd-10Co-SIP	0.2Pd-10Co-CIP
	<i>n</i> -Paraffin		α -Olefin	
2	4.18E-06	4.34E-06	1.98E-07	6.17E-08
3	6.68E-06	8.98E-06	2.93E-06	1.03E-06
4	6.53E-06	7.47E-06	1.74E-06	6.88E-07
5	1.21E-05	1.09E-05	9.51E-07	2.14E-07
6	1.03E-05	8.66E-06	9.12E-07	3.32E-07
7	1.21E-05	7.13E-06	1.19E-06	2.69E-07
8	9.61E-06	5.84E-06	7.32E-07	1.580E-07
9	5.52E-06	5.17E-06	3.80E-07	1.44E-07
	Methyl-branched-Paraffin		Linear olefin	
4	1.12E-07	1.86E-07	7.16E-06	3.28E-06
5	5.39E-07	1.55E-07	9.82E-06	2.75E-06
6	2.42E-06	4.13E-07	5.95E-06	1.24E-06
7	1.45E-06	2.41E-07	3.35E-06	5.53E-07
8	1.37E-06	2.48E-07	7.72E-07	2.17E-07
9	1.32E-06	2.81E-07	1.23E-06	2.22E-07
	Alcohol			
1	6.45E-07	4.39E-07		
2	4.58E-07	4.17E-07		
3	1.02E-07	4.21E-08		
4	5.49E-08	1.22E-08		
5	5.46E-08	1.39E-09		

Table B 9 Comparisons between C₅–C₉ selectivity and yield of all catalysts in this work measured @ 8 h of TOS.

Catalysts	C ₅ –C ₉ selectivity based	C ₅ –C ₉ yield based
	on % C	on %C
10Co-IP	17.05	3.87
0.2Pd-10Co-IP	32.73	8.45
1Pd-10Co-IP	15.15	0.83
10Co-RM	14.13	1.25
0.2Pd-10Co-RM	15.78	1.48
1Pd-10Co-RM	10.62	0.13
10Co/SBA-15	23.05	15.41
0.2Pd-10Co/SBA-15(CIP)	31.50	8.29
10Co/SBA-15(M)	19.42	16.88
0.2Pd-10Co/SBA-15(M)	24.90	9.77
0.2Pd-10Co/SBA-15(SIP)	38.20	18.57

B 3 Chain growth probability (α yield)

As mentioned early in chapter II and III, The probability of the species on the surface growing by one carbon number (C_{n-1} to C_n) as opposed to desorbing is described as the chain growth probability (α_{n-1}). If α is independent of carbon number, it can be found from the Anderson-Schulz-Flory (ASF).

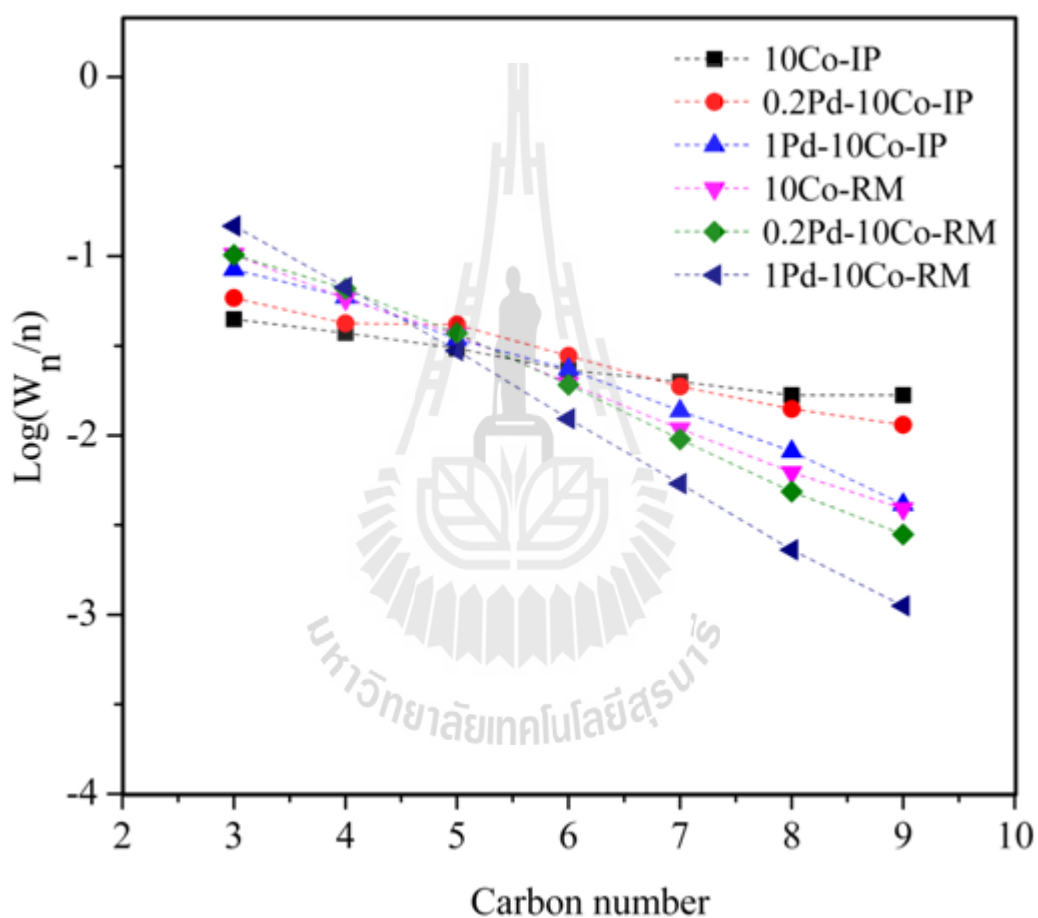


Figure B 8 Log of formation rates of linear hydrocarbons versus carbon number for catalyst supported on SiO_2 series @ 8 h of TOS.

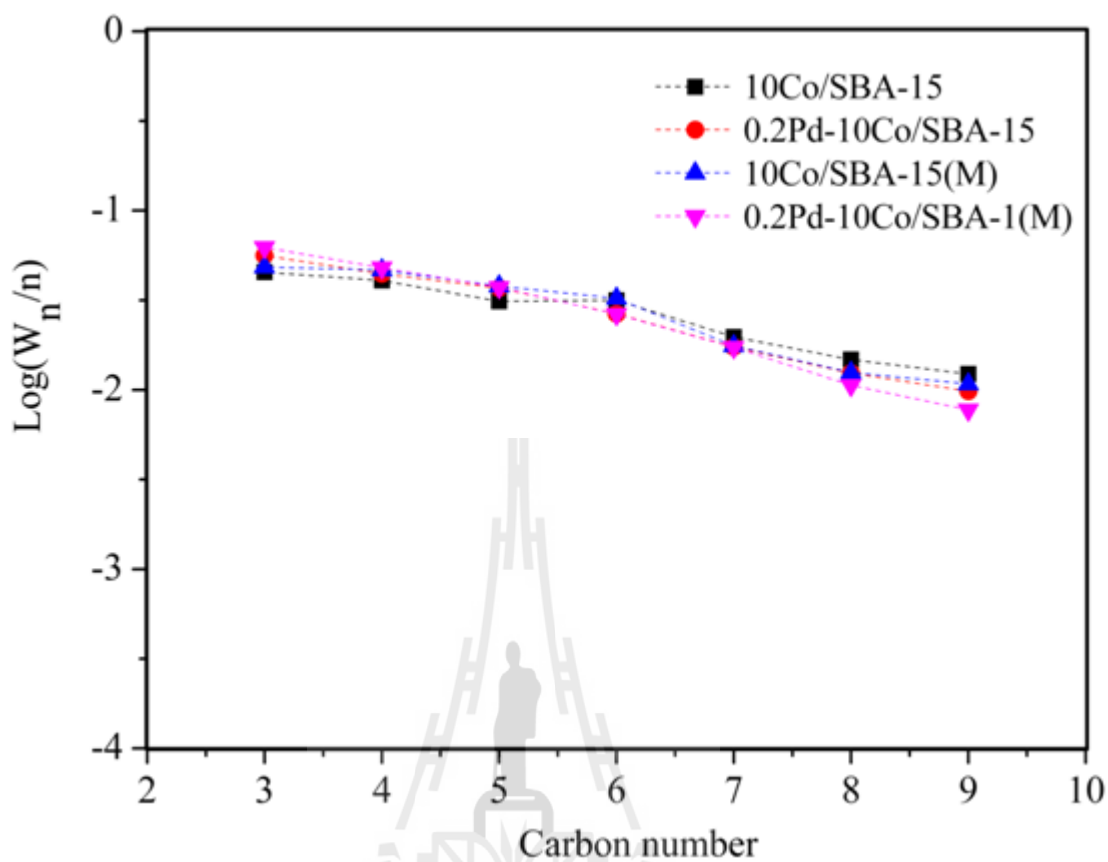


Figure B 9 Log of formation rates of linear hydrocarbons verse carbon number for catalyst supported SBA-15 and SBA-15 (M) @ 8 h of TOS.

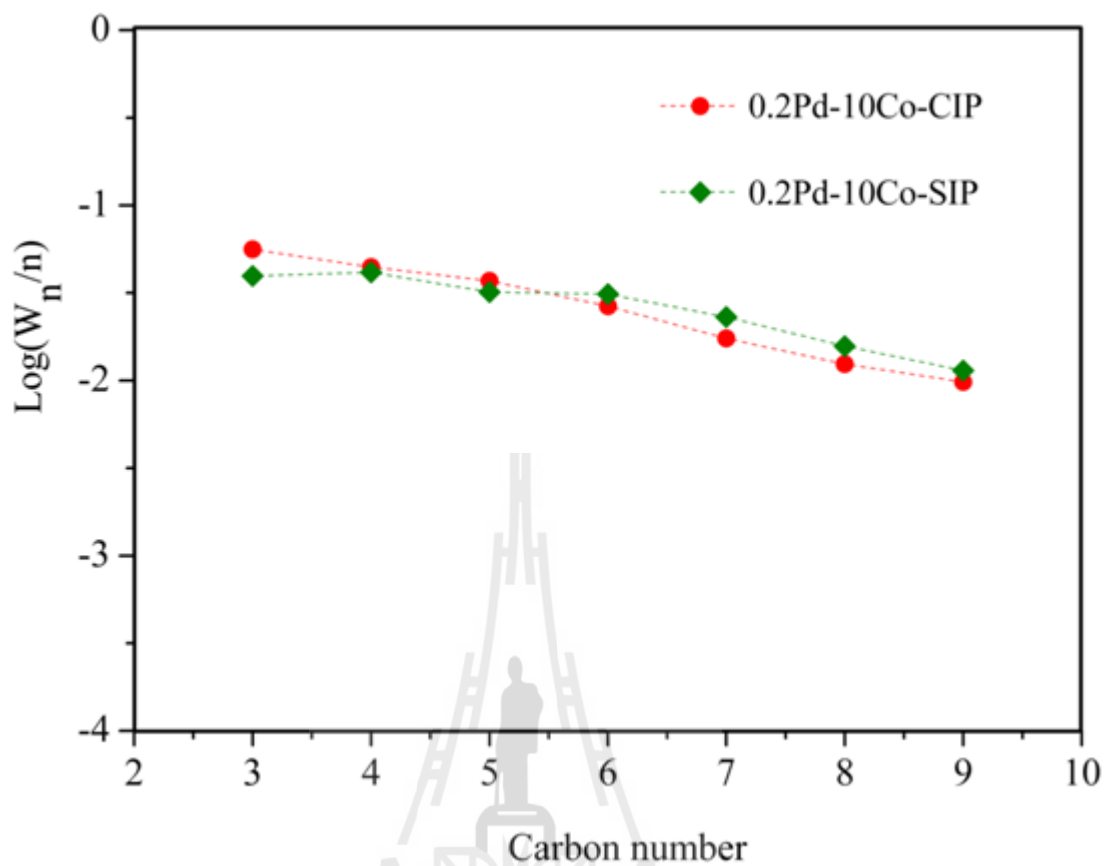


Figure B 10 Log of formation rates of linear hydrocarbons verse carbon number for catalyst supported SBA-15 prepared by different Pd addition method @ 8 h of TOS.

APPENDIX C

ADDITIONAL CHARACTERIZATION RESULTS

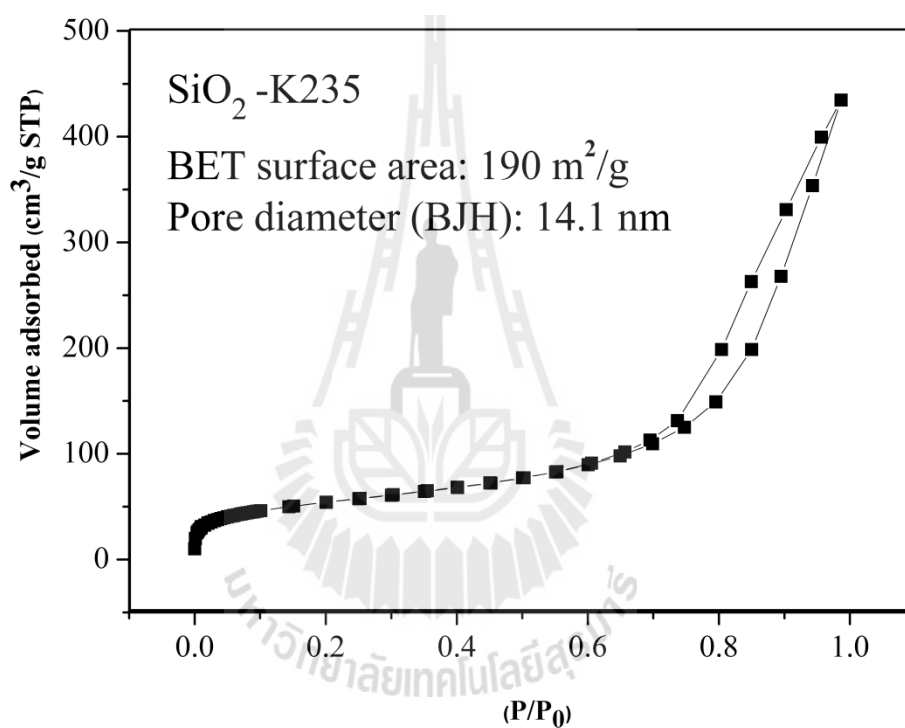


Figure C 1 N₂ adsorption – desorption isotherm of SiO₂-K235.

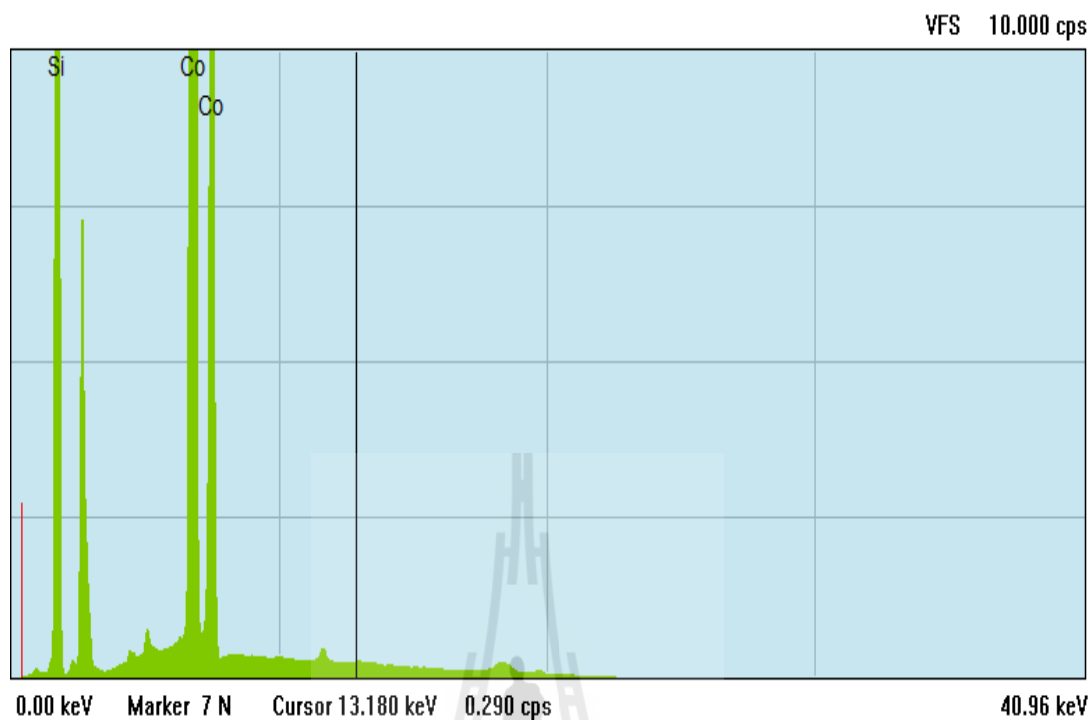


Figure C 2 Spectra of 10Co-SiO₂ characterized by Energy Dispersive X-ray Fluorescence (EDXRF, Horiba XGT-5200)

Table C 1 The quantitation of Co supported on SiO₂ by EDXRF, Horiba XGT-5200.

Catalysts	Co (% wt)	2 σ
10Co-IP	10.3	0.058
0.2Pd-10Co-IP	10.4	0.062
1Pd-10Co-IP	9.9	0.061
10Co-RM	10.8	0.064
0.2Pd-10Co-RM	11.1	0.075
1Pd-10Co-RM	10.2	0.066

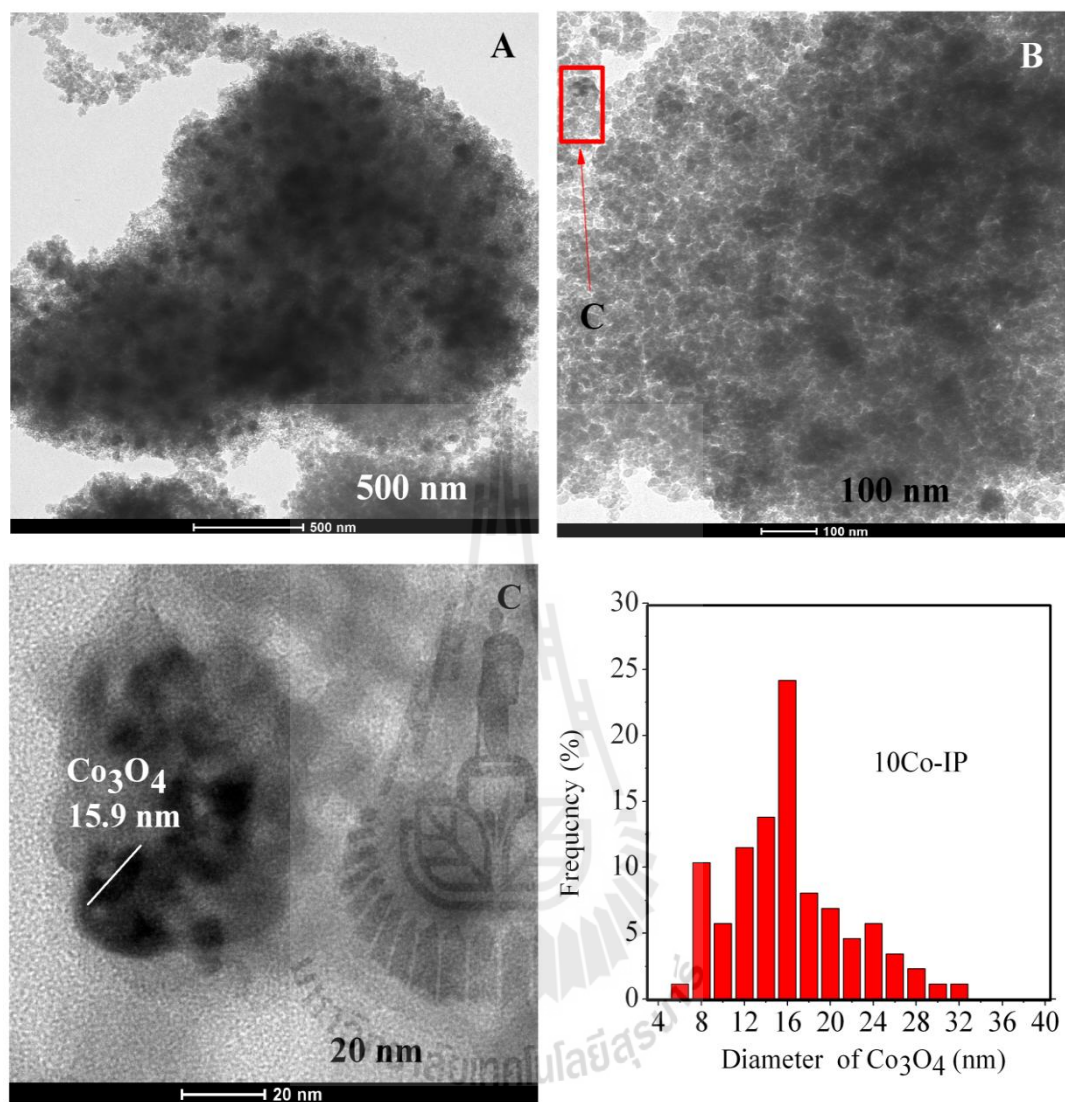


Figure C 3 TEM image of calcined 10Co-IP.

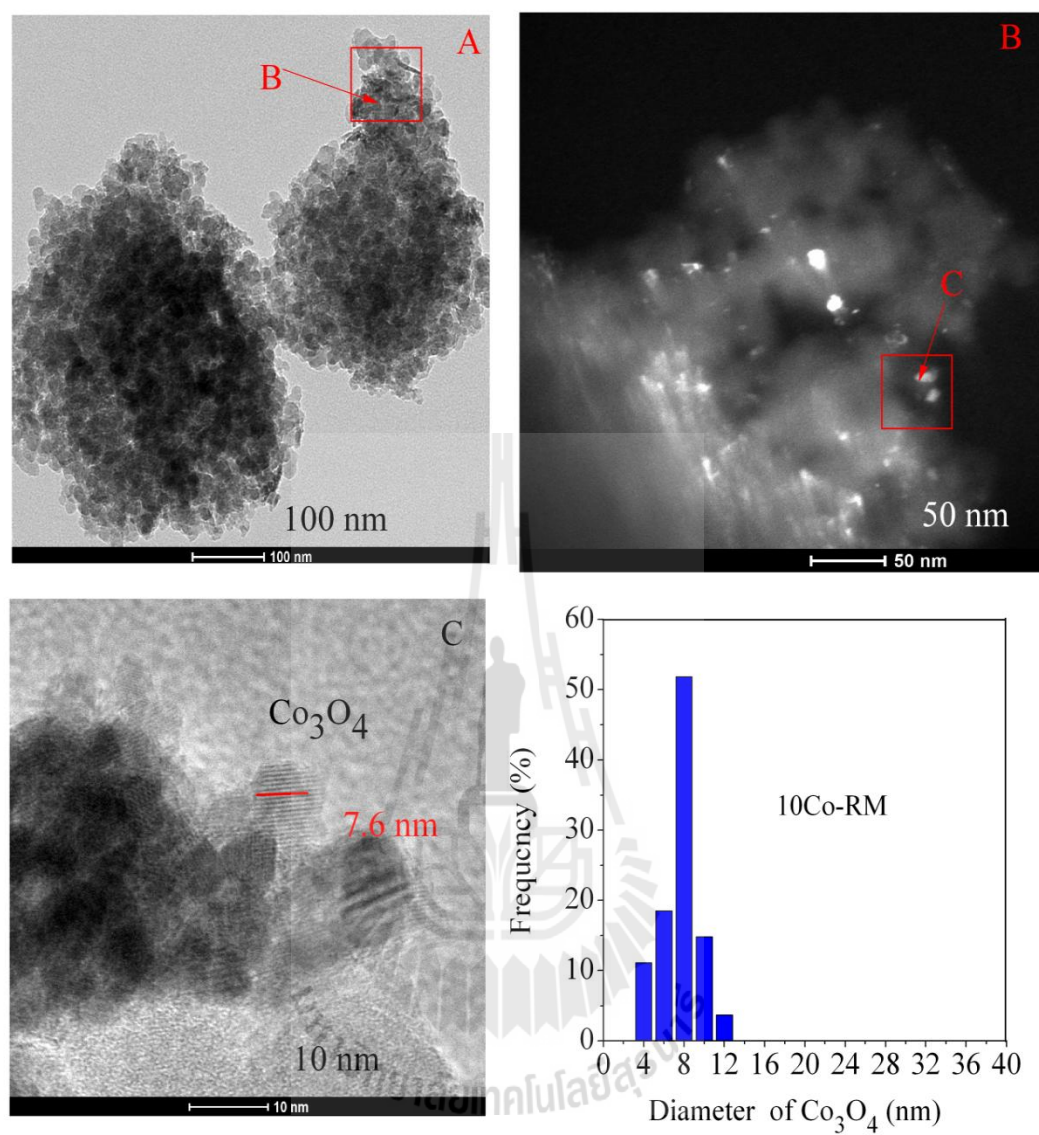


Figure C 4 TEM image of calcined 10Co-RM.

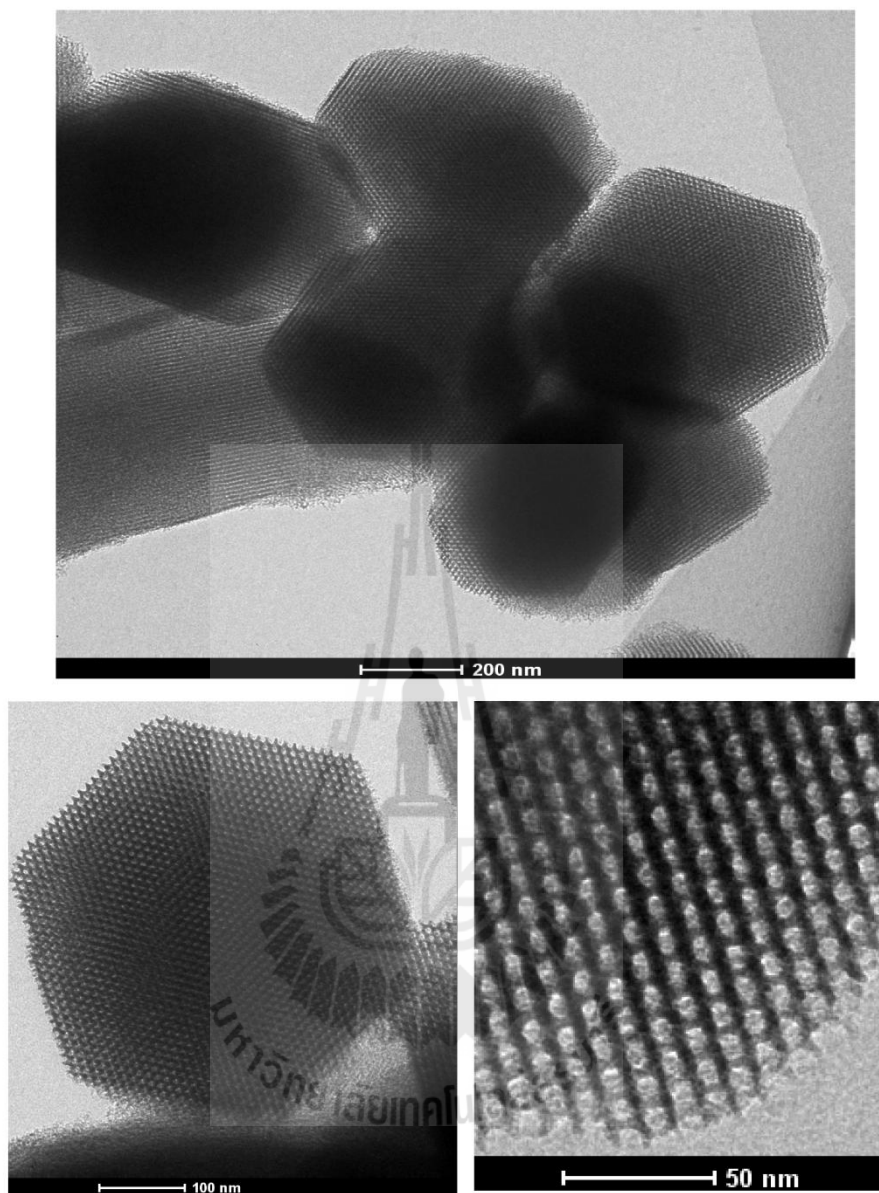


Figure C 5 TEM image of SBA-15.

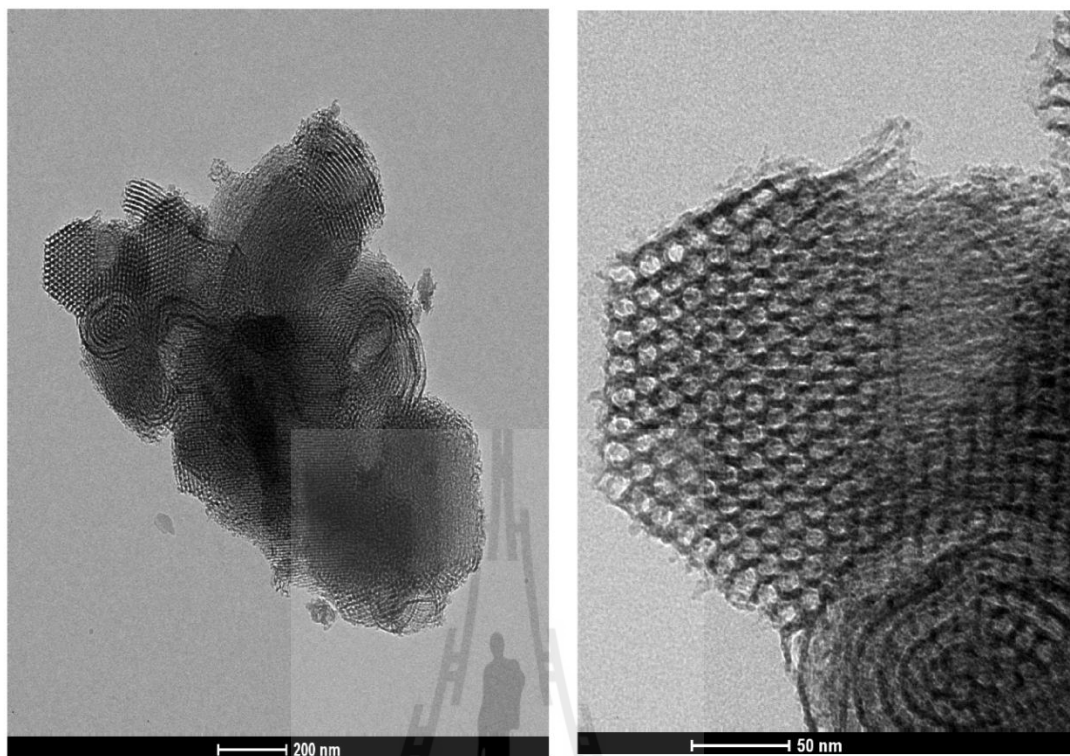


Figure C 6 TEM image of SBA-15 (M).



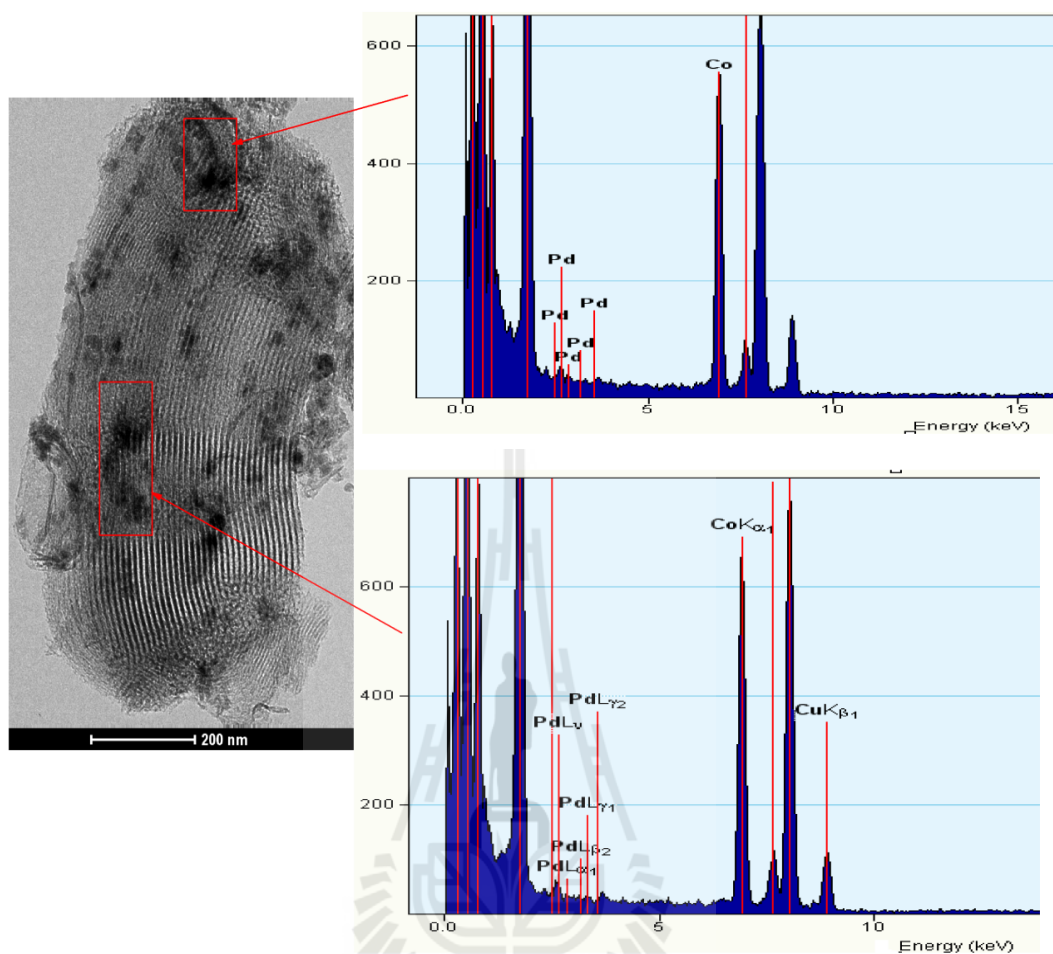


Figure C 7 TEM image and EDX spectra of spent catalyst (0.2Pd-10Co-SIP).

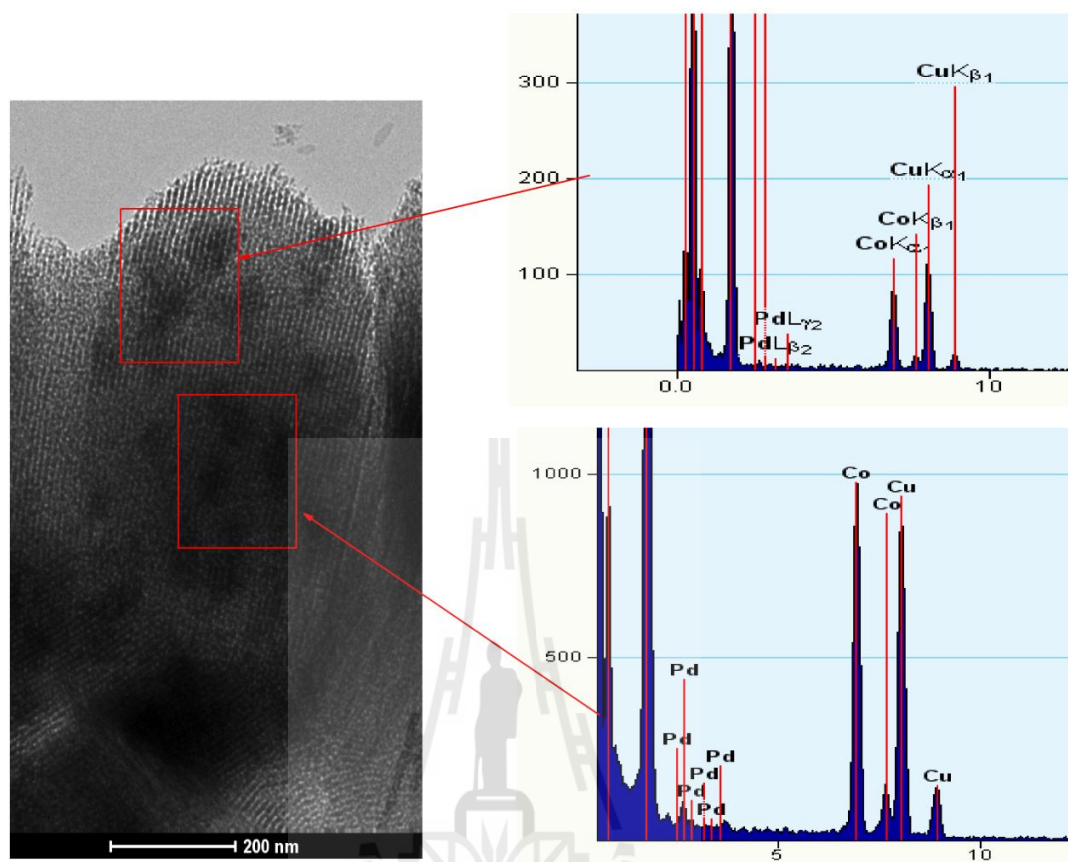


Figure C 8 TEM image and EDX spectra of spent catalyst (0.2Pd-10Co-CIP).

Table C 2 The quantitation of spent catalyst (Pd-Co supported on SBA-15) by TEM-EDX, Tecnai G20 (FEI-2012, LaB6).

Catalysts	Pd (% wt)	Co (% wt)
0.2Pd-10Co-SIP	0.19	10.3
0.2Pd-10Co-CIP	0.21	10.8

